Università degli studi di Genova

Facoltà di Scienze M.F.N

Doctorate school in

Sciences and Technologies of Chemistry and Materials

Doctorate in Materials Science and Technology

XXXIV cycle

Thesis title:

Development of multi-functional nanostructured membranes for airborne particles collection, fluidic sensing and co-localized plasmonic enhancement

PhD Candidate: Giacomo Manzato

Supervisors: Prof. Francesco Buatier de Mongeot (UniGe DIFI)

Dr. Paolo Brotto (PM_TEN s.r.l., UniGe spinoff)

Contents

Introduction

Monitoring and identifying biomolecules and nanoscale particulate matter represents a relevant technological challenge with deep social and environmental implications, requiring smart sensing solutions to enable multifactorial and high sensitivity measurements. In this thesis I investigate original approaches derived from nanotechnology for collecting and concentrating airborne particulate matter on a miniaturised custom chip, which enables elemental identification and assessment of the particles size distribution. In addition to this, leveraging on concepts derived from nanophotonics, by doping the active surface of chip concentrators with specially tailored plasmonic nanoantennas, I study the possibility of co-localised and spatially resolved detection of submicrometric airborne particles, with high resolution and sensitivity which reaches the molecular level.

Relevance of particulate matter detection

Different categories of aerosols, defined as a suspension of liquid and solid particles in a gas[1], are present in our environment, varying in sizes typically from tens of nanometers to tens of microns. A subdivision in three groups can however be done, defining ultrafine particles (diameter below 0.1 µm), fine particles (diameter between 0.1-2.5 µm) and coarse particles (diameter above 2.5 µm). The denomination of Particulate Matter, or PM_x, is therefore used to distinguish airborne particles discriminating their dimension. The term PM_x, in particular, refers to a subdivision of particles based on their ability to pass through size-selective systems where the efficiency presents a cut-off at "x" µm diameters, defining common particles as PM_1, $PM_{2.5}$, PM_{10} [2], though it is usually accepted the use of these terms – in a broader way – to define particles with size below 1, 2.5 and 10 µm respectively.

The presence of PM in the atmosphere is related to different sources, including both human activities like industries, domestic heating, and transport or natural sources (e.g. pollen, sea spray)[3]. Residential, commercial and institutional energy consumption, in particular, are the principal anthropological sources of coarse particular matter (PM_{10}) and fine particular matter ($PM_{2.5}$) generation[3].

Once in the atmosphere, aerosols interact with radiation leading to consequences on climate due to three main effects: the promotion of cloud formation due to the increased number of particles acting as cloud condensation nuclei, the scattering and absorption of radiation (both incoming and outgoing) and changes in the surface albedo resulting from the deposition of particles (typically black carbon) on ice and/or snow covered regions[4,5]. It is clear, however, that the impact of aerosol on climate is not just related to the size of suspended particles, but also to their chemical composition, an aspect that is only partially analysed in ordinary PM monitoring strategies.

Together with the impact on climate changes, arising from the interaction with radiation in the atmosphere, several clinical studies demonstrated in the last decades the negative influence of aerosols on human health[6–8]. A clear example of this issue is the work conducted

in the U.S. by Dockery et al.[9] which examined more than 8000 citizens coming from different regions, between 1970 and 1990, representative of the risks associated with air pollution in the whole country. The study demonstrated a positive linear correlation between mortality and PM exposure which was even stronger when considering exposure to $PM_{2.5}$ alone, independently from risk factors such as age, sex, cigarette smoking and occupational exposure.

It is thus clear the need of instruments and measurement techniques, in this historical period, capable of monitoring the concentration of particles and provide a wider set of measurements for their full characterization. The technology involved in the analysis can strongly vary depending on the property that is to be determined. In their review, Amaral et al. identified the particle concentration as the most relevant property to measure for air quality purpose[10]. However, standard European measurement technique for the determination of PM_{10} and $PM_{2.5}$ concentrations in ambient air[11] refer to gravimetric or optical detection methods, strongly influenced in the first case by ambient conditions (humidity, temperature)[12] or in the latter case by the assumptions of particle uniform shape (spheres) and density as well as the dependency of the smallest detectable particle diameter on the laser wavelength[13]. The previous considerations thus make clear that there is an urgent need of developing innovative sensors, able to explore wider set of PM parameters other than concentration and size distribution. With this respect the exciting and challenging goal is to develop a novel approach to investigate functional characteristics of particulate matter combining on the same instrumentation particles collection and counting, size distribution analysis, elemental mapping with EDX microanalysis, and structural identification with a powerful spectroscopic technique such as Raman scattering.

Nanophotonic approaches to high sensitivity detection of molecules and particulate matter

A fundamental requirement for the optical detection and the application of microscopy techniques to micro- and nanoparticles is that the studied objects should be in the order of the wavelength of used light. This is not always verified in the case of nano-scale particles, which typically display sub-wavelength dimensions and thus require, for the observation, techniques capable of increasing the confinement of light. Nanophotonic approaches address this challenge by manipulation of light at the nanoscale, employing nanostructured materials with tailored shape and composition to achieve unconventional sensitivity, making possible detection at the level of single molecules[14–17].

When incident visible light interacts with sub-wavelength metallic structures, indeed, coherent oscillations of the conduction electrons are excited within the material. This phenomenon, known as plasmonic resonance, is characterized by a frequency strongly dependent on size, shape and material of the involved nanostructure[18,19]. The plasmon resonance leads to local displacement of mobile electron charges with respect to fixed ionic cores, and consequently induces a large enhancement of electromagnetic fields, surrounding

the metallic particle. Nanostructures separated by a few nanometres support coupled plasmons, with hot-spot regions of extremely high field intensity in the gaps between the structures, drastically enhancing optically driven processes[20] and allowing detection of nanometer scale objects [21–23].

Doping sensing substrates with plasmonic nanostructures is therefore a potential route toward the disclosure of unconventional sensitivity in PM monitoring devices[24–26], paving the road for miniaturized and portable sensors[27]. Nanophotonic methods and instruments can be in perspective applied, in parallel with standard monitoring methods regulated by international standards, to enable ever-increasing complexity of the information obtained by collected samples.

As objective of the thesis, I propose the application of plasmonic nanostructures to the functionalization of miniaturized substrates for the collection of aerosol particles, conjugating nanophotonics solutions with the point of view of particulate matter detection at the nanoscale. Applying versatile and stable substrates, moreover, it would be possible to perform different spectroscopic analysis co-localized on the collected particles[28–30], investigating not only the concentration, size, and shape of the micro- and nanometric objects (by electron microscopy), but also their chemical composition (elementary EDX analysis) and molecular structure (vibrational Raman spectroscopy), assuming a key-role potential as complementary approach in parallel with standard environmental monitoring methods.

The thesis is therefore organized in 6 chapters, as follows:

In **chapter 1** the fundamental properties of plasmonic resonances and their application to the enhancement of spectroscopic techniques are introduced, together with the state-of-art technologies for concentrating analytes in sensing platforms and combining co-localized measurements. In conclusion of the chapter, the idea of fabricating a particle sampling substrate based on free-standing membranes is presented.

Chapter 2 is dedicated to the nanofabrication techniques applied during the thesis for the realization of the presented samples. Besides electron beam lithography, the main nanofabrication technique developed for this investigation, I also explored the possibility to adopt different large area methods for the fabrication of periodic gratings and the self-assembled growth of high-density nanostructures.

In **chapter 3**, I provide more technical details regarding the nanofabrication processes and the setups employed. I suggest the reader to consider this section as complementary to the following chapters, where the discussion is focused more on the ideas and results rather than instrumental parameters and recipes.

In **chapter 4**, the nanofabrication of PM collection substrates based on free-standing Si_3N_4 membranes is discussed. Together with the design of the fabricated chip, I report here the

development of a collection prototype and the study of airborne particles production, leading to the validation of the proposed device referring to standard PM collection techniques.

Chapter 5 is focused on the application of fabricated membranes to the co-localized characterization of collected particles. Moreover, functionalization with plasmonic nanostructures is demonstrated to enhance the signal of spectroscopic techniques on the free-standing surface.

In **chapter 6** is presented a parallel application of plasmonic structures to flat-optics sensing of liquid solutions. Two different configurations are reported, one on large-area samples where the structures periodicity is employed to couple localised plasmonic and lattice excitations, the other a miniaturized version designed on the free-standing membrane, where the nanostructures are applied to launch guided modes into the thin substrate. In both cases the plasmonic arrays are employed for sensing liquid samples in terms of their refractive index.

In the **appendix** is reported a work done in the frame of an international collaboration, regarding the application of the large area nanopatterning processes described in Chapter 6 in a different context. The aim here is to fabricate large area templates functionalized with anti-reflection nanopatterns, to be employed as supporting substrates in thin film organic solar cells featuring increased conversion efficiency.

List of related publications

- Mennucci, C., Chowdhury, D., Manzato, G., Barelli, M., Chittofrati, R., Martella, C., Buatier de Mongeot, F., *Large-area flexible nanostripe electrodes featuring plasmon hybridization engineering*. Nano Res. 14, 858–867 (2021);
- Chowdhury, D., Giordano, M. C., Manzato, G., Chittofrati, R., Mennucci, C., Buatier de Mongeot, F., *Large-Area Microfluidic Sensors Based on Flat-Optics Au Nanostripe Metasurfaces*. J. Phys. Chem. C 124, 31, 17183–17190 (2020);
- Manzato, G., Giordano, M. C., Barelli, M., Chowdhury, D., Centini, M., Buatier de Mongeot, F., *Free-standing plasmonic nanoarrays for leaky optical waveguiding and sensing*, Optics Express 30, 10, 17371-17382 (2022);
- Chowdhury, D., Mohamed, S., Manzato, G., Siri, B., Chittofrati, R., Giordano, M.C., Hussein, M., Obayya, S.S.A., Hameed, M.F.O., Stadler, P., Scharber, M. C., Buatier de Mongeot, F., *Broadband Photon Harvesting in Organic Photovoltaic Devices Induced by Large-area Nanogrooved Templates*, under submission to ACS App. Nano Mat.;
- Manzato, G., et al., *Nanofabricated Silicon Nitride Membranes for Miniaturized Airborne particle sampling and co-localized EDX-Raman analysis*, in preparation for submission;
- Manzato, G., et al., *Plasmonic functionalization of silicon nitride nanosieves for Raman-SERS detection of sub-micrometric particles*, in preparation for submission.

Chapter 1 – Plasmon Enhanced spectroscopies and concentrating sensors

In the last decades, a significant fraction of the scientific and technological advances in Materials Science have been driven by the possibility to achieve a wide range of non-conventional physical and/or chemical properties in nanostructured materials. These non-conventional properties, induced in the material thanks to manipulation of the constituent atoms at the nanometer level, can be applied to modify and engineer a broad range of fundamental properties governing the interaction of a substrate/material with its environment (e.g. super-hydrophobic properties induced by biomimetic texturing[31], relevant in self-cleaning functionalization of surfaces; or broadband antireflection effects induced by biomimetic "moth-eye" nanotexturing[32,33], relevant in energy conversion applications). The ability to manipulate light/matter interaction at the nanoscale level turns out to be crucial also in the broader context of advanced spectroscopy and sensing applications. In recent years a very intense research activity has been oriented at understanding and exploiting the extraordinary properties of noble metal nanostructures supporting Localised Surface Plasmon resonances which enable light manipulation at the nanoscale[34–38]. Thanks to the strong plasmonic near-field confinement, an extraordinary sensitivity can be achieved in plasmon-enhanced spectroscopies such as Surface-Enhanced Raman Spectroscopy (SERS)[39–42], capable of detecting weak vibrational signal emitted by a single molecular layer. Similarly, the strong localization of electromagnetic fields in the nanogaps formed between a surface and a special metallic tip, which supports plasmonic modes, is at the base of the extreme spatial resolution obtained in Tip-Enhanced Raman Spectroscopy (TERS)[43–46]. The combination of spectral and spatial resolution achieved by this peculiar nanospectroscopy represents the key ingredient at the basis of innovative devices suitable to handle biomolecules such as DNA (flow through nanopores, labelled functional surfaces) or probing novel atomically thin materials[47–50].

Focusing our attention on the detection of disperse and/or low signal analytes, nanostructures can be exploited to induce phenomena as concentration of electromagnetic fields or selective capture of particles, improving drastically the amount of information that can be obtained when the analyte is available in small volumes or highly diluted conditions. Plasmonic nanoantennas represent a promising opportunity in this direction providing the possibility to resonantly enhance weak signals emitted by the analytes lying in their proximity (hot spots). In parallel novel strategies based on nanopatterned templates can be developed to locally increase molecular concentration, further improving the overall molecular sensitivity.

In this first chapter I will focus my attention on the possibility to enhance the signal of measurements by either concentrating the electromagnetic (EM) field (paragraph 1.1) or concentrating the analyte itself (paragraph 1.2), placing the emphasis on the innovative solutions derived from nanotechnology, exploiting the plasmonic effects of metal structures. In paragraph 1.3, moreover, I will discuss the possibility of exposing concentrated samples

to different techniques, increasing even more the quantity of information that one can extract from a sample. In conclusion of the chapter, in paragraph 1.4 I present the idea of fabricating a particle sampling substrate based on free-standing membranes and suitable for co-localized observations.

1.1 EM field enhancement: Plasmonic resonance in metallic structures

Plasmonic resonances take place when a metallic nanostructure is excited by an external electromagnetic (EM) field. The free electron gas of a nanoscale metallic structure can be driven in oscillation while the heavier positive nuclei remain stable in their position due to their higher inertia. Once the negatively charged electron cloud is displaced, a restoring force between electrons and nuclei forces the system to recover its minimum potential configuration, so that in a simple approximation the dynamics of the system can be treated as that of a forced oscillator. When the characteristic oscillation frequency of the system matches with that of the incident EM wave, the condition for resonant plasma oscillations is satisfied leading to a Localised Surface Plasmon Resonance (LSPR).

A broad range of effects relate to this peculiar behaviour of metallic nanoparticles. In fact, the resonant oscillation of the electron cloud can result in strong absorption and redistribution of the energy delivered by the incident EM wave. Moreover, during oscillation a large net charge is confined in proximity of the nanostructures' surfaces leading to a large enhancement of the local EM field (near-field regime), in the immediate vicinity of the nanoparticle surface with respect to its free-space value. These effects are particularly evident for gold and silver nanoparticles whose plasmon resonance frequencies fall into the visible spectrum and for which damping effects due to carrier scattering are minimised leading to very sharp resonances. LSPRs are non-propagating excitations that can be excited by direct light illumination.

For what concerns the non-propagating modes, these phenomena were theoretically analysed in the framework of electrodynamics by Gustav Mie who managed to resolve Maxwell's equation for a spherical metallic nanoparticle. He found a general expression for the extinction optical cross section as an infinite summation of coefficients a_n and b_n given by spherical Bessel functions[51]:

[eq. 1.1]

$$\sigma_{ext} = \sigma_{scat} + \sigma_{abs}$$

$$\sigma_{scat} = \frac{\lambda}{2\pi\varepsilon_m}\sum_{n=1}^{\infty}(2n+1)(|a_n|^2 + |b_n|^2)$$

$$\sigma_{abs} = \frac{\lambda}{2\pi\varepsilon_m}\sum_{n=1}^{\infty}(2n+1)Re\{(a_n + b_n)\}$$

In the simplest approximation the LSPR can be described in the limit where the particle is much smaller than the incident wavelength ($d << \lambda$). It is the so-called *Quasi Static*

Approximation or *Dipole Approximation* since the problem is reconducted to that of a particle exposed to an electrostatic field and spatial-retardation effects within the volume of the sphere can be neglected. In this approximation the nanoparticle acts as an electric dipole, resonantly absorbing and scattering incident EM fields and the limit is valid for particles with dimension below 100 nm illuminated by visible or near infrared radiation. In this approximation the cross-section can be obtained interrupting the infinite series (eq. 1.1) at the first order in the term (d/λ). Within this approximation we have:

[eq. 1.2]

$$\sigma_{scatt} = \frac{k^4}{6\pi}|\alpha|^2$$

$$\sigma_{abs} = k\, Im\{\alpha\}$$

Where α is the complex polarizability and k is defined as:

$$k = \frac{2\pi\varepsilon_m}{\lambda}$$

For a spherical particle of volume V, the polarizability α_{sph} is given by the Clausius-Mossotti equation (considering only dipolar contributions):

[eq. 1.3]

$$\alpha_{sph} = 3V\frac{\varepsilon - \varepsilon_m}{\varepsilon + 2\varepsilon_m}$$

Where $\varepsilon = \varepsilon_1 + i\varepsilon_2$ and ε_m are the dielectric function of the nanoparticle and the host medium, respectively.

It is worth to notice that, since polarizability depends on particle volume V, it implies a dependence on V^2 of scattering cross section and on V of absorption cross section. Quasi static approximation tells us that for very small metallic particle absorption is stronger than scattering. Moreover, when the denominator of the polarizability function is minimized, a strong enhancement in absorption and scattering cross sections is found, corresponding to the LSPR excitation. It happens when, for small values of the imaginary part ε_2, at a specific wavelength λ_R is satisfied the equation:

[eq. 1.4]

$$\varepsilon_1(\lambda) + 2\varepsilon_m = 0$$

This relation, also known as Fröhlich condition, clearly represents how the plasmonic resonance frequency is determined by particle properties, through ε, and local surrounding medium, through ε_m. For what concerns the dielectric function of the metallic particle in the approximation of quasi-free electrons, we can recur to Drude model to find its expression:

[eq. 1.5a]

$$\varepsilon(\omega) = 1 - \frac{{\omega_p}^2}{(\omega^2 + i\gamma\omega)} \quad ; \quad {\omega_p}^2 = \frac{ne^2}{m\varepsilon_0}$$

Where ω_P is the plasma frequency of metals, n and m are the conduction electron density and effective mass, respectively, and γ is the conduction band electron relaxation rate ($\gamma = 1 / \tau$).

If we solve the Fröhlich condition (eq. 1.4) for a metallic sphere with $d << \lambda$ in air ($\varepsilon_m = 1$) we understand that the free electron gas can resonate with an external field at frequency:

[eq. 1.5b]

$$\omega_0 = \frac{\omega_p}{\sqrt{3}}$$

A reference work in this field is the paper of Otto Muskens et al.[52] where they demonstrate, by recurring to the mentioned equation, that resonance wavelengths of noble metal nanoparticle redshift because of increasing the matrix dielectric constant ε_m embedding the particle.

An interesting case to study is represented by non-spherical particle, in which polarization dependent effects come into play. We now consider the case of an ellipsoidal shape whose size is sufficiently small to guarantee quasi static approximation validity. In sake of simplicity, we consider a prolate spheroid with a long axis a and identical short axes $b = c$ (see sketch in Fig.1.1).

For ellipsoidal nanoparticles, the polarizability α_n along one of the axis directions assumes the following expression[51]:

[eq. 1.6]

$$\alpha_n(\omega) = \frac{V}{4\pi} \frac{\varepsilon(\omega) - \varepsilon_m}{[\varepsilon_m + L_n(\varepsilon(\omega) - \varepsilon_m)]} \quad ; \quad n = x, y, z$$

Where L_n is the depolarization factor which depends on the spatial direction and considers geometrical shape of the particle (e.g., for a sphere $L_x = L_y = L_z = 1/3$).

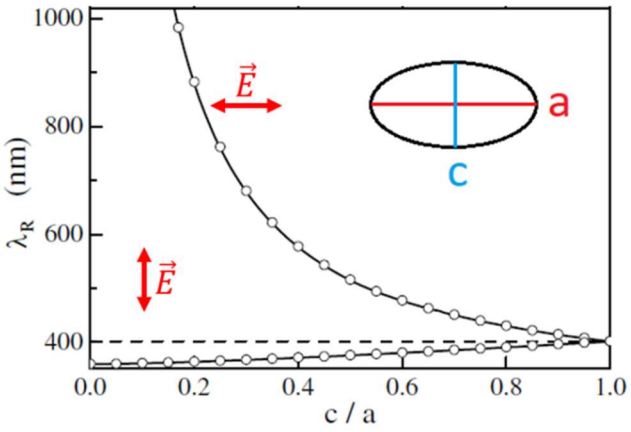

Figure 1.1: Resonating wavelength variation in relation with the variation of the particle aspect ratio. Following the curves, the resonance condition varies differently for polarization parallel (red) or perpendicular (blue) to the long axis (a) of the particle. Adapted from[52].

Similarly to the case of the spherical particle (eq.1.5a), the resonance condition of the spheroid appears as:

[eq. 1.7]

$$\varepsilon_1(\lambda_R) + \frac{1 - L_n}{L_n}\varepsilon_m = 0$$

Eq. 1.7 introduces a degeneracy in the LSPR spectral position with the n-axis. In Figure [1.1] are plotted the resonance wavelengths, λ_R, for the gold prolate spheroid of volume V as a function of the particle aspect ratio, c/a, and for incident light polarized along and across the long axis, a. As the c/a value approaches 1, the particle is reduced to a sphere which resonates at λ = 540 nm independently from the incident polarization. If the aspect ratio is decreased, a red and a blue shift of the resonance are instead predicted for light polarized along and across the long axis respectively. That introduces the possibility to tune the spectral position of the LSPR of a particle by means of modification of its aspect ratio. In the presented equations, moreover, interesting effects concerning plasmonic resonances have been briefly explored including their local sensitivity to the dielectric function of the surrounding medium. This last aspect is of particular importance in view of experiments that will be presented in Chapter 5.

1.1.1 Coupling of periodic plasmonic structures

We have seen that the localized plasmon resonance of a single metallic nanoparticle can be shifted in frequency from the Fröhlich frequency defined by (eq 1.4) via alterations in particle shape and size. In particle ensembles, additional shifts are expected to occur due to electromagnetic interactions between the localized modes. For small particles, these interactions are essentially of a dipolar nature, and the particle ensemble can in a first approximation be treated as an ensemble of interacting dipoles. I will now describe the

effects of such interactions in ordered metal nanoparticle arrays. Here, we assume that the particles of size a are arranged within ordered one – or two – dimensional arrays with interparticle spacing d. We further assume that $a \ll d$, so that the dipolar approximation is justified, and the particles can be treated as point dipoles.

One can intuitively see that interparticle coupling will lead to shifts in the spectral position of the plasmon resonance compared to the case of an isolated particle. Using the simple approximation of an array of interacting point dipoles, the direction of the resonance shifts for in-phase illumination can be determined by considering the Coulomb forces associated with the polarization of the particles. As sketched in Fig.1.2a, the restoring force acting on the oscillating electrons of each particle in the chain is either increased or decreased by the charge distribution of neighbouring particles. Depending on the polarization direction of the exciting light, this leads to a blue-shift of the plasmon resonance for the excitation of transverse modes, and a red-shift for longitudinal modes.

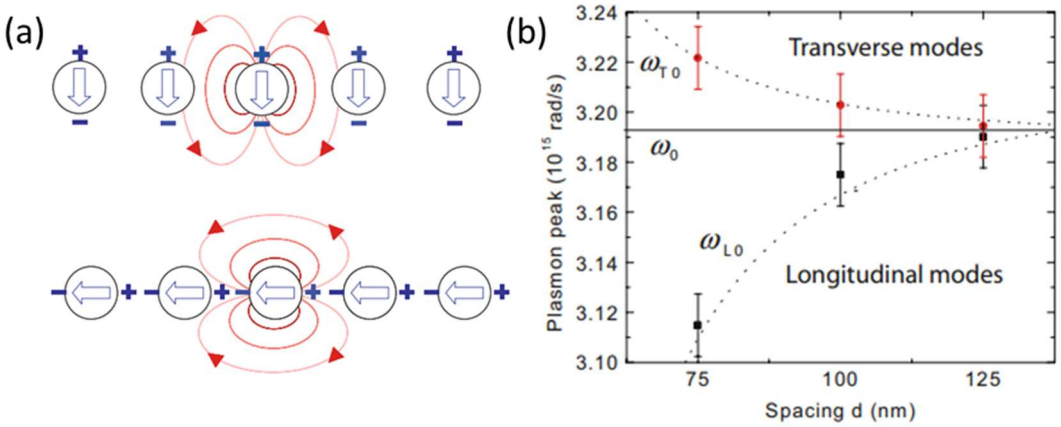

Figure 1.2: Adapted from[34]. (a) Schematic of near-field coupling between metallic nanoparticles for the two different polarization; (b) experimental observation of dependence of the spectral position of the plasmon resonance on interparticle distance.

Using one-dimensional arrays of 50 nm gold particles with varying interparticle distance, these shifts in resonance energy were experimentally demonstrated using far-field extinction spectroscopy[53]. The dependence of the spectral position of the plasmon resonance on interparticle distance is shown in Fig.1.2b both for longitudinal and transverse polarization. Due to the strong scaling of the interaction strength, particle separations more than 150 nm are sufficient to recover the behaviour of essentially isolated particles.

Where two or more metallic nanostructures are in proximity, anyway, the possibility exists for interaction between the modes of the individual nanostructures to form new *hybrid modes*. The case of two interacting particles has been extensively studied. For multiple nanostructures there is also the possibility of coherent interaction arising from multiple scattering. Light that is scattered to propagate in the plane of the particles will undergo multiple scattering by the regularly spaced particles. A geometric resonance arises when the wavelength of the scattered light is commensurate with the periodicity of the array, which,

when it occurs in the same spectral range as the LSPR, may lead to a dramatic modification of the measured optical extinction.

In the coupled dipole approximation, each particle is modelled by a dipole of polarizability α. The particles studied have been described in chapter 1.1 as ellipsoids (semiaxes a, b, and c, volume V), for which the static polarizability (eq. 1.6) can be written as:

[eq. 1.8]

$$\alpha^{static} \propto V \frac{\varepsilon_m - \varepsilon_d}{3\varepsilon_m + 3L(\varepsilon_m - \varepsilon_d)}$$

with ε_m and ε_d the relative permittivities of the metal and surrounding medium, respectively, and L a shape factor. When the particle size is of order 50 nm or more, this expression needs to be modified to account for dynamic depolarization and radiative damping — the so called *modified long wavelength* approximation. We do so by introducing an effective polarizability α^{MLWA} and considering the (homogeneous) surrounding medium which has refractive index n.

When excited by an electro-magnetic wave at frequency ω, a dipole re-radiates a scattered wave in proportion to its dipole moment. The net field on every dipole is therefore the sum of the incident field plus the radiation from all other dipoles, which leads to a system of coupled equations to be solved self-consistently for the total field. Assuming an infinite array, the general solution can be expressed as an effective polarizability α^* for every (indistinguishable) particle:

[eq. 1.9]

$$\alpha^* = \frac{1}{\frac{1}{\alpha} - S}$$

where an array factor S embraces the contribution from the other dipoles and is only dependent on geometrical parameters. In the case of normal incidence, and for a square array of dipoles, this factor is:

[eq. 1.10]

$$S = \sum_{dipoles} e^{ikr} \left[\frac{(1 - ikr)(3\cos^2\theta - 1)}{r^3} + \frac{k^2 \sin^2\theta}{r} \right]$$

θ being the in-plane angle between the dipole locations. The poles of the effective polarizability define the resonances and result from an interplay between the particle properties and the geometrical array factor. When the imaginary part of S is negative, a partial cancellation of the radiative damping has been predicted, thus improving the quality factor of localized surface plasma resonances.

1.1.2 Rayleigh Anomalies and plasmonic lattices

When arranged in the right geometry condition, arrays of gold nanoantennas support collective modes related to their periodic distribution, called Lattice Surface Modes (LSMs), resulting from the coupling of multipolar plasmonic resonances with specific geometrical conditions of the lattice.

The surface and its interaction with an incident EM wave can be schematically summarised as reported in Fig. 1.3[54]:

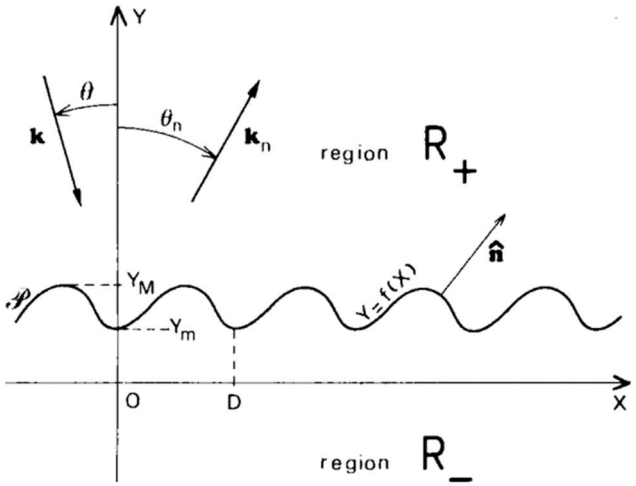

Fig. 1.3: Sketch of an incident beam illuminating a periodic lattice, and the resulting diffraction modes.

The lattice surface is represented by a periodic function f(x) with a maximum height Y_M and a minimal height Y_m, with distribution characterized by a periodicity D. Starting from the lattice periodicity, it is possible to define $\left|\vec{K}\right| = \frac{2\pi}{D}$. Are furthermore defined the angle θ as the incidence angle of the light beam respect to y-axis and the angle θ_n as the angle of the diffracted beam respect to the y-axis. The $\vec{k}$ and $\vec{k}_n$ vectors, in conclusion, being the related wave vectors. The periodic nature of the interface allows an impulse exchange between the interface and the incident wave. More precisely, it is possible to add or subtract to the impulse component of the incident wave parallel to the interface an integer of impulses associated to the lattice ($\vec{K}$). Starting from this assumption, it is possible to obtain an expression for the value of the impulse parallel to the surface of the resulting wave. Such relation is defined as:

[eq. 1.11]

$$\vec{k}_n = \vec{k}_l + m\vec{k}$$

Where the terms referred to the EM wave momentum parallel to the surface can be expressed in relation to the wave total momentum. Assuming that the total momentum is unvaried, one can obtain the following relation:

[eq. 1.12]

$$k_0 sin(\theta_f) = k_0 sin(\theta_i) + mK$$

Stating, finally, the wave momentum module in relation to the light beam wavelength ($k_0 = n\frac{2\pi}{\lambda}$, where n stands for the refractive index of the surrounding medium of the wave) and applying the explicit expression for K. the following relation is obtained, known as *grating equation*[55]:

[eq. 1.13]

$$n_f sin(\theta_f) = n_i sin(\theta_i) + m\frac{\lambda}{d}$$

Where n_i represents the refractive index of the medium where the light is travelling before the interaction with the lattice, while n_f is the refractive index of the interface located in the light diffraction region. Assuming that the final angle is equivalent to 90° or 270°, corresponding to the Rayleigh condition for evanescence, and that the refractive index of the interface before the interaction with the lattice is equal to 1, the following equation is obtained:

[eq. 1.14]

$$m\lambda = d(n_f \pm sin(\theta_i))$$

From the last obtained relation, it is clear to the reader that one is able to tune the resonant wavelength by modification of three parameters: the incidence angle respect to the plane of illumination, the lattice periodicity and the refractive index n_f. Such property enables the realization of simple and versatile systems in the field of "flat optics", where the thickness of the active material is confined to the nanoscale.

The term n_f, in the case of structures with high aspect ratio, has to be exchanged with a term n_{eff} which represents the effective refractive index for the diffracted wave propagation. This distinction is relevant as two effective refractive indices can be identified for the lattice. One in proximity of the external surface of the lattice, and the other corresponding to the interface between the lattice and the underlying substrate. The presence of two effective refractive indices associated to the lattice enables the observation of two distinct Rayleigh modes. The one related to the external surface, in particular, resulting as strongly dependent from the refractive index of the surrounding medium and thus finding application in refractive index sensing (an application that will be discussed in depth in chapter 6). Moreover, despite the weak coupling of multipolar resonances to radiation, LSMs originating from multipolar resonances can significantly enhance the emission of fluorophores. In particular, one can find in literature works[56] that testifies tenfold enhancement of the emission of dye molecules coupled to lattice surface resonances that arise from the diffractive coupling of $3\,{}^{\lambda}/_{2}$ antenna resonances. This enhancement opens the possibility for fluorescence spectroscopies, with large nanoantennas, which are easy to fabricate, that can

be used to enhance signals at shorter wavelengths through the coupling of high-order multipolar plasmonic resonances in arrays.

1.1.3 Plasmonic amplification of the electric field

We have stated that the excitation of LSPR induces, among the other effects, amplification of the electric field inside and in proximity of the resonating nanostructure, and thus becomes extremely interesting to define the geometry of the phenomenon in view of applications in nano spectroscopies enhancement.

Let's consider an isotropic and homogeneous sphere of radius a, placed in the origin of our reference system and inside a constant electrostatic field $\vec{E} = E_0\hat{z}$ (see Fig.1.4). The sphere is surrounded by an isotropic, non-adsorbing medium with dielectric constant ε_m. The response of the sphere is described by the dielectric function $\varepsilon(\omega)$ which we will consider as a complex number ε.

Solving Laplace equation $\nabla^2\phi = 0$ for the sphere we obtain the electric field spatial distribution $\vec{E} = -\nabla^2\phi$ as expression of the potential inside and outside the sphere:

[eq. 1.15]

$$\phi_{in} = -\frac{3\varepsilon_m}{\varepsilon + 2\varepsilon_m} E_0 r\cos\theta$$

$$\phi_{out} = -E_0 r\cos\theta + \frac{\vec{p}\cdot\vec{r}}{4\pi\varepsilon_0\varepsilon_m r^3}$$

Where $\vec{p}$ represents the electric dipole momentum of the sphere equivalent to

[eq. 1.16]

$$\vec{p} = 4\pi\varepsilon_0\varepsilon_m a^3 \frac{\varepsilon - \varepsilon_m}{\varepsilon + 2\varepsilon_m}\vec{E}_0$$

$$\vec{p} = \varepsilon_0\varepsilon_m\alpha\vec{E}_0$$

And α is the electrical polarizability of the sphere, already defined in eq. 1.3.

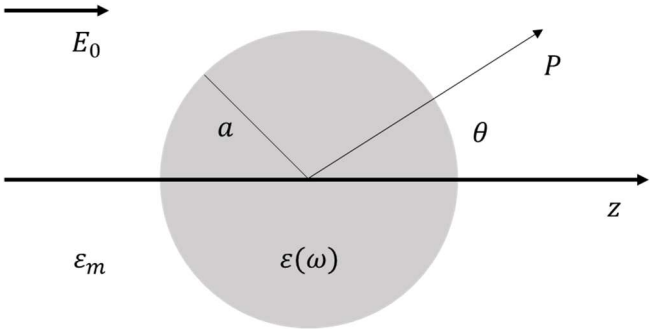

Figure 1.4: sketch of a homogeneous spherical particle of radius a, immersed in an electric field and surrounded by an isotropic, non-adsorbing medium with dielectric constant ε_m.

From eq. 1.9 one can express again the Frölich condition for the excitation of the LSPR, and from the potential definition in eq. 1.8 the behaviour of the electric field inside ($\vec{E}_{in}$) and outside ($\vec{E}_{out}$) the spherical particle can be calculated:

[eq. 1.17]

$$\vec{E}_{in} = \frac{3\varepsilon_m}{\varepsilon + 2\varepsilon_m}\vec{E}_0$$

$$\vec{E}_{out} = \vec{E}_0 + \frac{3\hat{n}(\hat{n}\cdot\vec{p}) - \vec{p}}{4\pi\varepsilon_0\varepsilon_m}\frac{1}{r^3}$$

These equations demonstrate how, in correspondence of resonance excitation, the electric field amplification occurs outside the particle as well as inside it, with a propagation length fading exponentially and thus defining a close-proximity limit to the field enhancement.

The plasmonic resonance modification of the electric field can be detected by various spectroscopy techniques (SNOM, SERS or photoluminescence) and leads to particularly interesting applications in light harvesting[57–59], signal amplification[60–62], photo thermal treatments for medicine, photo catalysis. In the context of the thesis, we focus the attention of the reader on plasmon enhanced fluorescence and Raman-SERS, where the amplification of the EM field enables signal improvement up to three-four orders of magnitude.

1.1.4 Plasmon enhanced fluorescence and Raman-SERS

The Raman effect is the inelastic scattering process between a photon and a molecule, mediated by a vibrational or rotational mode of the latter. Due to the energy exchange during the scattering, the energy of the incoming photon, $h\nu_l$, is shifted by a quantity $h\nu_m$, which corresponds to the energy of the vibrational state. This energy shift can either decrease or increase the energy of the photon respectively depending on weather the involved molecule is in its vibrational state (Stokes scattering) while in the second case the de-excitation of the molecule induces an energy gain for the photon (Anti-Stokes scattering). The frequencies of these two Raman bands are respectively:

[eq. 1.18]

$$\nu_S = \nu_l - \nu_m$$

$$\nu_{aS} = \nu_l + \nu_m$$

In general, the photons involved are not resonant with the molecular levels and the transition is a pure scattering process which takes place via virtual levels. The Raman transition is a pure scattering process even if the incoming photon is resonant with the molecular level of the molecule (i.e., Resonant Raman Scattering), however in this case the emission results to be amplified but its efficiency is still much weaker than that of fluorescent transitions. Moreover, the Raman scattering is a spontaneous linear process where the total power of the inelastically scattered (P_S) beam scales linearly with the intensity of the excitation beam ($I(\nu_l)$). For instance, the power of the Stokes process scales as[34]:

[eq. 1.19]

$$P_S(\nu_S) = N\sigma_R I(\nu_l)$$

Where N is the number of scatterers and σ_R the scattering cross-section.

The intensity if the Raman emission, which is generally very weak, could be enhanced if the Raman-active molecules are placed within the amplified near field of a metallic nanostructure. In this case the process is called Surface Enhanced Raman Scattering (SERS). The Raman amplification could be achieved by exploiting a chemical or, alternatively, an electromagnetic effect. In the first case the Raman cross section σ_R is modified due to a change in environment of the molecules and we expect, from theoretical modelling, a maximum enhancement of the order of 100[34].

On the other side a much more important contribution comes from the increased electromagnetic field in the near vicinity of metal nanoparticles due to the excitation of Localized Surface Plasmon (LSP) resonances and to a crowding of the electric field at the metal interface (i.e., lightning rod effect). The first effect strongly depends on the frequency of the incoming excitation, which excites the resonance only for a minimum of the nanoparticle's polarizability, while the second is a purely geometric phenomenon induced near a sharp metallic feature. In both the cases, the nanoparticles act for the external exciting field as real antennas and for this reason are often called Optical Nano-Antennas (ONAs).

The local field enhancement could be evaluated in terms of the enhancement factor $L(\nu)$, which is defined as:

[eq. 1.20]

$$L(\nu) = \frac{|E_{loc}(\nu)|}{|E_0|}$$

Where $|E_{loc}|$ is the local field amplitude at the Raman active site. In this way we can write the field enhancement factor $L(\nu)$ in terms of the contribution from LSP resonances and lighting rod effect as:

[eq. 1.21]

$$L(\nu) = L_{LSP}(\nu)\, L_{LR}$$

It is further to note as in SERS the amplified near field can play a two-fold role: on one side enhancing the excitation field (i.e., excitation field enhancement) and on the other the Raman emission (i.e., re-radiation field enhancement) which takes place in a resonant wavelength range. We can hence write the total power of the Stokes SERS emission as:

[eq. 1.22]

$$P_S(\nu_S) = N\sigma_{SERS}\, L^2(\nu_l)\, L^2(\nu_S)\, I(\nu_l)$$

Since the difference in frequency $\nu_l - \nu_S$ between the incoming and scattered photons is in general much smaller thanthe spectral range where a LSP resonance is excited we can

approximate $|L(\nu_i)| \approx |L(\nu_S)|$ obtaining that the electromagnetic contribution to the total SERS enhancement is proportional to the fourth power of the field enhancement factor, the so called $E^4\ approximation.$

The enhancement of the power of the Stokes beam can hence be written as[63]:

[eq. 1.23]

$$R = \frac{|E_{loc}|^4}{|E_0|^4}$$

SERS active substrates could be prepared exploiting a wide range of functionalization approaches. Arrays of disconnected nanowires can be exploited [60,62] in order to amplify the Raman signal of Methylene Blue molecules via Localized Surface Plasmon excitation. The selective excitation of an LSP along the wires, behaving as nanoantennas, is expected to induce near-field amplification effects, which are further enhanced if the width of the wire-to-wire nanogap is reduced to the nanometre range and the nanostructures are near field coupled.

In chapter 5 I will discuss a possible approach to this phenomenon, in an application example where metallic structures of size in the order of 50 nm are separated by nanogaps of 10 nm, thus coupling efficiently analyte particles inside the enhanced electric field for spectroscopy signal amplification.

1.2 Nanotechnologies for concentrating sensors

In the application of nano-spectroscopies to low concentrated samples, collection of the analyte itself is a key aspect of its own to be discussed. Depending on the method of analysis taken in consideration, preparation of quantitatively meaningful samples can require days of particle accumulation on large area filters, a standard procedure for collection of airborne particles aiming to gravimetric analysis or chromatography in environmental physics[64–66]. While on the one hand this kind of observation is strongly reliable and regulated by international standards[67,68], it refers to integrated information arising from large numbers of different particles, and therefore lacks the possibility of discrimination between different particles.

Referring to high resolution microscopy and micro-spectroscopy techniques such as Scanning Electron Microscopy (SEM) eventually coupled to X-ray microprobe (EDX) or micro-Raman spectroscopy, the typical fields of view measure hundreds of micrometres on the surface of a sample, with spot resolution well below the micrometre. As stated in the previous chapter, surface functionalization with sensitizers such as plasmonic nanoantennas can be exploited in some instances to increase the signal extracted from the analytes and sensitivity (thus lowering the detection limit).

The combination of plasmonics and Raman spectroscopy has led to extraordinary success of SERS and TERS in detecting even individual molecules by concentrating optical radiation energy in hot spots with areas of just a few nm^2. Such hot spots are however active only in

the optical near-field region, localised within a few nanometres from the surface, and unfortunately in most practical applications the nanoparticles or molecular targets are dispersed in the bulk volume of the carrier fluid where they are free to diffuse, residing most of the time far from the active surface sites.

Conversely large-area sampling filters conventionally employed in air or liquid sampling applications are endowed with a high geometrical cross-section which enables sampling of high volumes of fluid, but at the price of poor signal-to-noise ratio when spectroscopic techniques are employed to analyse the deposited particles since only a small portion of the sensitive area is actively investigated. The reduced sensitive area in a nanospectroscopy application, limited to a few hundred nm^2, thus renders the encounter between the molecules and nanosensor very unlikely. As has been demonstrated[69,70], when the concentration of the solution is close to femtomolar and the linear size of the sensor is in the range of a few tens of nanometres, the accumulation time for the detection of a few molecules is on the scale of days. In other words, nanosensors cannot be used for low-concentration detection (below picomolar concentrations) because the accumulation time is far beyond practical timescales.

The previous considerations suggest the crucial importance of developing new sampling schemes that aim to increase the concentration of the probe molecules/nanoparticles on the active area of the detector. One can e.g. mention approaches based on the use of functionalized plasmonic nanoparticles which spread and diffuse in the solution and bind with the target molecules, in a different approach the fluid to be probed is forced to flow through microfluidic channels that drive the molecules towards the active surface sites concentrated in small area; in a similar approach some groups have proposed to employ perforated membranes that force molecules to pass through nanopores acting as sieves[71,72].

In a particularly significant example propagating Surface Plasmons Resonances excited in thin metallic films are exploited to monitor the interaction of the activated surface with the surrounding medium (as seen in the equations of chapter 1.1). Biacore[73] pioneered commercial Surface Plasmon Resonance (SPR) biosensors offering a unique technology for collecting high-quality, information-rich data from biomolecular binding events. Since the release of the first instrument in 1990, researchers around the world have used Biacore's optical biosensors to characterise binding events with samples ranging from proteins, nucleic acids, small molecules to complex mixtures, lipid vesicles, viruses, bacteria, and eukaryotic cells.

Biacore's optical biosensors are available in several models, displaying slightly different levels of automation and simultaneous analysis capability, but are overall designed around three core technologies: (1) An optical detector system that monitors the changes in plasmonic signal brought about by binding events in real time; (2) An exchangeable sensor chip upon which one of the interacting biomolecules is immobilised or captured, with a bio specific surface where biomolecular interactions occur; (3) A microfluidic and liquid handling system that precisely controls the flow of buffer and sample over the sensor surface.

When a change in mass occurs near the sensor chip surface, e.g. as a result of a binding event of analyte on the bio specific surface, the angle of reflected light at which SPR occurs shifts due to a change in refractive index near the sensor chip surface. A linear sensor records any changes in SPR angle in real time, with responses measured in resonance units (RU, 1RU = 0.0001° shift). These systems are contained within the processing unit, in most cases with robotic operation, and communicate with a computer equipped with control and data evaluation software for self-driven operation of full cycle analysis.

A completely different approach, demonstrated by E. Di Fabrizio and co-workers for liquid samples[74], is based on the idea of exploiting nanotechnology to modify the wettability of a sampling substrate (following a biomimetic approach known as Lotus effect[75]) to concentrate diluted analytes on the functionalized sensing areas (Fig.1.5a). Super-hydrophobic surfaces allowed them to drive and concentrate molecules over a functionalized sensing nano-area (Fig.1.5b, Fig1.5c), where plasmonic electric-field hotspots were used to carry out molecule detection at the single-molecule level in highly diluted solutions, even at femto- or attomolar ($10^{-15} - 10^{-18}\ mol\ l^{-1}$) levels. The diffusion limit can then be overcome, and time accumulation reduced to a few minutes, allowing spectroscopic detection experiments based on fluorescence and Raman scattering even for concentrations at attomolar levels.

Once the analytes are successfully concentrated in a micro- or nanoscale area of the sensor, the subsequent step is to univocally determine the nature of the particles and eventually their position and/or size distribution. In several cases, it turns out that a simple identification of the particulate matter recurring to an elemental composition analysis (e.g., X-ray fluorescence or EDX) is not sufficient to univocally determine the phase of the material. In those cases, it would be highly desirable to study the sample with different analysis techniques, possibly located in different experimental setups or laboratories. This last example highlights the need of a reproducible sample or sample holder which allows to define a stable coordinate reference making possible co-localized experiments performed in different setups.

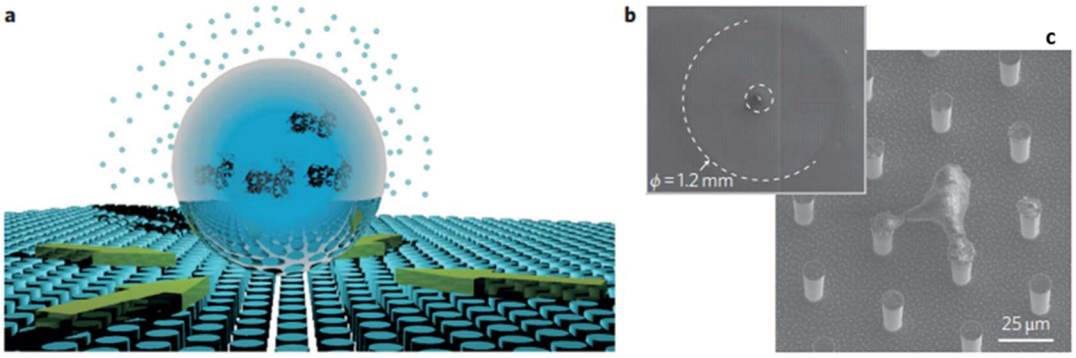

Figure 1.5: Sketch representing the high contact angle and evaporation process with no pinning of the drop and no solute left on the substrate during drop concentration, adapted from[74].

1.3 Co-localized experiments for micro-spectroscopic detection of analytes

The overall understanding of complex samples requires a large variety of scientific instruments based on different techniques[29]. The structural, elemental, chemical, biological, optical, electrical, and mechanical properties of a sample can be imaged at different scales, e.g. from the macroscopic, down to the nanoscopic level, recurring to a variety of scientific instruments and techniques which provide crucial knowledge when they can be combined in a colocalized manner. Taking as an example the trend observed in the study of biological systems, the initial focus has been shifted from simple morphological observation provided by optical microscopy (or by transmission electron microscopy) adding new and complementary information like e.g. the fluorescence signal from tagged regions of the samples. More recently the degrees of freedom have been expanded exploiting the possibility to correlate several other modalities including atomic force microscopy (AFM)[76–78], super-resolution microscopy[79], and Raman microscopy[80].

A similar trend is taking place in other contexts pertaining to material science, environmental science, nanotechnology and condensed matter physics etc. Some modality couplings have developed rapidly in recent years, such as the coupling of scanning electron microscopy (SEM) and Raman microscopy, the former technique providing remarkable structural and atomic information, the latter providing complementary chemical information (examples in Fig.1.6).

To perform observations on the same regions of interest (ROI) using different techniques, scientists have developed various approaches. One approach is to rely on observational skills: navigating over the sample with different instruments, recognizing some given patterns, and recording images in the same ROI. It is then possible to use software that performs precise registration of the images obtained by the different modalities[81]. However, in some cases, the images of a given ROI are very dissimilar between two instruments, because their modalities are sensitive to very different properties of matter, and visual recognition is difficult and unreliable. This is the case, for example, for the combination of SEM and fluorescence microscopy. In all cases, visual spotting of the same ROIs is a tedious and time-consuming process. In other cases, the fields of view of the instruments can be too dissimilar to achieve reliable visual recognition of ROIs. Another difficulty comes from the fact that the different instruments may be in different locations, operated by different specialists, making visual recognition still more unreliable and impractical. As a consequence, scientists have worked out several solutions to allow observations to be performed on the same ROIs with different instruments.

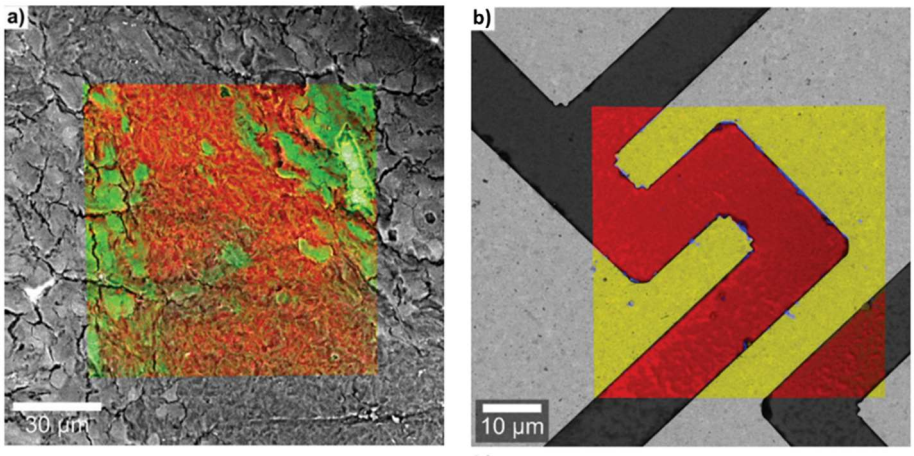

Fig 1.6: Overlay of SEM (grey scale) and Raman (coloured) co-localized images, on organic (a) and inorganic (b) samples. Adapted from [82].

Instrument manufacturers also have crafted solutions to make the process of co-localization between instruments easier. One solution was to create hybrid instruments so that two or more modalities were applied to the same sample, as for example the RISE (SEM-FIB-Raman) instrument produced by TESCAN[82], which enables electronic, ionic and light beams to scan the sample extracting different information in a single chamber. This can be very helpful when the three modalities should be used simultaneously or within a short period. However, the vision of bringing "the best of two worlds" to the same instrument is often confronted by the reality that the instrument constraints are added. This also tends to be costly, making the hybrid instrument more expensive, and less productive, compared to two separate instruments that can be operated simultaneously by two users.

A different – and far way cheaper – option proposed by instrument manufacturers is the application of sample holders (shuttles) that fit on their different instruments with fiducials realising a sample coordinate frame. An example is from BrukerBioMAT Shuttle Stage[83] which allows to colocalise AFM with Optical microscopy modes in upright configuration (e.g. brightfield, fluorescence, confocal laser scanning, FLIM FRET, FRAP, FCS, IR and Raman).

In the next section I will introduce a radically simplified concept in which a nanofabricated sampling chip, allows at the same time low-cost collection and concentration of the analyte and co-localization of particles, generically compatible with standard characterization instruments (SEM, TEM, EDX, Raman).

1.4 Nanofabrication for particle sampling

While aiming at the identification of disperse analytes we can define two key-points as relevant for the sample design: (1) the identification of individual particles or clusters, together with the measurement of their size, that can be performed with SEM or TEM; (2) the identification of elementary composition and/or phases of the analyte units, that can be achieved with Energy Dispersive X-ray Spectroscopy (EDX) and micro-Raman spectroscopy.

In transmission electron microscopy, a typical substrate used to handle samples during the analysis in transmission is an electron transparent, silicon-based, micrometric substrate commercially available under the definition of TEM grid or TEM membrane. Different TEM grids can be acquired from manufacturers, with different possible materials composing the surface and the supporting element (e.g. carbon or polymeric film as surface, supported by a copper grid for mechanical stability) or the geometry of the surface itself, that can be flat and continuous or, for different applications, randomly or periodically porous (e.g. holey membranes by Norcada[84]or TedPella[85]).

In any case, the common aspect is the presence of a thin, electron transparent window (or multiple windows) surrounded by a thicker frame, usually silicon, which can be handled with tweezers and inserted in instrument holders (see Figure 1.7). This geometry is ideal not just for transmission microscopy, where electron transparency is needed for clear reasons, but many works has been published applying them as low-scattering substrates for EBL[86], spin-coating the resist film directly on top of the transparent window and thus creating a condition where quasi-zero scattering is produced below the polymeric film, strongly reducing proximity effects and enabling extremely dense patterning[87]. The same principle applies to EDX measurements, where the reduced scattering leads to low background-noise and improved lateral and vertical resolution.

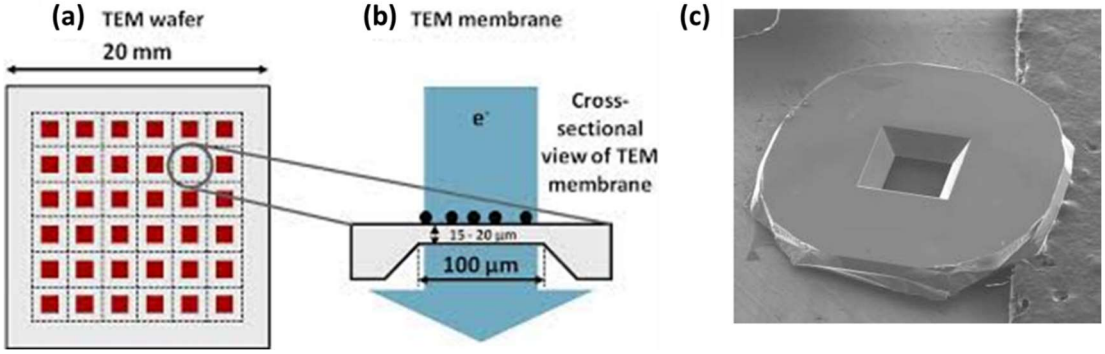

Figure 1.7: (a,b) schematic of a windows array and cross sectional sketch of a 100 micron square membrane. (c) SEM image of a membrane chip, with the central window exposed by diagonal selective etching of the silicon frame.

In the last ten years a great research effort has been done to explore the application of similar systems as filters for the collection of airborne particulate matter – in analogy with our case study – typically taking advantage of the ready-to-use and relatively low-cost electron microscopy chips[88–93] (e.g. Figure 1.8a) or in other cases, mainly in the field of molecular transport through membranes, fabricating functionalized collection substrates with the desired properties (e.g. Figure 1.8b)[94–98].

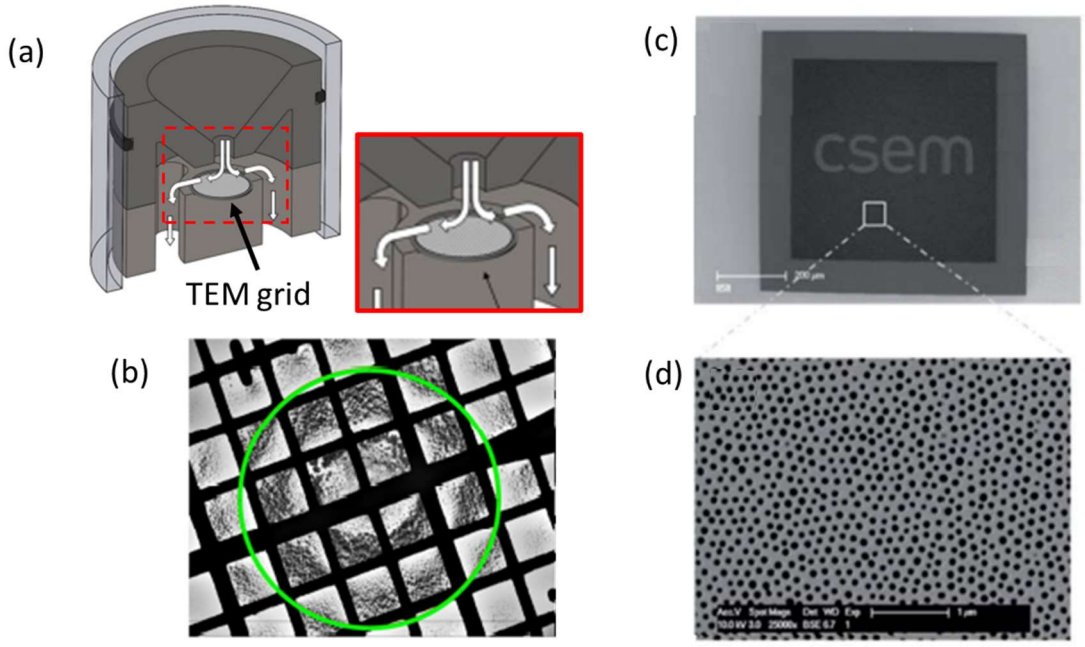

Figure 1.8: (a, b) From Anders Brostrøm et al.[88], (a) drawings of a stage and jet of a micro inertial (MINI) impactor system, with (b) a square mesh nickel TEM grid[99] with thickness 19±5 µm; (c, d) From Franck Montagne et al.[97], (c) SEM picture of a 100 nm-thick free-standing membrane (with a logo in the middle), the scale bar is 200 µm; (d) SEM picture of the nanopores, the scale bar is 1 µm.

The idea of nanofabricating a specifically functionalized membrane chip arises great interest in the development of a collection substrate capable of concentrating nanometric particles (whose dimension would be determined by the pores size) on small areas and will be the focus of the thesis in chapter 4 and 5. With recent advances in microfabrication techniques it has become possible to use lithography to produce well defined nanometre-scale pores with improved chemical and physical properties in comparison with commonly applied polymeric filters[94], and Si-based platforms are particularly attractive due to their chemical and thermal stability, biocompatibility, and potential for precise lithographic control of pore diameter and thickness. Moreover, silicon pores carry potential interest since they have adjustable surface properties through chemical functionalization and are readily integrated into lab-on-a-chip devices[100–104].

In chapter 2 I will introduce several fabrication techniques capable of engineering custom substrates for collection, with a combination of different nanostructure geometries and functionalized properties. In chapter 3 are summarised the details about the instruments and technical aspects that the reader can recall at need, while chapters 4, 5 and 6 – which are focused on the ideas and results of the experimental work – will present the nanofabrication of nanosieve concentrators, the application of such nanosieves as functionalized nanosensors in optical spectroscopies and the realization of plasmonic gratings for refractive index sensing application.

Chapter 2 – Nanofabrication: design of functional properties

Nanofabrication defines in essence the production of nanostructures, generally supported on the surface, independently from the specific technique – or the combination of techniques employed to design the features involved in the various possible applications of interest. There is currently neither a widely accepted definition of nanofabrication nor a definition of where the boundaries between nano- and microfabrication lie. Although one would be tempted to define nanofabrication as the process of making things that are in the single-digit nanometres, in practice a much wider range of dimensions are accepted as nano. The term "nano" started to emerge in the popular and scientific media as the size of electronic devices started to drop below 1 µm[105]. Component sizes that used to be several micrometres gave way to single-digit micrometres, then hundreds of nanometres, and finally down to a few nanometres where they are today. What used to be called "microfabrication" was rebranded as nanofabrication, although many of the basic principles and techniques have remained essentially the same. Although the main driver of this technology has been the manufacture of integrated circuits, there have been tremendous fallout benefits to other areas, including photonics and sensing.

The range of nanofabrication routes toward functional structures is almost as diverse as the materials, applications, and geometries needed for next-generation applications. The approaches can in principle be compartmentalised by separation into either a *top-down* or *bottom-up* definition.

Top-down fabrication refers to methods where one begins with a macroscopically dimensioned material, such as a thin film, into which are placed nanostructured features, thus referring to approaches such as Electron Beam Lithography or Focused Ion Beam lithography. In these cases, either focused electrons or ions are used to carve nanostructures out of larger structures. Alternatively, in the bottom-up approach, one begins to assemble nanostructures from smaller units. Examples include colloidal synthesis, where the colloids are literally assembled from single ions in chemically neutralised solution. Such processes are frequently used for the creation of plasmonic metal nanoparticles or semiconductor quantum dots. Bottom-up assembly also refers to the assembly of larger hierarchical structures, where, for example, colloids self-assemble into larger structures for a particular purpose[106].

Top-down Electron Beam Lithography, or EBL, is mostly applied – commercially – in the production of masters for photolithography[107] but remains a cutting-edge technology for nanofabrication of high resolution, geometrically complex and high density nanostructures. At the beginning of my doctorate, an EBL module was acquired by the research group to upgrade an existing electron microscopy setup, giving me the possibility to define processes and parameters, eventually making the instrument operational as a resource for the laboratory. Several applications of the technique to different materials and substrates have led to interesting experiments that will be discussed in chapters 4, 5 and 6, leading to

different results that share a common starting point and are deeply connected with nanofabrication.

2.1 Nanofabrication by Electron Beam Lithography (EBL)

Nanoscience and nanotechnology have become keywords for scientific development in many areas of research. In the race to build devices with resolution better than 100 nm, the electron beam lithography (EBL) has been one of the most widely used techniques. Among its biggest advantages are the resolution, the registration accuracy, and the large depth of focus. Structures with dimensions smaller than 100 nm can be routinely obtained using conventional resists, and structures even smaller than 20 nm are achieved when special resists and field emission gun (FEG) sources are used[108]. Combining it with its ability to form arbitrary two-dimensional patterns down to the nanometre scale, nowadays EBL is one of the most important techniques in nanofabrication. In short, it involves the exposure by a highly focused electron beam to precisely modify the solubility of a resist material during a subsequent development step.

EBL in its original form was developed using scanning electron microscopes to which a pattern generator and beam blanker are added to control which areas of the viewing field are exposed to the electrons. To this definition corresponds the instrument involved in the thesis experimental work (see chapter 3, nanofabrication methods section, for further information on our EBL setup) but more specialised EBL tools are nowadays common in lithography labs, fully dedicated patterning systems that employ high brightness electron sources for faster throughput, and high-resolution mechanical stages to be able to expose step-by-step large substrates maintaining the narrow field of focus of the electron beam. These direct write systems have the advantage of extremely high resolution and the ability to create arbitrary patterns without a mask. Their disadvantage is the long-time necessary to write large, complex patterns. Efforts to overcome this challenge include projection EBL and the use of massively parallel beams. Our interest in this chapter, however, relies on the technique adopted during the doctorate thesis and thus we will focus on the single beam, scanning EBL technique.

The key objectives of EBL writing are to achieve arbitrary patterns in the resist with high resolution, high density, and high reliability. These characteristics are interrelated in a complex fashion. The key determinants will be the quality of the electron optics (e.g., the ability to create a finely focused spot), the choice of resist, substrate and developer, and the process conditions regarding electron beam energy and dose, development time and temperature. Additionally, depending on the selected parameters, more complications can occur as the delocalization of electrons due to the scattering generated in the interaction with the substrate (proximity effects), collapse of the pattern after development due to swelling and capillarity forces, and fluctuations in the sizes of features (line edge roughness).

2.1.1 Patterning and development parameters

The first requirement for a high-quality beam is a stable, high brightness electron source, such as one employing thermal field emission. The quality of the spot is determined by the electron optics and degree of focus, it is thus necessary to have high positional accuracy with limited astigmatism and small spot size. The electron column is under vacuum to reduce gas scattering of the beam, but divergence of the electron trajectories results from their mutual electrostatic repulsions, which is more pronounced at higher currents and lower energies. However, commercial EBL systems can usually deliver a spot size of just a few nanometres[109–111]. Unfortunately, other factors such as scattering will usually limit the final pattern resolution on the resist: as the electrons enter the film, they begin a series of low energy elastic collisions, each of which will deflect the electron slightly. This forward scattering broadens the beam by an amount that increases with thickness, and this effect is more pronounced at low incident energies (see Fig. 2.1). In addition to forward scattering, there is also backscattering to consider: typically, most of the electrons pass entirely through the resist and penetrate deeply into the substrate, but a fraction of those electrons will eventually undergo enough large angle collisions to re-emerge into the resist at some distance from the point at which they left it. At higher energies, these backscattered electrons may cause exposure microns away from where the beam entered, and this leads to the so-called *proximity effect*[112] where electrons writing a feature at one location increase the exposure at a nearby feature, eventually causing pattern distortion and overexposure. The density of features becomes an important factor in determining the writing parameters in relation to proximity effects, and backscattering is usually minimised as much as possible by modification of the beam conditions or, in some cases, modifying the pattern geometry to compensate the broadening of the features (e.g. reducing the lateral size of a dense array of stripes[113]). Another electron transport phenomenon to be considered is the production of secondary electrons, low energy electrons (a few eV to a few tens of eV) generated by ionizations resulting from inelastic collisions of the primary incident electrons. Because of their energy, secondary electrons travel shorter distances in the sample (several nanometres) but may ultimately limit the resolution achievable with EBL. A final issue, related to the selected substrate geometry, treatments and material, is electrostatic charging[114]. Particularly when writing onto an insulating substrate, if there exists no pathway for the absorbed electrons to dissipate, charge will build up and defocus the electron beam. In such cases, a thin metal or conductive polymer layer is required above or below the resist.

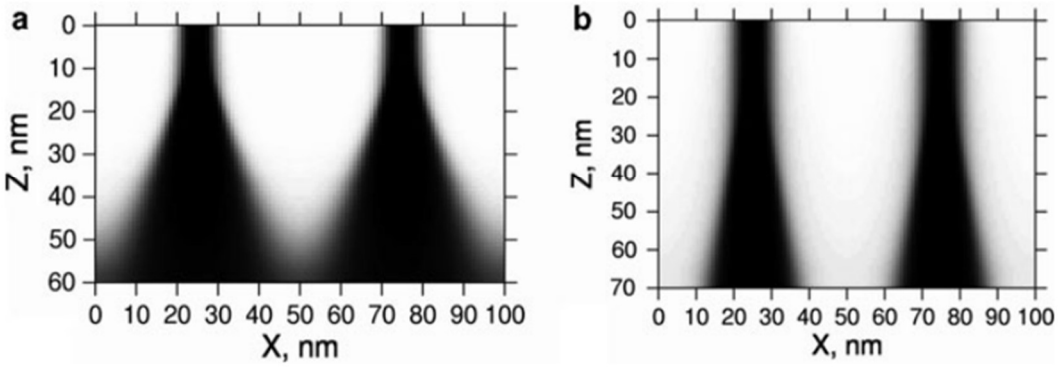

Figure 2.1: From[108]: Electron beam broadening due to forward scattering in the resist at (a) 3 keV and (b) 10 keV of incident energy. Shown is a predicted cross-section of resist exposure for two parallel lines.

Exposure of the resist polymer causes in the film inelastic collisions of electrons with the polymeric chains, resulting in their ionisation (secondary electron generation), which is accompanied by physico-chemical changes in the resist as increased solubility in a solvent (in the case of positive resists). Just as with optical lithography, EBL can employ two classes of resist: positive tone resists undergo a conversion from low to high solubility upon exposure to electrons, the classic example is PMMA (poly-methyl methacrylate) which is characterised by a long chain polymer that is broken into smaller, more soluble fragments during the exposure to the electron beam. In a negative tone resist, in the opposite way, electrons convert the material to low solubility. The prime example here would be HSQ (Hydrogen silsesquioxane) which undergoes a cross-linking reaction to combine smaller polymeric chains into larger, less soluble ones.

After exposure, the resist is typically immersed in a liquid developer to dissolve the fragments (positive tone) or non-cross-linked molecules (negative tone). Temperature and duration become important parameters here as the hotter/longer the development, the farther along the continuum of solubility the dissolution extends. For example, cold development of PMMA freezes out the development of all but the very smallest fragments, resulting in very high resolution as much of the scattered electrons cause insufficient exposure to reach this threshold.

Exposure and development are interrelated as short exposure with long or aggressive development can be equivalent to heavier exposure with short development. As the required resolution increases, the kinetics of the dissolution process becomes quite important to the optimization of EBL, necessitating understanding of these factors at a detailed level. Often a mix of solvents (such as 1:3 methyl isobutyl ketone with isopropyl alcohol for PMMA) is used to tailor dissolution behaviour. An issue that arises if the resist is overdeveloped is the degradation of the resist-substrate bond and the capillarity forces that result as the solvent is removed. These lead to the mechanical failure of the resist structure resulting in pattern collapse, with adjacent linear features particularly vulnerable to this problem, especially for thick resists. Figure 2.2 shows examples of underexposed/underdeveloped structures

(Fig.2.2a, Fig.2.2b), pattern collapse (Fig.2.2e, Fig.2.2f) and optimized fabrication (Fig.2.2c, Fig.2.2d) in PMMA.

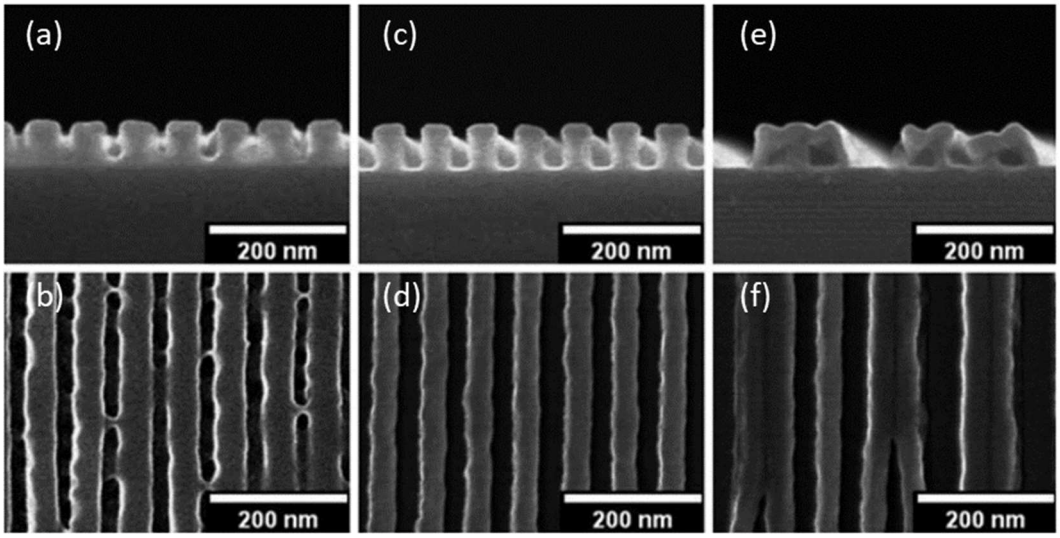

Figure 2.2: PMMA grating structures in cross-section (top) and plan view (bottom) SEM images. (a,b) underexposed or underdeveloped structures; (c,d) optimized writing dose / development time; (e,f) collapsed patterns due to overexposure and/or overdevelopment[115,116].

2.1.2 Application of metallic back-etch masks

Application areas such photonics, nanoelectronics, and bio-nano-electromechanical systems (bio-NEMS) require fabrication of large, macroscopic-scale arrays of nanoscale features, often involving fabrication of transparent nanostructured masters[107]. Dielectric materials appropriate for this purpose present a difficulty when employing EBL for their nanostructuring, as said, because unlike with conducting and semiconducting substrates, lead to charging phenomena and consequent deflection of electron trajectories. The solutions revolve largely around usage of conducting anti-charging layers[117]. An example where a metallic anti-charging layer is located underneath the resist is given in Fig.2.3. In this approach, usually referred to as *Back-etch lithography*, a UV transparent fused silica (FS) substrate is initially coated with a sputtered 30 nm Al film, followed by spin coating a 60 nm layer of PMMA resist on top of it. In this PMMA/Al/FS scheme, the Al layer works as a charge conduction layer during e-beam exposure, and subsequently works as a hard mask for pattern transfer into the FS substrate via glass etching, enabling high resolution on the insulating silica master.

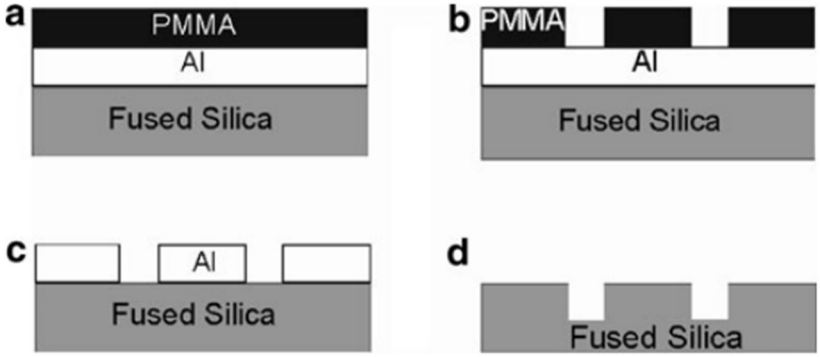

Figure 2.3: From[108]: dielectric mask fabrication schemes. (a) The insulant substrate is coated with Al and PMMA; (b,c) patterns are generated by e-beam exposure in the PMMA; (c) the pattern is transferred to the Al layer using dry etch with PMMA acting as the etch mask; (d) final etching of the pattern into the glass substrate, with the Al layer acting as a hard mask before its removal from the fused silica surface.

The metallic mask can be then removed from the substrate using suitable chemicals that affect only the coating film (e.g. Aqua regia for gold, PAN solution for aluminium). A negative side effect of this method is the edge roughness that occurs because of the granular nature of the film, formed during metal film deposition by sputtering. Although the grain size can be decreased by carefully selecting the conditions of deposition and the metal, the roughness in the released fused silica pattern caused by the metallic grains is a quite common challenge of this approach. Of course, the grain effect is absent when applying a layer of conducting polymer instead of a metal layer, in which case the multi-layer is spin coated with the polymer on top of the EBL resist (conductive coating/PMMA/FS scheme).

EBL is thus a complex nanofabrication process, with many interrelated parameters that affect the quality of the resulting nanofabricated structures and the robustness of the process. So far, I presented the key-elements which led to some critical decisions that have been faced during the fabrication of the samples involved in the thesis, whose details will be discussed thoroughly in chapters 3 and 4.

2.2 Large area nanofabrication by Laser Interference Lithography

While we already defined in detail the advantages of a top-down nanofabrication method as EBL for the fabrication of features concerning our interests, it is worth mentioning a different top-down technique, which finds its strength in fabrication of large area samples.

Laser interference lithography (LIL) is a method to produce periodic structures using two interfering, highly coherent light beams, with resulting structured areas reaching square centimetres[118]. Typically, light from a source is divided and recombined, forming a periodic intensity pattern that can be recorded by the exposure of a photosensitive substrate. Thomas Young first demonstrated the interference of light in 1801, his famous interference experiment gave strong support to the wave theory of light showing interference fringes created when a coherent light source (a flame) was shining through double slits. Nowadays,

lasers produce intense beams of monochromatic (single frequency) light, where all the waves across the beam are in phase. If we use a laser beam to illuminate two slits, which are narrow to ensure adequate diffraction, the diffracted beams from the two slits overlap causing the superposition of two light waves, which appears on the screen as alternate dark and bright bands, called *interference fringes*. The bright fringes are caused by constructive interference and the dark fringes by destructive interference.

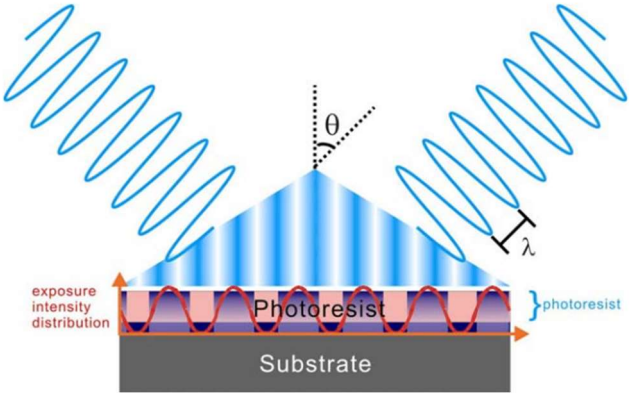

Figure 2.4: Interference of two coherent light waves and the resulting intensity profile in a photoresist layer. The intensity of light impinging on the photoresist is depicted as a sinusoidal curve along the surface.

For lithographic applications, the most intuitive way to form a set of interference fringes is simply to split a beam into two, and then recombine the two beams. The intensity distribution of a superposition of two plane-waves will give a spatial structure that is non-uniform, known as sinusoidal form (Figure 2.4). Under the assumption of symmetry of incidence angle, the periodicity of the fringe pattern of two interfering beams can be simply described with Eq. 2.1, where λ is the wavelength of the beams and θ is the half angle between the two incidence beams:

[eq. 2.1]

$$p = \frac{\lambda}{2\ sin\ \theta}$$

Where p corresponds to the periodicity of the obtained pattern, λ is the wavelength of the laser and θ the angle calculated between the incidence axis and the surface of the sample. This means that by rotating the stage where the sample is mounted (or shifting the incidence direction of the laser) one can finely tune the periodicity of the formed interference pattern and thus the duty cycle of the lithographic pattern.

With this simple relation, periodic and highly ordered nanostructures can be fabricated on large area samples using a simplified configuration of a Mach-Zehnder Interferometer[119]. A UV laser is split in two arms which are recombined using a set of mirrors. Spatial filters in

each arm serve to expand the beams for dose uniformity over a large area and to remove the spatial frequency noise. Due to the long propagation distance and the lack of additional optics after the spatial filters, the beams interfering at the substrate can be accurately approximated as spherical. A set of sensors and a compensation system are used to correct the phase errors. The whole setup should be placed on an actively damped optical table in order to filter the vibrations.

However, accurate positioning and precise alignment are required to produce a single grating structure with Mach-Zehnder Interferometer. When the grating periodicity has to be changed, a complete and time-consuming re-adjustment of the whole optical setup has to be pursued, which limits the flexibility of Mach-Zehnder Interferometer in many cases.

In a recent paper published with my contribution[120], we addressed fabrication issues applying an alternative variant of LIL which enables the production of plasmonic structures periodically arranged over large area (cm^2 scale) on low cost, transparent and flexible substrates (e.g., soda-lime glasses or polymer films like Arylite™). The implied setup is a rather simpler alternative to the Mach-Zehnder Interferometer since it uses a single mirror to recombine the laser emission directly in front of the sample surface. More details about the setup components can be found in the dedicated section of Chapter 3.

Among all possible geometries, in this work we explored the fabrication of 1D-periodic gratings. The pattern fabricated in this configuration can be applied as a mask for the evaporation of metallic nanostripes but can also work as anisotropic transparent electrodes when contacts are placed at the edge of the sample in the longitudinal direction of the wires. In particular, we have fabricated structures directly on glass or polymer substrates, typical transparent window layers employed in photovoltaic or bio-sensing applications. We also demonstrated that the LIL nanofabrication process can be extended in the third dimension to produce dimeric plasmonic structures consisting of vertically stacked (Au/SiO2/Au) nanostripes separated by nm-scale dielectric gap (see Fig. 2.5). Thanks to the homogeneity and stability of the resulting LIL structures, the three material layers can be evaporated subsequently without removal of the mask, undergoing mounting in different deposition chambers, and being exposed to a non-controlled atmosphere.

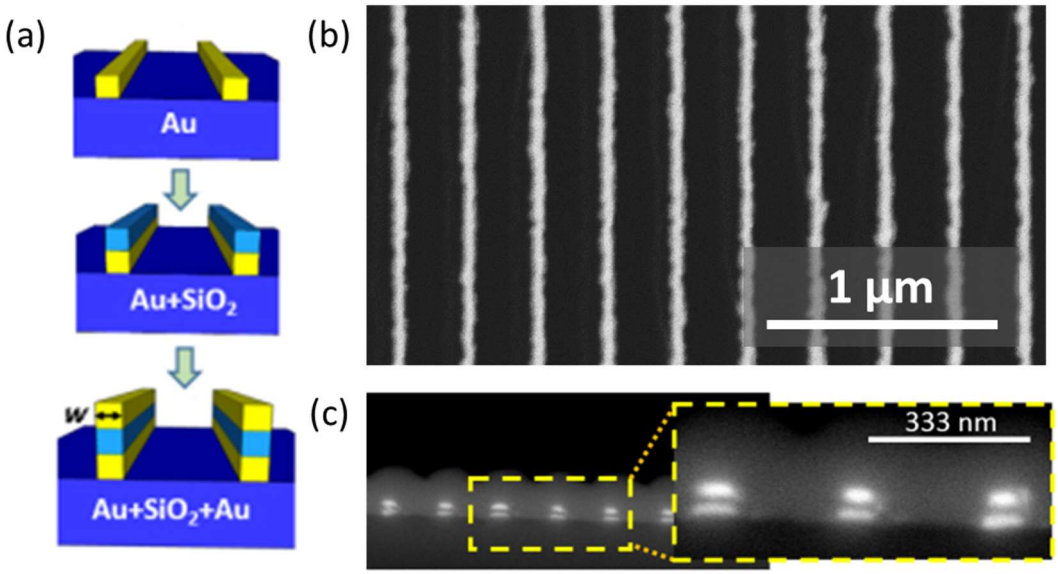

Figure 2.5: From[120]: (a) sequential steps of the nano-dimer formation process; (b) SEM image acquired through backscattered electrons channel demonstrating the lateral thickness and periodicity of the structures; (c) SEM micrograph on the cross-section of the Au/SiO2/Au sample.

Thanks to the highly periodic lateral arrangement of the plasmonic nanostripes obtained with LIL fabrication, it is possible to engineer coherent light scattering from the array into sharp optical modes related with the pattern periodicity, leading to strong amplification of the local electromagnetic field[121] and qualifying the transparent electrodes also as multifunctional templates featuring enhanced photon harvesting in the NIR spectral range with possible applications ranging from nanospectroscopy and biosensing to photovoltaics.

Another application of LIL-fabricated samples studied during the period of my PhD is the functionalization of transparent substrates for nanofluidics and, more precisely, RI sensing performed exciting Plasmonic Lattice modes. More details about this matter will be given in Chapter 6, where this work with LIL and a new application of EBL on membranes are presented.

2.3 Self-organised nanofabrication

As mentioned above, top-down fabrication approaches have the advantage of locally and precisely modifying the surface of a sample, achieving high resolution and control on the morphology of nanostructures whose typical size could be reduced until the range of nanometers. On the other side, anyway, top-down methods present limitations due to the high cost of the processes and to the long time required to pattern large areas. Alternatively, bottom-up techniques induce the formation of nanopatterns over large areas by exploiting the physical and/or chemical properties of atoms and molecules on the surface. In this way large area patterns can be obtained in a cost-effective way, with a strong advantage in terms of scalability of these templates to real-world applications.

However, a crucial aspect of the "bottom-up" method is the control of the size, shape, and order of the nanopatterns tailoring the chemical and/or physical variables that drive the pattern formation. In this context particularly relevant are the physical nanopatterning approaches based on the self-organisation. Indeed, by exploiting the physical properties and the interactions of the atoms at the surface, a strong control of the local morphology can be achieved over uniform large-area templates. In this way ordered arrays of nanostructuctures can be fabricated going beyond the conventional bottom-up random nanoparticles ensemble, typically achieved by conventional chemical approaches. In this section a brief overview of the self-organised nanopatterning approaches studied during the thesis is provided.

2.3.1 Ion beam sputtering

Among the range of self-organised physical approaches, the use of defocused ion beam sputtering (IBS) has gained a growing attention due to the ease of implementation, the flexibility and the scalability over macroscopic substrate areas employing standard industrial equipment. A wide range of planar substrates, after irradiation with noble gas ions at energy from few hundreds of eV to several tens of keV develop ordered nanoscale patterns over large surface areas. When the ion fluence exceeds 10^{16}-10^{17} ions/cm^2, a rich variety of nanostructures can be observed depending on the material and the sputtering conditions, in particular on the incidence angle of the ions[122].

IBS with a defocused, low energy ion beam provides a very useful tool for synthesising nanoscale periodic structures. Depending on sputtering conditions, different morphologies such as ripples or dots are induced by the self-organisation process. The model proposed by Bradley and Harper in 1988 explains, starting from Singmund's theory of sputtering, the evolution of ripple pattern on amorphous surfaces under ion beam irradiation. The starting idea is that the sputtering rate of material in a point is proportional to the power dissipated there by the incoming ions. They transfer their kinetic energy to the atoms of a thin surface layer generating secondary collisions. A small fraction of the atoms is sputtered away while adatoms and vacancies are formed in a surface layer which is amorphized. The erosion velocity in a generic point depends on the energy released locally which is higher for valleys (local positive curvature) than for through (local negative curvature). On the other side thermal and/or ion induced diffusion of the mobile species (i.e. adatoms, vacancies) reduce the interface width. The evolution of an ordered ripples profile is hence due to the interplay between the ion induced roughening and the relaxation mechanism on the surface.

In a work from A. Toma et al.[123], is reported the development of an application of this rippling phenomenon for the physical synthesis of laterally ordered self-organised arrays of metallic nanowires, supported on nanostructured dielectric templates (Fig.2.6). The method, based on a combination of nanoscale patterning of the glass substrate by ion beam sputtering with shadow deposition of the metal nanoparticles, provides a viable alternative to time consuming serial nanopatterning approaches. Far-field optical characterization demonstrates that the nanowire arrays exhibit tunable anisotropic properties in the visible range due to the excitation of localised plasmon resonances.

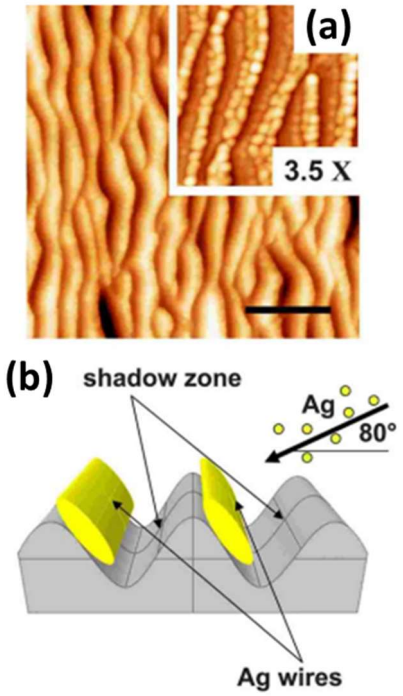

Figure 2.6: Adapted from[123]. (a) AFM morphology of the nanostructured glass substrate after Ag deposition (scale bar 600 nm). The inset shows a 3.5x zoom of the NW array. (d) Experimental geometry adopted for the shadow deposition of the Ag NWs: the nucleation takes place preferentially near the top of the illuminated regions.36

2.3.2 Self-assembled growth of plasmonic features

In the case of very thin or organic substrates, such as polymeric thin films or membranes, ion beam sputtering is precluded by the intrinsic mechanical stability of the material. To fabricate equivalent self-organised structures on such substrates is therefore necessary to take on a non-damaging approach, as can be the idea of exploiting *self-shadowing* of the growing film (in the sub-monolayer state) to create structures, instead of the *geometrical shadowing* related to topographical features discussed in the previous paragraph.

The technique of glancing angle deposition (GLAD) allows the production of highly porous thin films which may enable applications in the production of catalytic surfaces, microsensor elements, micro sieves, low dielectric materials, and optical circuitry components[124]. The design and engineering of GLAD films for specific applications will require a thorough understanding of the dependence of the film morphologies on the details of the deposition process, including the deposition rate, the angular distribution of the incident vapour flux, the film and substrate temperature, the energetics of the surface-substrate interface, and the partial pressure of residual gases in the deposition chamber.

Essential features of GLAD film morphology may be explained by the two competing mechanisms of self-shadowing and temperature-dependent surface diffusion[125].

In a key study performed at Toyota in 1989, a number of metal oxide films were deposited over the range $0° \leq \theta \leq 80°$, where the angle θ is the angle subtended by the incoming flux

and the outward substrate normal. If the angle remains highly oblique ($\theta \geq 80°$) during deposition of a film, significant porosity may be achieved.

During the growth of obliquely deposited films, the highest features of the film will geometrically shadow other surfaces from direct impingement by the incoming vapour flux. Surfaces which have been shadowed in this manner may subsequently grow only by some mechanism other than direct impingement, for example, by indirect impingement by vapour atoms which have been previously scattered, reflected, or desorbed, or by surface diffusion of adatoms from a non-shadowed surface. The self-shadowing mechanism leads to voiding within the film and, under conditions of collimated vapour flux, elongated columnar structure. Self-shadowing and diffusion length become the predominant mechanism in determining morphology at high incident angles.

Most theoretical and practical studies on GLAD and, indeed, on obliquely deposited films, in general, have been concerned with deposition on initially smooth substrates. In this case, film nucleation takes place at random locations on the substrate, and the resulting film structure becomes one of randomly distributed columns. Strong growth competition among the unevenly sized columns leads to column broadening and extinction, as well as to variations in the film porosity[125,126]. However, for many GLAD applications, a periodic distribution of the columns is required, and even in applications that strictly do not need periodic orientation of the columns, the inter-column competition and randomization of column diameters remain undesirable growth effects. To introduce regularity and periodicity into GLAD films, substrates must be prepared with a topography that stimulates nucleation at specific sites. Invariably, this involves the fabrication of arrays of small bumps—or "seeds"—on the substrate prior to the GLAD process.

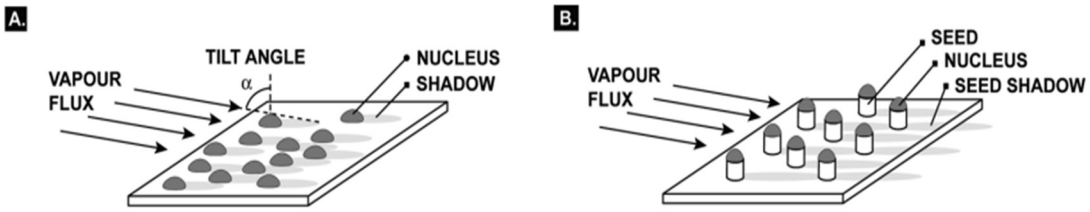

Figure 2.7: From[127], (a) When GLAD is performed on a smooth substrate, the initial flux nucleates randomly on the substrate, resulting in a film with randomly distributed structures; (b) when GLAD is performed on a substrate with a seed layer, the seeds and their shadows enforce periodic nucleation, and yield a periodic film structure.

The principle of periodic GLAD thin films is to replace random nucleation on a smooth surface with enforced nucleation on a layer of seeds, where the raised height of each seed precipitates nucleation of the obliquely incident flux (see Fig.2.7). When GLAD is performed on a smooth substrate (Fig.2.7a), the initial flux nucleates randomly on the substrate, resulting in a film with randomly distributed columns. However, when GLAD is performed on a substrate with a seed layer (Fig.2.7b), the seeds and their shadows enforce periodic nucleation, and yield a periodic columnar film structure. The size and shape of the seeds are,

thus, critical, whereas the composition is of little importance and independent of the GLAD film material being deposited. The ideal periodic GLAD film consists of one column growing off each seed, with no film growth occurring between seeds, and to achieve this the seed patterns must be designed to match the intended film structure while taking into account the growth effects inherent in the GLAD process. Since GLAD is performed on low-temperature substrates, the impact of thermal effects on adatom transport and column growth is negligible, and only geometrical effects have to be considered.

In chapter 5 a similar process will be discussed, where the glancing angle deposition of gold $\theta = 80°$ without periodic seeds was performed to create randomly disconnected sub-monolayer films. Such structures are capable of sustaining plasmonic excitations and therefore performing local concentration of EM field on top of surfaces that could not be nanofabricated by ion beam sputtering modification.

The peculiar optical properties of metasurfaces described within the present chapter, and their application in combination with optical spectroscopies, will be crucial for the core activity of my thesis focused on the development of novel functional sensors with impact in photonics, biosensing and environmental detection. To reach this final goal an intense work of nanofabrication has been performed exploiting and optimising both the high-resolution top-down techniques (EBL) and the latter large scale, self-organised approaches.

Chapter 3 – Nanofabrication methods

In this chapter are collected technical information regarding the fabrication setups implied in the thesis. Since a remarkable effort has been dedicated during my doctorate to the development of new processes and the design of custom setups, this separated section – focused on quantitative and specific information – is a supplement to the following chapters, where more emphasis is dedicated to the discussion of ideas and results.

3.1 Vacuum chamber for thin film deposition

The ultra-high vacuum (UHV) chamber implied for the deposition of metallic/dielectric films during the thesis is a custom chamber built and equipped with several tools for sample preparation, and a manipulator which permits three dimensional shifts in x-y-z and rotation movement around the z-axis in order to face the sample towards the various instruments and also sample annealing up to 500°C using resistive sample heaters embedded in the copper sample holder. As shown in Fig.3.1, in the bottom part of the chamber are located two custom built evaporation crucibles for thermal sublimation of metals (physical vapour deposition), while in the top part of the vacuum vessel a quartz crystal microbalance allows to monitor the evaporation flux. The chamber also houses a high flux ion gun based on a microwave ECR plasma source (by Tectra®) for defocused Argon ion beam sputtering and nanopatterning applications. The vacuum in the chamber is obtained combining a preliminary low vacuum stage (reaching pressures of about 10^{-2} mbar) based on a dual stage rotary pump (Leybold Trivac B), with the high vacuum stage based on a 360 l/s turbo molecular pump (Leybold TURBOVAC360) with nominal vacuum limit in the order of 10^{-10} mbar. Chamber vacuum is monitored with a Pirani sensor in the low vacuum range and an ion gauge measuring high vacuum between 10^{-3} and 10^{-10} mbar. During metallic film deposition experiments, the typical operation conditions imply base pressure of about 10^{-7} mbar. For ion beam sputtering, starting from an analogous base pressure, Argon gas is introduced in the chamber by means of a fine leak valve, reaching the operating pressure of 4 in 10^{-4} mbar necessary for the ignition of the plasma of Ar^{+} ions.

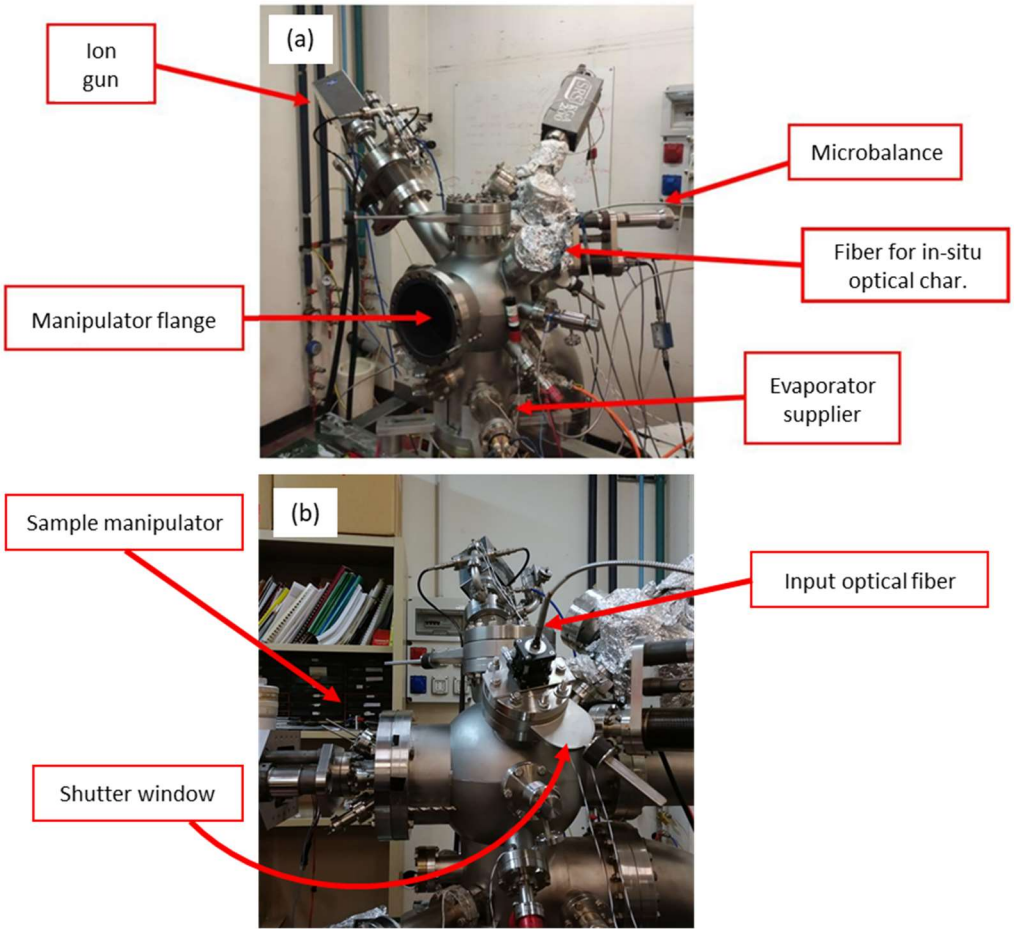

Figure 3.1: Components of the sample preparation UHV chamber. (a) Front-view image of the open chamber, with labels indicating the manipulator entrance, ion gun, microbalance, optical fiber and evaporator; (b) lateral-view picture of the closed chamber, with label indicating the sample manipulator and a clear view of the optical fiber connection to the chamber.

A fundamental component for monitoring in real-time the experiments reported in the thesis is the in-situ optical characterization module (labelled in Fig.3.1b). A pair of optical fibers, coupled to a solid-state spectrometer (Ocean Optics® HR 4000) and a broadband Deuterium-Halogen light source (DH-2000-BAL Ocean Optics) are connected to the vacuum chamber via collimating lenses which form a collimated beam (diameter 4mm) in coaxial configuration for transmission measurements. The optical beam enters the vacuum chamber through two CF40 ConFlat viewports located at an angle of 45° and crosses the centre of the spherical chamber along one of the diameters protected by magnetic shutters (Fig.3.2a). Thanks to the four degrees-of-freedom of the sample manipulator it is possible to align the sample holder plate orthogonally with respect to the optical beam, so that the optical beam is centred coaxially with a 5mm hole which traverses completely the holder allowing safe mounting of a sample for optical measurements in transmission configuration, as reported in Fig.3.2b and Fig.3.2c. This feature enables monitoring in-situ and in real-time the optical properties of the nanostructures during the modification of samples, allowing a fine tuning of the desired optical properties.

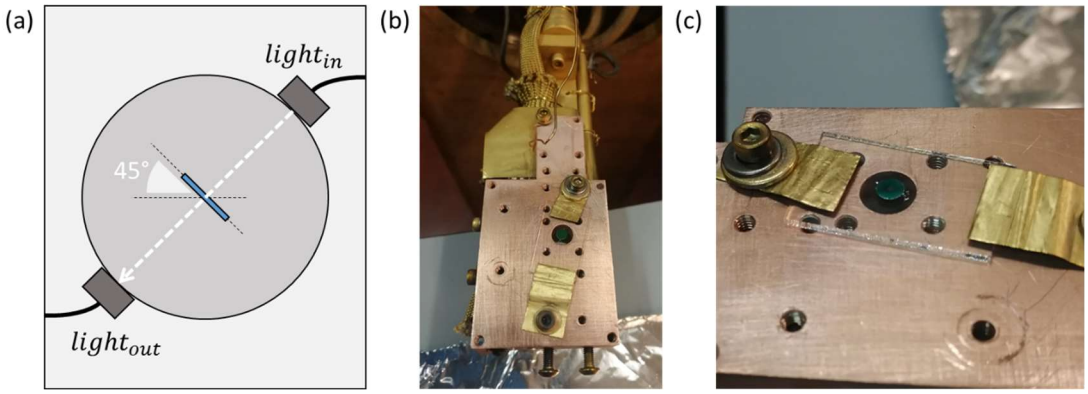

Figure 3.2: In-situ optical characterization module of the UHV chamber. (a) sketch of the geometrical position for the manipulator allowing transmission of light through mounted samples; (b) picture of the manipulator rotating plate, with a sample mounted on the transmission hole, and (c) detail of a membrane chip mounted on the hole.

3.2 Laser Interference Lithography (LIL)

The Laser Interference Lithography nanofabrication process presented in chapter 2.2 has been developed in the laboratory as a custom-built prototype. The setup has been conceived as a compact and low cost version of a Mach-Zehnder Interferometer in Lloyd configuration (see Fig.3.3a) with the sample application of a perpendicular mirror recombining the light with periodic interference phenomena directly onto the sample surface (Fig.3.3b,c), creating a highly-homogeneous pattern (Fig3.3d).

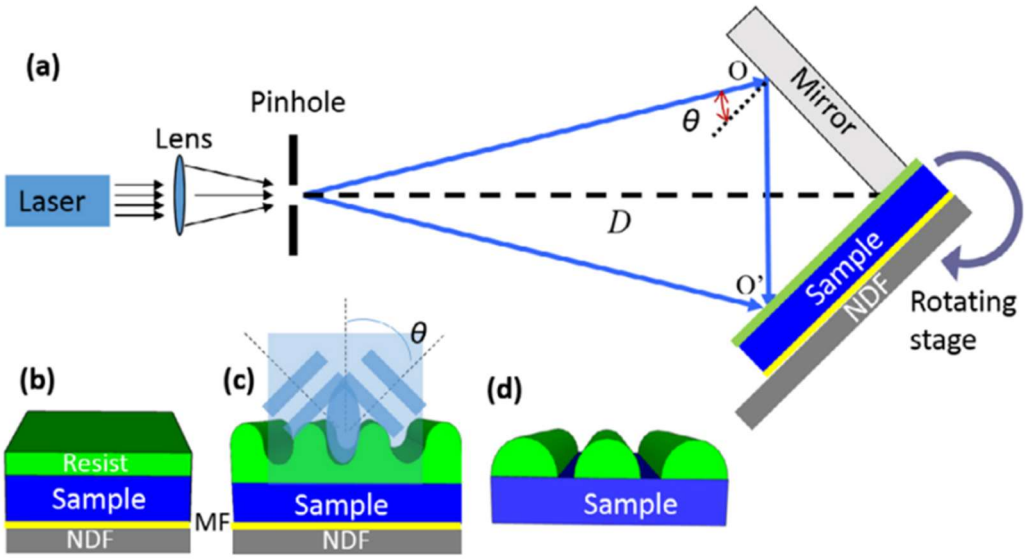

Figure 3.3: Sketch of LIL setup used for large area nanopatterning of polymeric thin films (thin green slab) spin coated on the sample (glass or polymer). (b)–(d) are the consecutive steps to be taken to complete the patterning process: firstly, a thin photoresist film is spun on the substrate coupled to a neutral density filter through matching fluid (b), afterwards interference fringes are recorded into the resist layer (c) and thanks to wet development of the resist layer a final rippled morphology is obtained (d).

Au nanostripe arrays were fabricated on top of large area (cm^2 scale) low-cost glass slides with this setup, as schematically shown in Figure 3.4. In particular, a soda lime glass substrate was first cleaned with a series of ultrasonic baths of acetone and isopropyl alcohol (Fig.3.4a). A positive tone photoresist film (AZ 701 MIR) diluted in the AZ-EBR solvent (ratio 2:1) was then spin coated on top of the substrate at a speed of about 2 krpm for a time interval of 60 s (Fig.3.4b), followed by a soft baking at 100 °C prolonged for 300 s. The so-formed thin polymeric layer was then exposed to the ultraviolet (UV) radiation by using a Lloyd's mirror interference setup aligned to a diode-laser source (wavelength (λ) of 406 nm coupled to a spatial filter. Exposure of the photoresist takes place with an impinging energy density rate of 0.77 mJ × cm^{-2} s^{-1} prolonged for 20 s (i.e., total dose incident on the substrate of 15.4 mJ cm^{-2}), followed by a post baking of the sample (100 °C) and resist development (AZ 726 MIF developer for 5 s) (Fig.3.4c). After blowing the sample with a dry nitrogen flux to dry the surface, AFM microscopy reveals the formation of periodic interference fringes which are homogeneously distributed on the sample over a large cm^2 area (Fig.3.4d).

In order to avoid the formation of a vertical standing wave pattern in the resist layer, because of interference between incident and reflected light from the substrate, we developed an optimized LIL nanofabrication exploiting (i) the photoresist layer thickness reduced below λ/2 (~180 nm) and (ii) a neutral density filter (NDF in Fig.3.4c; optical density = 4), capable of absorbing the incident light while coupled to the back interface of the substrate by means of a matching fluid (Cargille, OHGL nD).

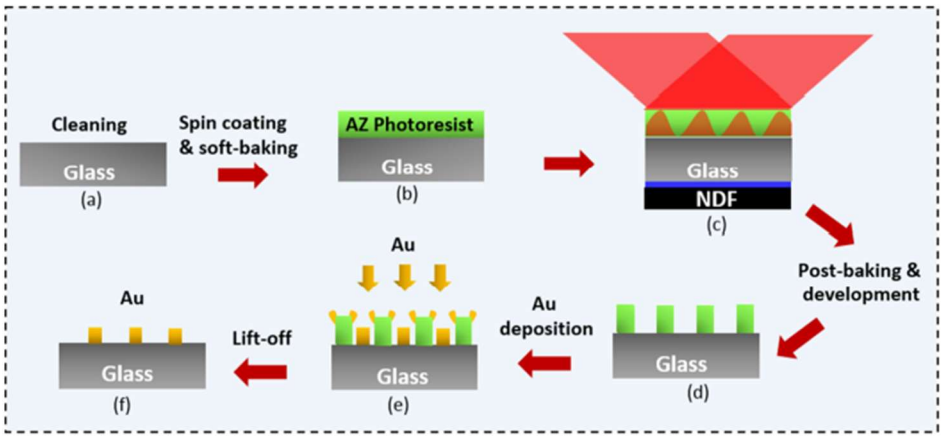

Figure 3.4: schematic process for LIL-based fabrication of gold nanostripe arrays. (a) cleaning of the surface in solvents; (b) spin coating of the photoresist polymer film; (c) exposure of the film to the light interference fringes generated with the application of an orthogonal mirror; (d) development of the exposed areas in a specific solvent; (e) evaporation of gold in the UHV chamber; (f) gold nanostripes resulting after the polymer mask lift-off.

3.3 Electron Beam Lithography (EBL)

Electron beam lithography (EBL) is currently considered the gold standard among the different nanofabrication methods, as described in chapter 2. Recently, shortly before the

beginning of my PhD thesis, the laboratory which hosted me upgraded an existing scanning Electron Microscope (Hitachi SU3500) by adding an EBL nanolithography module, consisting of a so-called pattern generator (Elphy Quantum from Raith®) and a beam blanker (Deben PCD beam blanker). The nanolithography software allows to design the pattern to be exposed on the resist layer, defining the electron dose delivered to each pixel, and controlling the fast-actuating electromagnetic beam-blanker needed for blanking off the beam.

The addition of the new instrument to the fabrication facilities of the research group required a considerable investment in manpower for the development of new recipes and methods in the design of complex geometries. I therefore had the chance and responsibility of developing such new EBL nanolithography processes on the free-standing Si_3N_4 membranes which are the subject of my research work.

Just before the beginning of my activity, the EBL setup and the nanofabrication process have been preliminarily tested on reference silicon substrates, obtaining some test results aiming at assessing the functionality of the instrument (at that time features with a lateral resolution below 200 nm were obtained), but the technique had not yet been implemented at its resolution limits. The possibility to perform the EBL nanofabrication process on the freestanding Si_3N_4 membranes, on one side, represents a challenge since the standard recipes developed for bulk silicon substrates had to be updated and modified; on the other side performing the EBL process on the ultrathin membranes guarantees a reduced electron background from backscattered and secondary electrons, potentially ensuring an increase in spatial resolution. The electron beam lithography for membrane patterning has been optimised for the PMMA resist employed in previous preliminary tests (E-Beam Resist AR-P 679 by AllResist®), spin coated at a speed of 4k rpm for 1 minute and then heated on a hot plate at 150°C for 3 minutes, with resulting thickness of 160 nm. Different geometries and conditions were explored to find the optimal recipe for the specific system and to optimize the spatial resolution. Figure 3.5a shows several geometries which are reproducibly obtained with the EBL technique, including dots, square features and lines of different lateral thickness.

As reported in figures 3.5b,c, the features which we have obtained on the free-standing membrane are characterised by a spatial resolution improved by about 20% with respect to previous silicon-based experiments, with minimum typical size of 170 nm. Improvement in size-control was indeed expected due to the reduction of electron back-scattering from the membrane: reduction of proximity effects that usually play an important role in defining the minimum lateral size permits the use of high energy beams (30kV) which are characterised by a sharper resolution. Further optimization of the EBL process is expected to deliver an even higher resolution, at levels which are not essential for the goals of my thesis.

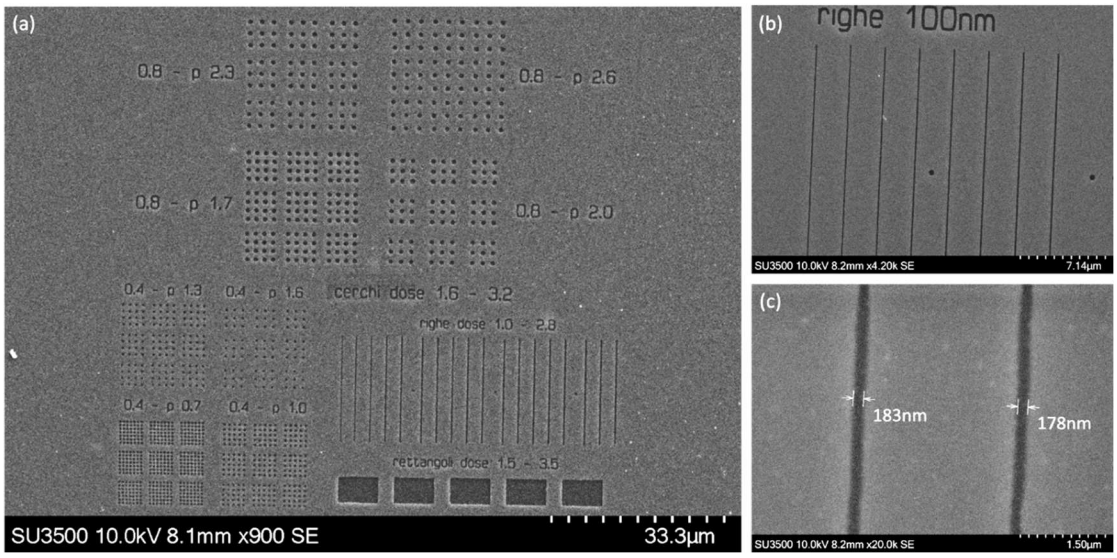

Figure 3.5: SEM images of geometries reproduced on the free-standing membrane via electron beam lithography. (a) circles, dots, squares and lines fabricated with high energy electron beam (acceleration voltage 30kV); (b, c) high resolution features demonstrate minimum lateral width of 170 nm.

3.3.1 Development of a fabrication process for perforated membranes

After optimization of the patterning by EBL of a holey mask on a PMMA film (supported by the Si_3N_4 membrane), one must proceed to a further nanofabrication step in order to perforate the membranes. The erosion of the membrane, necessary for the fabrication of nano-hole arrays, is performed via Reactive Ion Etching (RIE) using a chemical active gas (SF_6) which interacts strongly with silicon nitride (circa 140 nm/min of erosion rate at 300W) and weakly with metals (negligible erosion for evaporated gold).

Erosion of holes in the ultra-thin membrane can be then performed fabricating a protective metallic hard mask to shield the membrane during the etching process, with an approach similar to the one presented as a solution for charging issues in chapter 2 (back-etch mask). With this aim, a thin gold film has been deposited on the membrane via physical vapour deposition at normal angle (40 nm of gold on titanium layer to promote adhesion). PMMA resist has been spin coated above the metal, using the same recipe adopted on the bare membrane, and then exposed to the electron beam lithography with no evident loss in resolution related to the presence of the thin metallic layer. Proximity effects arising from the scattering of electrons in the metallic film are most likely negligible in the geometry conditions of the experiment, where a 10 nm error in the diameter of holes (ranging from 400nm to 700nm) wouldn't be noted.

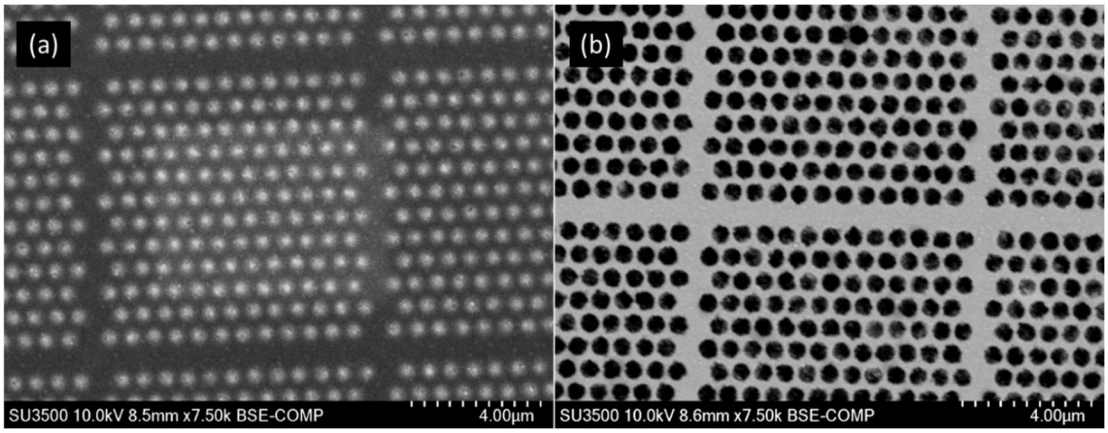

Figure 3.6: SEM images of the pattern before and after wet etching of the gold film above the membrane. (a) bright signal of the gold film emerges from the patterned polymer resist; (b) without polymer, bright signal of the patterned gold film is in contrast with the low-signal free-standing membrane.

After development of the impressed polymer, with specific developer (Developer X AR 600-55/1 by AllResist®) and applying propanol as a stopper (40 seconds developing + 15 seconds stopping), chemical wet etching has been performed through the EBL geometrical features transferring the geometry to the gold film (Figure 3.6a,b). For that purpose, a commercial solution of iodine and potassium iodide (7% / 5% in water) has been applied to the sample, diluted in proportion 2:1 with de-ionized water, chemically removing the exposed metal in about 3 to 5 seconds before being washed away in the propanol bath. With such a high erosion rate, the time-control is critical, and the precision of the etched area is challenging to calibrate: comparing the two panels of figure 3.6, it can be easily seen how the erosion process broadens the pattern, with the risk of connection between holes. A further optimization has been achieved applying the same recipe in a cold bath (iodine solution kept at 4°C with ice surrounding the vessel) decreasing the erosion rate and enabling experiments lasting about 10 seconds, drastically improving the control as demonstrated by Fig.3.7.

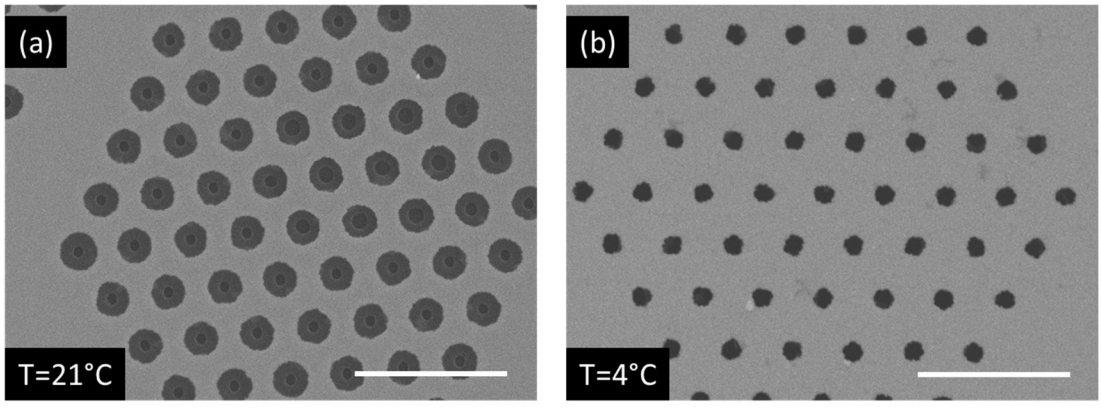

Figure 3.7: Cold wet-etch process of gold and related erosion control improvement. (a) SEM image of a wet-etch step performed at 21°C, with the eroded area (dark large circles) extending below the patterned hole in the polymer (small inner circles); (b) wet-etch step performed at 4°C, without broadening of the holes geometry (scale bars 5 µm).

Reactive ion etching is then easily guided by the metal mask, completely eroding vertically the silicon nitride thin membrane in about two minutes and leaving the mask thickness unchanged. The applied recipe is based on a single step of erosion performed at low power, 2:15 min at 50W (ICP) with a gas mixture of SF6 (70 sccm) and O2 (20 sccm). In figure 3.8a,b is reported the result of such a process applied to a test pattern where periodically spaced holes of diameter below 800 nm have been reproduced in a 100 nm-thick membrane every 2,5 µm. The recipe applied to this sample can be modified in terms of size and spacing of the holes inside the array, simply changing the geometry of the EBL pattern impressed in the resist layer, granting the capability to fabricate different designs and tune in that way the conduction properties of the membrane.

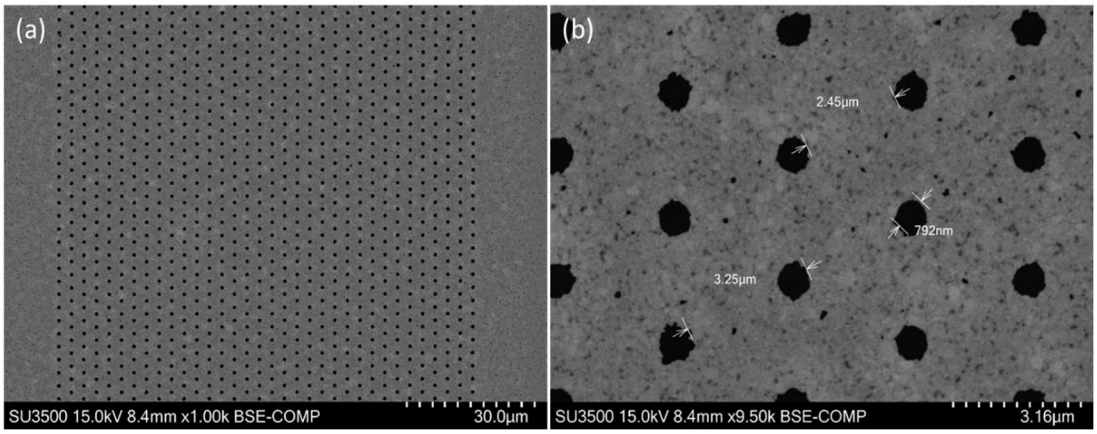

Figure 3.8: SEM images of nano-holes fabricated in the free-standing membrane via RIE. (a) periodic, ordered array of nano-holes in the membrane, high contrast is granted by the gold film still present on the membrane; (b) high-resolution image of the nano-holes, obtained diameter around 800 nm. Smaller low-signal dots are related to granular features of the gold film.

Chapter 4 – Nanofabricated free-standing membranes as concentrators of airborne particulate matter

As explained at the end of chapter 1, one of the advantages of adopting TEM membranes as substrates for nanometric-particle analysis is the membrane's high transparency to electrons, which enables high resolution lithography and low-background electronic spectroscopies. To better understand the potential application of this feature, here I describe the fabrication of free-standing perforated membranes optimised for concentrating and capturing nanoscale particulate matter in air suspension. In the first part of the chapter, I quantitatively assess the limits of detection of elemental EDX applied to submicrometric scale test nanostructures, fabricated by electron beam lithography on the membrane chip, demonstrating the advantages of choosing free-standing membranes as substrates for particle collection. In the second part of the chapter, a prototype setup for the collection of airborne particles is presented. In the last two parts of the chapter, generation and collection of micro- and nano-particulate is discussed.

4.1 Optimized perforated membranes

Nanodisc arrays of gold, with controlled sub-micrometric diameter, have been fabricated by EBL on top of 200 nm and 30 nm thick free-standing Si_3N_4 membranes, and on reference Si_3N_4 membranes supported on a Si frame, in order to study the EDX detection limits and signal-to-noise (S/N) level compared to bulk substrates, and also the effect of membrane thickness on the quality of the signal. The nanofabrication has been performed via Electron Beam Lithography on a single layer PMMA resist film, applied as a mask on the Si_3N_4 membrane. Following electron irradiation and development of the pattern, as described in more detail in Chapter 3, gold deposition is obtained via PVD and then removed in acetone. As shown in Figure 4.1, one corner of the free-standing window is selected as geometrical reference and multiple nanodisc arrays are written both on the membrane and on the silicon frame to statistically ensure the presence of at least one disc for every diameter of the sequence. In the selected design, nanodisc diameter varies from 200 nm to 2 µm but the interest of the observation is mainly dedicated to nanoparticles of typical size in the range 200 – 600 nm, roughly corresponding to the size of sub-micrometric particles that will be the object of the following study.

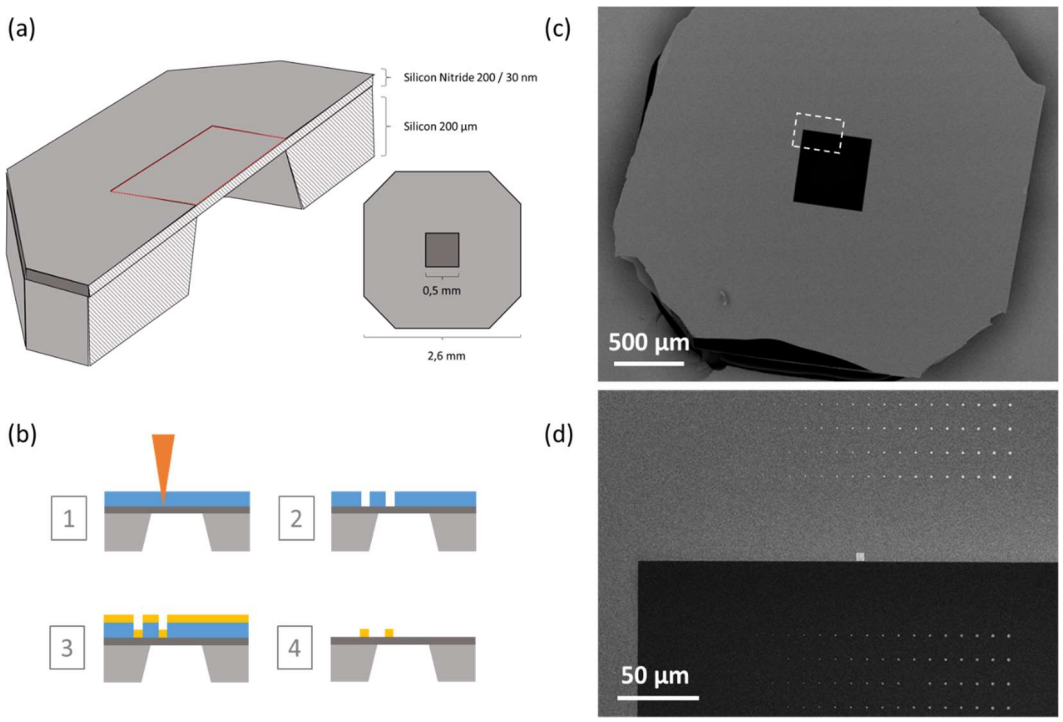

Figure 4.1: Fabrication of gold structures on a TEM membrane chip. (a) sketch of the chip geometry, in cross-section and top view; (b) EBL fabrication process, including pattern writing (1), resist development (2), gold layer PVD through the polymeric mask (3) and lift-off (4); (c) low magnification SEM image of the chip and (d) detail of the gold structures fabricated both on free-standing window (black area, bottom) and silicon frame (grey area, top).

The application perspective, as explained previously, regards the investigation of airborne particles and the idea of co-localization of different techniques to identify particle components and determine their nature. With this goal in mind, we study the advantages of working with free-standing membranes in terms of improved resolution and signal of spectral mapping measurements, adopting sub-micrometric particles as reference targets. Taking advantage of the Energy Dispersive X-Ray Spectroscopy module (EDX Thermo Fisher Scientific, NORAN SYSTEM 7) integrated with the laboratory's electron microscope, we can directly acquire the spectral response of the fabricated structures to the illumination with a high current electron beam.

For each measure the beam is scanned across a single object, acquiring the signal arising from a fixed square area, thus simulating the acquisition of a spectral map with a single particle in the field of view. The results of this observation are shown in Figure 4.2, which demonstrates the capability to detect a substantial amount of information. In the first panel (Fig.4.2a) two SEM reference images display the EDX acquisition from square areas, repeated in sequence over the sub-micrometric gold discs. The investigated structures are defined by scaling the nanodisc diameter from 600nm to 200 nm (from left to right) and are located both on the thick silicon frame (top, labelled as "frame") and free-standing membrane (bottom, labelled as "free"). This peculiar configuration allows at first glance a comparison

between the signal extracted illuminating a structure on the frame and one supported by the membrane (see Fig. 4.2b). The background signal observed on the frame, produced in the underlying material, is significantly higher (grey spectrum, hundreds of counts between 0,5 and 1,5 keV) and negatively affects the detection of low signal peaks as the one of aluminium (weak signal arising from the mounting support of the chip). In an opposite manner, in the case of the free-standing disc a very low background signal is detected (red spectrum, tens of counts between 0,5 and 1,5 keV) thanks to the complete absence of underlying material, thus strongly increasing the detection sensitivity to low intensity signal.

This effect is better defined through the observation of how the EDX signal scales with the diameter of the discs, reported in Figure 4.2c. In the graph, the absolute signal of the primary gold EDX peak (located at 2.4keV) is shown for different sample configurations: discs fabricated on a 200 nm-thick membrane corresponds to red square symbol, filled in the "frame" case and empty in the "free" case. Similarly, the structures fabricated on a 30 nm-thick membrane correspond to blue triangles and are divided in filled and empty symbols for the "frame" and "free" cases. As expected, the signal decreases for smaller objects approaching zero for 200 nm discs located on the silicon frame and increases for larger objects with higher signal detected in free-standing conditions thanks to the low background effect. The fact that the thicker membrane displays an overall slightly higher signal is motivated by the increased amount of scattering events happening in the material below the gold disc. Indeed, as discussed in more detail in the paragraph, passing through the membrane, electron trajectories are deflected by interaction with the substrate atoms and may be scattered back to the gold layer, increasing the number of photons generated in the metallic disc. As discussed in chapter 2 this phenomenon is playing a similar role also in the context of EBL resolution limits, which are defined by the implied material atomic number and by its thickness.

It is important to highlight that the method of EDX acquisition which has been chosen, integrated signal over selected micrometer scale areas larger than the nanodisc itself does not correspond to the maximum signal that can be extracted from the sample. The EDX spectrometer, in fact, can also be configured to focus the electron beam on a single pixel position for an extended span of time ("point and shoot" mode), acquiring all the photons emitted from a single illuminated spot. In this case a higher EDX signal is granted with respect to the measure of an integrated area because the electron beam is continuously stimulating the X Ray emission from the target atoms of the nanostructure. Our choice is based on the fact that, also neglecting the difficulties related to drift in sample position for stable investigation of sub-micrometric objects, to perform the "point and shoot" analysis one must know in advance the position of a specific particle of interest, which is not granted in the case of an experiment aiming at sampling of randomly deposited particulate matter. This means that the Limit of Detection (LoD) deduced by the scaling intensities of Fig.4.2c is substantially larger than the LoD derived from a point-and-shoot measurement. This statement can be easily demonstrated by comparing the signal obtained with the beam scanning a square area (as before) and the signal extracted illuminating a circular area

roughly corresponding to the area of the nanodisc, as can be seen in Figure 4.2d. A single 200 nm particle located on the free-standing membrane is there illuminated for the same time in the two modalities, first with a square scanning area of lateral size about 3µm (green curve) and then right on top of the object (blue curve). In this mode, the gold peak signal is drastically increased by more than an order of magnitude thanks to the continuous interaction of the beam with the Au structure. However, also the overall background signal is more than doubled due to the increased electron scattering and X-Ray generation from the high Z-number Au structures.

The spectroscopic EDX signal obtained with the square scanning spectral map corresponds in other terms to a good compromise between, on the one hand, high signal level from the nano object and low background level, and, on the other hand, reduced requirements for positioning accuracy and for drift control (compared to point and shoot spectroscopy). Thanks to the presence of the electron-transparent membrane in most of the illuminated surface, even the very low X-ray signal generated by a small nano object in the 100 nm range can be thus detected. In light of these considerations, I thus re-analyze the signal from the nanodiscs no more in terms of the absolute counts of the peaks, but as the ratio between the peak counts l and the baseline statistical noise (defined as the square-root of the baseline counts). The *Signal to Noise Ratio* (S/N) thus expresses in a straightforward way the detection capability of the system.

The symbols displayed in Fig.4.2e follow the same labelling adopted in the graph of Fig.4.2c, with different membrane thickness and different supporting conditions represented by colours and shape. Here, the thin-30nm-membrane displays the overall higher S/N values thanks to the extremely low background in comparison not just to the silicon frame measurements but also to the free-standing 200nm-thick membrane, especially at the smaller diameters. This last observation is the core message of the plot in Fig.4.2f, where the two free-standing membranes (200 and 30 nm) are compared focusing the attention on the S/N gain arising respect to the silicon frame condition, as a function of the scaling Au nanodisc diameter. The plot highlights in a clear way how critical the choice of a thin, free-standing membrane is when EDX analyses are done on small particles in the 100 nm range or below.

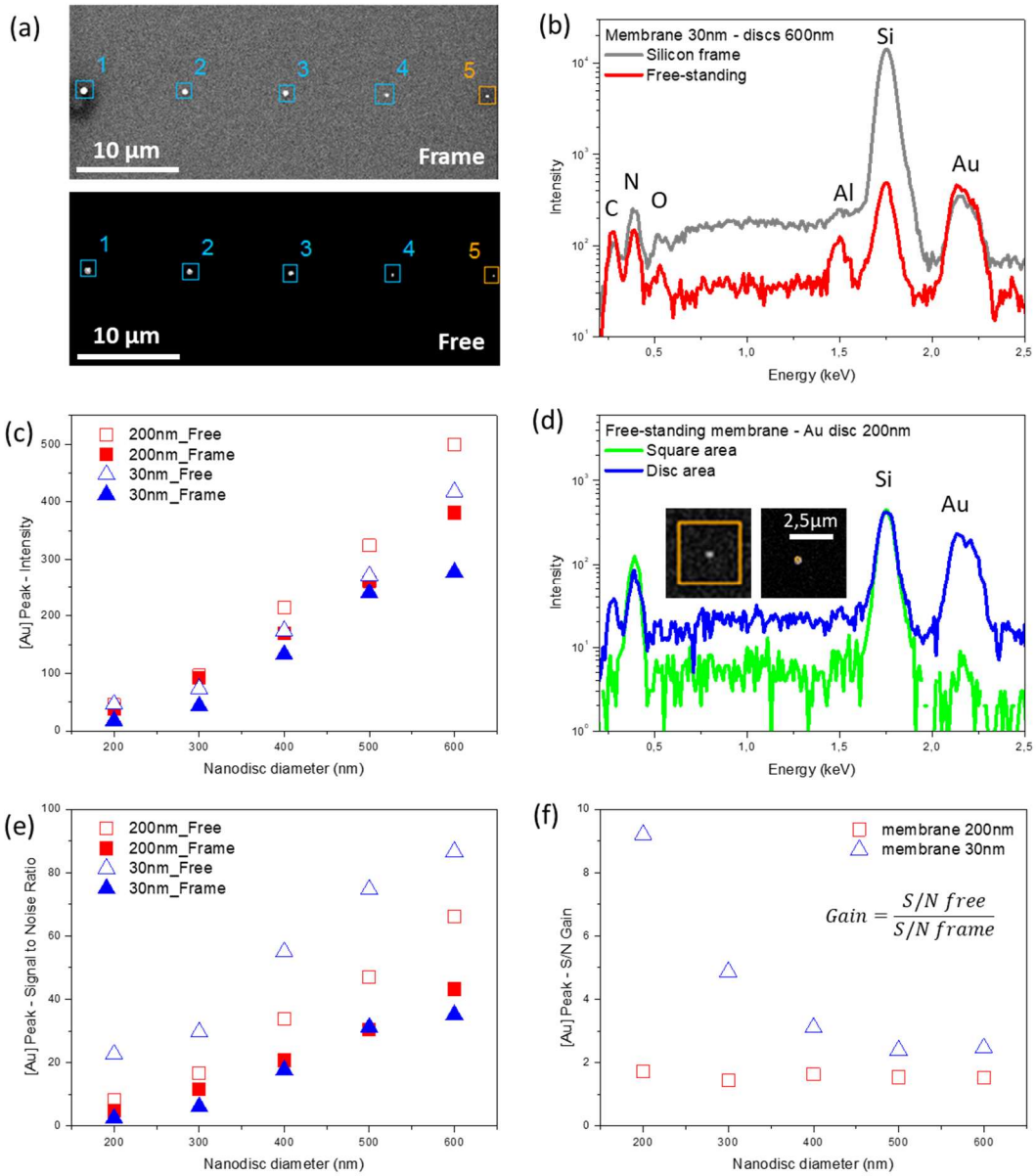

Figure 4.2: Influence of membrane geometry on EDX sensitivity. (a) Structures fabricated on silicon frame (top) and free-standing membrane (bottom), with disc diameter scaling 600-200nm from left to right; (b) comparison of EDX spectra of identical gold discs (d=600 nm) measured on silicon frame (grey) and free-standing membrane (red); (c) gold signal scaling with nanodisc diameter in different configurations, varying membrane thickness and position of the structures; (d) comparison of EDX spectra of the same structure acquired integrating a larger square area (green) and a circular area inside the disc (blue); (e) gold signal to noise ratio (S/N) of the measurements displayed in panel (c); (f) S/N gain, calculated as the S/N ratio of structures free-standing and those located on the frame.

The application of membrane chips in concentrated collection experiments, anyway, requires functionalization of the central free-standing window with arrays of pores to ensure the flux of airborne particles directly through the membrane. Such fabrication requirements

bring its own physical limits, related in first place to the mechanical stability necessary to withstand high pressures during air sampling. Referring to the commercial Si_3N_4 membranes available on the market, perforated free-standing membranes are only found with thickness of 200 nm or larger due to mechanical stability issues. Though in terms of X-ray background the optimal choice would be to fabricate a perforated 30 nm membrane, we opted for a compromise between mechanical stability and reduced fluorescence background and focus our attention on 100nm-thick membranes.

To understand the improvement in EDX signal obtained fabricating membranes with thickness 100 nm instead of 200 nm, we rely on quantum Monte Carlo (QMC) simulations (Casino software package) to investigate the interaction between electrons and a realistic sample during EDX analysis, in the hypothesis of Si_3N_4 membranes of increasing thickness 30 nm, 100 nm and 200 nm. The QMC package allows us to estimate the influence of membrane thickness on the electron-sample interaction and the consequent X-ray photon emission. In Fig.4.3a is reported a simulation of the electron trajectories in a multi-layered system approximately equivalent to the nanodisc array sample. Here the electrons interact with an 80 nm-thick flat film of gold (same thickness as the nanodiscs but simplified as an extended film) supported by 100 nm of silicon nitride and by a 10 μm thick silicon frame. Red lines represent the path of Back-Scattered Electrons (BSE), which undergo enough scattering deflections to emerge from the sample surface, while blue lines represent trajectories of electrons which dissipate all their energy in scattering events, generating energy relaxation phenomena as secondary electrons and the X-Ray photons detected in EDX. As evident in the lower part of panel 4.3a, a relevant number of collisions takes place in the silicon layer, which explains the higher fluorescence background observed for bulk samples and when the Si_3N_4 membrane is supported on the Si frame. For the same reason a strong suppression of background fluorescence is expected when working with free-standing samples, since no material is located below the silicon nitride membrane and therefore the number of scattering events is drastically reduced. Similar QMC simulations have been performed for all membrane thicknesses and the results are summarised in Fig.4.3b: a schematic report of the EDX intensities calculated for gold, silicon and nitrogen displays how the signal arising from the three elements is affected by the thickness of the membrane (horizontal axis) in *frame* and *free* configuration (filled or empty symbols). The simulated data confirm a significant decrease of signal generated in silicon and nitrogen for 100 nm-thick membranes in the free-standing configuration, while the signal of gold remains stable meaning that the S/N detection capability of the system is already improved decreasing the silicon nitride thickness from 200 nm to 100 nm.

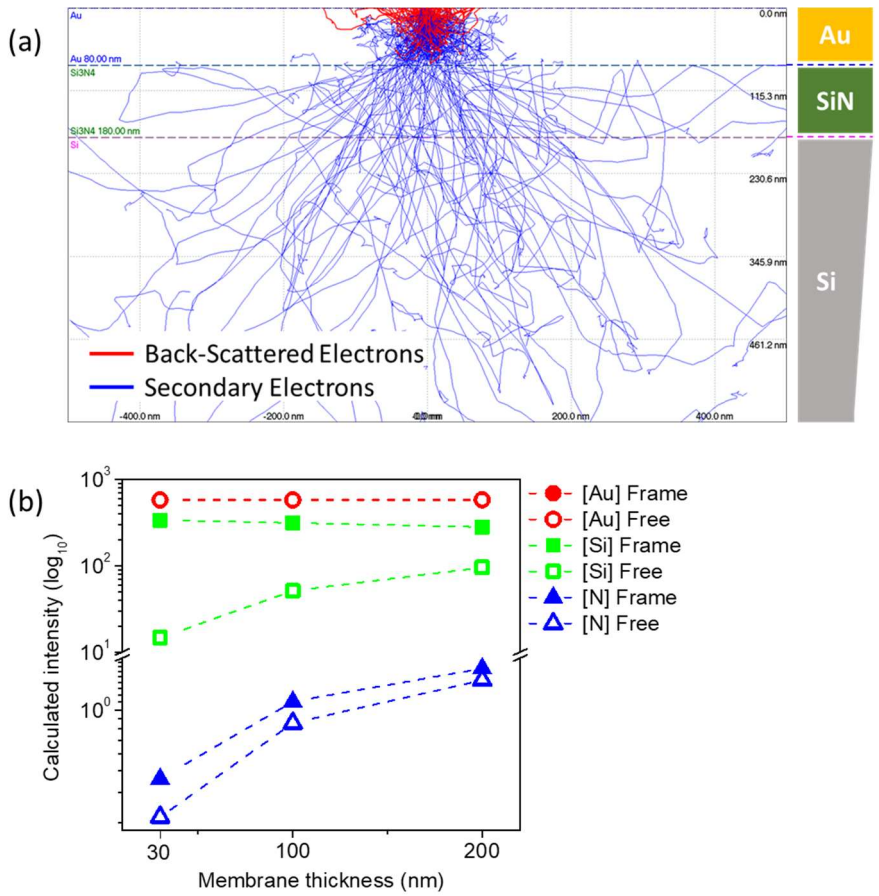

Figure 4.3: Simulated interaction (Casino simulation[128]) of the electron beam with samples of different thickness. (a) Calculated trajectories of the electrons (backscattered in red, secondary in blue) in the case of a 80nm gold film (yellow) supported by 100nm silicon nitride membrane (green) and a 10µm silicon frame (grey); (b) calculated EDX intensity of samples where the membrane simulated thickness is varied. Gold (red), silicon (green) and nitrogen (blue) signals are calculated on the frame (filled symbols) and on the free-standing membrane (empty symbols). Frame/free symbols of gold are overlapped at this scale.

This information supports further our decision to adopt a sample thickness of 100 nm, looking for a compromise between mechanical stability and detection sensitivity. The geometry of pores, anyway, plays an equally important role in determining the performance of samples for environmental sampling application. In the development of the fabrication process, we initially designed dense arrays of pores with square lattice symmetry, incurring in systematic mechanical failure of the free-standing window after the application of relatively low stress, as the manipulation of the frame with a tweezer or the pressure drop occurring during fabrication steps in vacuum chambers. In Figure 4.4a, I show an example of this casualty: the SEM image refers to a membrane broken during the dry etch transfer of the pattern to the free-standing window. The irregular surface morphology of the supporting glass, visible below the free-standing area, is a channel produced to avoid trapping air below the membrane chip. Looking at the detail images in Fig.4.4b and Fig.4.4c, one can clearly understand that the failure of the free-standing membrane has been promoted by the

presence of the square symmetry of pores, which causes concentration of the stress in the lattice as a linear distribution of point defects and guides the membrane rifting across the holes (see for example the pattern border in Fig.4.4c). During my work, I thus tested an optimised pore geometry consisting in a honeycomb array which alternates perforated regions and intact areas which allow to redistribute mechanical stress. As can be seen in Figure 4.4d, for this kind of perforated membrane we intentionally applied stress up to the breaking point by pressing a tweezer on the frame (and eventually breaking the frame itself). As can be seen in the detail of Fig.4.4e, the rift line runs across the free-standing membrane without developing a preferential path aligned along the fabricated holes. The same conclusions can be derived considering the image of Fig.4.4f, taken from another sample where the mechanical failure has been induced by applying a high pressure-drop in the 1 Bar range across the membrane. Also in this case, the tearing line follows a path external to the pores, ensuring that under the typical environmental sampling conditions (pressure drops below 100 mbar) the 100 nm-thick membrane has the required mechanical stability.

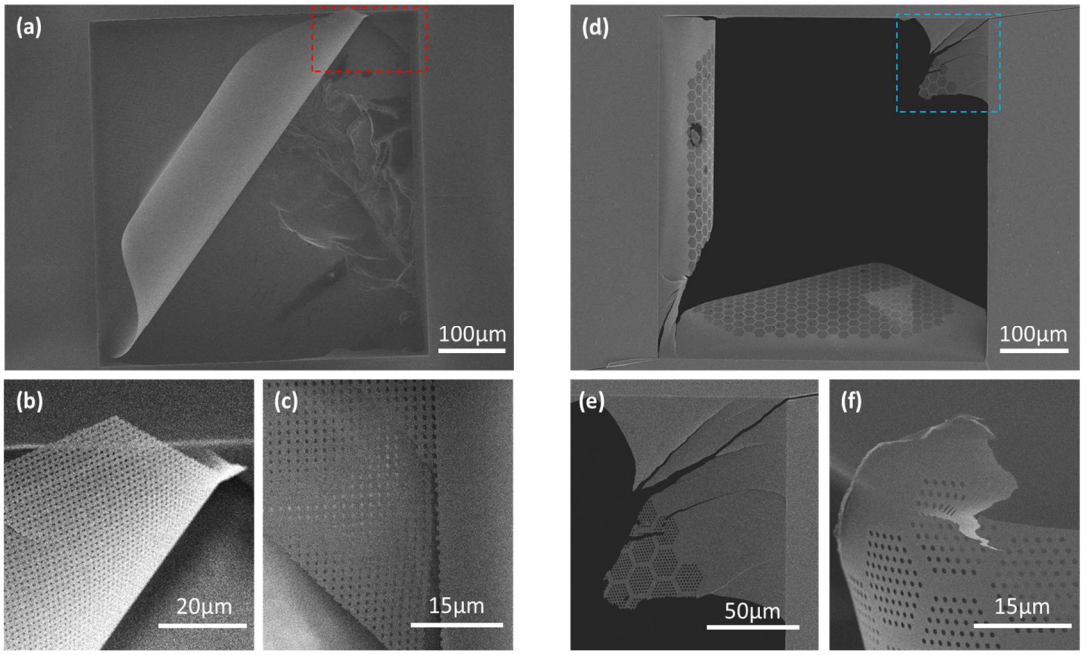

Figure 4.4: Comparison of failure events in the case of different hole-array geometry nanofabricated 100 nm thick Si_3N_4 membranes. (a) SEM image of a failed membrane with square distribution of holes and details (b, c) of the broken membrane, where the rift line propagates among the pores; (d) SEM image of a test chip with hexagonal optimized distribution of holes, cracked by stressing the frame. Details (e, f) of the rift line no longer propagating among the holes.

The challenge of fabricating in-house our own nanofunctionalized membranes for air sampling and co-localised particle analysis arises as a specific response, complementary to the conventional solutions available in the market. For this reason, our system properties were set up referring to commonly used materials like Polycarbonate Track-Etched (PCTE) filters (Cyclopore™ Track Etched Membrane, 0.4µm Polycarbonate (hydrophilic), 47mm diameter by Whatman®, Cat. No. 7060-4704), widely used in the field of environmental

physics[67,129], highly efficient for collection of sub-micrometric particles[68,130] and compatible with SEM imaging assessment[131]. In particular, they are characterized by a nominal pore diameter of 0.4µm (±20%), a thickness of 10µm and a total filter diameter of 47mm. The pores are randomly distributed on the surface and in many cases partially overlapped resulting in elongated apertures in the filter (see Fig.4.5a), with an estimated open area filling factor of 15%. The pores density and filling factor is up to 30 % higher in the case of perforate Si_3N_4 TEM membranes available on the market, as the 200nm-thick membrane shown in Fig.4.5b. In the latter case, the close hexagonal packing of 0.4 µm holes has the aim of supporting samples for TEM analysis with maximised transparency. In the fabrication of our functionalized membranes, therefore, we seek a compromise between the geometry defined in the previous section of the chapter and the emulation of PCTE filters properties. Keeping in mind that the thickness of our free-standing membrane is two orders of magnitude lower with respect to the PCTE filter, we design the fabricated holes to minimize the flow impedance without significant losses in mechanical stability, with a resulting open area ratio of about 10%. The optimized pores geometry is reported in Fig.4.5c, with pore diameter of 600 nm (panel A) that can be reduced to about 400 nm (panel B) modifying one processing step at the price of lower quality in shape and homogeneity of pores.

The nano-functionalization of membranes is achieved with a multi-step lithography process (details in methods, scheme in Fig.4.5d) involving EBL pattern writing with a PMMA film spin-coated over a thin gold layer (1), followed by resist development (2), wet-etch transfer to the metallic film (3), resist film removal in acetone (4) and dry-etch transfer to the free-standing membrane using RIE technology (5). At the end of the nanofabrication process, the functional area covers about the 70% of the free-standing window, extending over a 400x400µm area (Fig.4.5e) and the pore size distribution matching a range of diameters compatible with the pores of PCTE and 200nm membranes. The honeycomb structure additionally ensures the required mechanical stability.

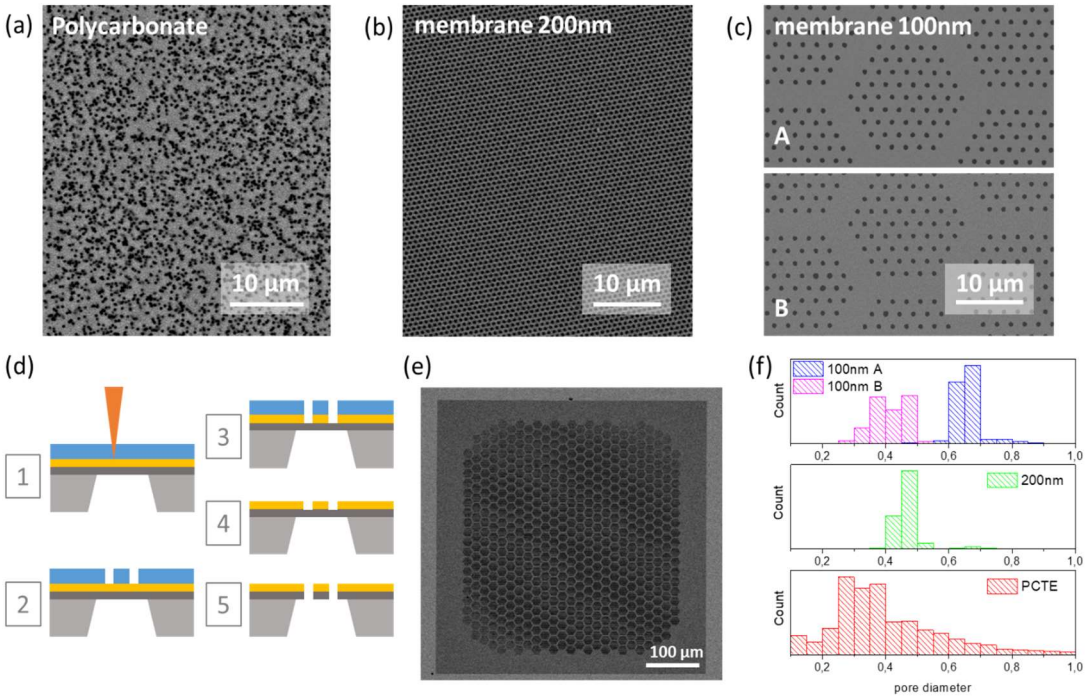

Figure 4.5: Fabrication of optimized porous membranes. (a) Reference PCTE filter with random distribution of pores; (b) 200nm-thick membrane with high density pores; (c) 100nm-thick membranes fabricated with optimized geometry and different pore diameter (A=650nm ±50 nm, B=425 nm ±75 nm); (d) fabrication process, including pattern writing in back-etch configuration (1), resist development (2), wet etch transfer to the metallic film (3), resist lift-off (4) and dry etch transfer to the free-standing substrate (5); (e) SEM image of a fabricated free-standing window; (f) size distribution statistics, extracted from SEM images of 100nm thick (blue, magenta), 200nm thick (green) and PCTE (red) pores.

4.2 Collection unit prototype

To demonstrate the detection improvement in our optimized collection samples, the first challenging task is the realization of a sampling system. The application of free-standing membranes into a real situation of particle sampling requires the integration of these micrometric systems into a bigger, dirty (in terms of particles) and sometimes unpredictable context. To do so, we designed a custom holder on which to mount the membrane chip with a clean thermal wax (TEDPella® *Quickstick135*). The coin-size, perforated support, allows to integrate the delicate free-standing membrane into a complex flux line avoiding the risky manipulation of the frame. After sampling the same coin-size support is also used for moving the membrane into the spectroscopic instruments or in the vacuum chambers.

In the panels of Figure 4.5 are presented the two objects that enable the integration of membrane chips into flux-lines: the coin-size “chip holder” and its scaffold, defined as “chip housing”.

The chip holder (Fig.4.5a, Fig.4.5b) is a perforated aluminium disc with a central, circular depressed slot where a membrane chip can be fitted. The use of a thermal mounting wax

ensures the complete adhesion of the chip frame to the chip holder thus avoiding any possible flow loss. On both sides of the disc, the thickness is reduced with a step that maintains the chip holder in position when clamped into the chip housing, avoiding displacement also if held upside-down or in case of accidental clashes with keys or other parts. When performing a collection experiment, several chip holders can be prepared in advance with the membrane chip mounted in place and then easily inserted one after the other in the chip housing to perform a set of measures.

The chip housing unit is essentially a connection of the external flux line with the porous membrane (see Fig.4.5c, Fig.4.5d). Attached to external parts with universal connectors (Swagelok® 1/6”), the housing is composed by a lower supporting half and an upper closing, held by a set of screws and airtight thanks to a double O-ring system which ensures the passage of air only through the membrane pores. The chip holder is blocked in a circular lowering of the supporting part (see Fig.4.5e) and pressed vertically on the lateral steps by the bare surface of the closing part, pressing at the same time the inner O-ring below the chip holder together with the outer O-ring surrounding it.

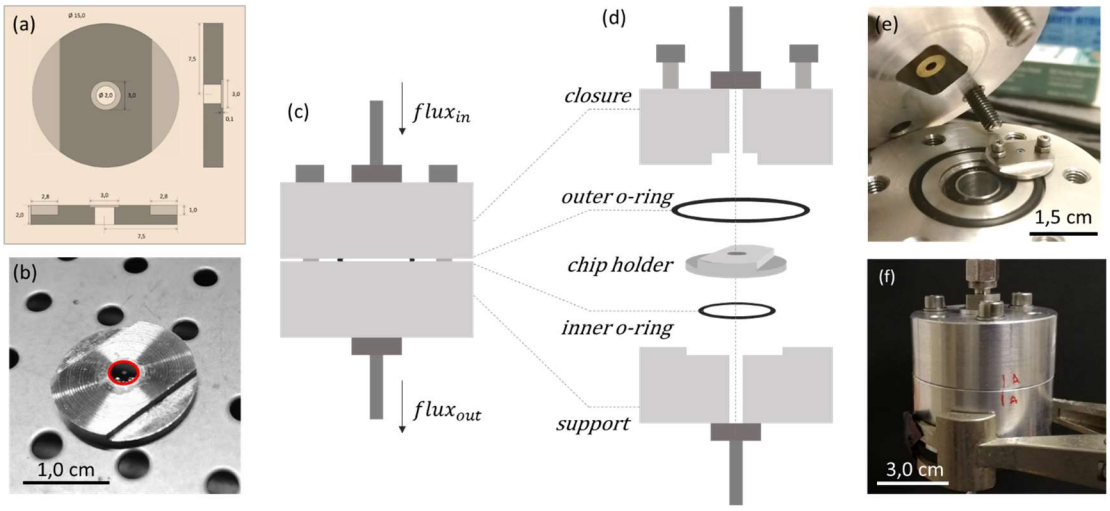

Figure 4.5: In-house built unit for insertion of the fabricated membranes in a flux line. (a, b) project drawing and picture of the removable coin-size *chip holder* unit, with the membrane chip (highlighted in red) mounted and aligned with the central hole; (c, d) schematic representation of the *chip housing* system, depicted as closed (c) and open (d); pictures of (e) an old prototype chip holder inserted in the docking position and (f) the closed chip housing system, ready for connection to a flux line.

With the chip housing available, the nanofabricated porous membranes can be inserted in a flux line and tested in view of their application. To obtain the same reference sampling conditions of the Cyclopore polymeric filters, we designed our flux line scaling the parameters to fit our nanofabricated filters. In conventional sampling conditions, PCTE filters with 47 mm diameter are employed with air fluxes of 16,6 l/min, requiring massive pumping systems and macroscopic lines. The use of nanostructured membranes for air filtration with remarkably lower active area on which the particles are concentrated, results however in a scaled equivalent flux of 5ml/min. For this range of small fluxes, it is possible to employ

miniaturized membrane pumps, notably reducing the system cost and dimension. In Figure 4.6 are presented two prototype configurations used to perform the experiments of the thesis, suitable to deliver fluxes in the range between 1-6 ml/min to the chip housing system. The first prototype (Fig.4.6a) is a reasonably compact system composed of a membrane pump, a software-operated mass-flow-controller (MFC, by Brooks® SLA5800 Series) connected to a laptop and a pressure-meter (GE Druck DPI 705-IS Pressure Indicator) attached to the back of the chip housing to monitor the pressure drop applied to the free-standing membrane. The second prototype (Fig.4.6b) is essentially the miniaturized version, equivalent to the first one, where the pump unit is substituted with a miniaturised membrane pump (Fig.4.6c, Xavitech V100-5V) and instead of the digitally controlled MFC a mechanical flowmeter (Rotameter Pr. No. 23324 by Supelco®) is installed, reducing the whole line to a portable system that can be fitted in a suitcase. As shown in the scheme of Fig.4.6d, anyway, the elements composing the setup are basically the same, and provide all the requirements for the full operation of experiments. In these conditions, the response of the different membranes to fluxing can be tested connecting the chip housing to the end of the flux-line. As reported in Fig.4.6e, a set of samples has been mounted in the line, including a 200nm-thick membrane, two different 100nm-thick membranes and a cropped portion of a commercial PCTE filter mounted over a silicon frame chip. The resulting pressure drops, measured for increasing fluxes, give information about the flow impedance of the different porous systems. Under this point of view, the experimental observation is in complete agreement with the expectations, since the two fabricated 100 nm membranes cover the whole range of impedances. The chip fabricate with a lower hole filling factor leads to a higher flow impedance: this is the case of 100 nm membranes with 400 nm pores (case of 100 nm B, magenta line), with larger pressure drops respect to the ones measured for PCTE (red line) and 200nm-thick membranes (green line) at equivalent fluxes. At the same time, chips fabricated with a higher hole filling factor on 100nm thick membranes (600 nm diameter pores - blue symbols 100nm B) demonstrate lower impedance to flux, right below the values of the 200nm membranes which display a significantly higher open-area ratio.

As a general observation, these flux-testing experiments demonstrated not only the possibility to mount our free-standing membranes inside complex fluxing systems, but also their applicability in sampling conditions where different sources of stress (pressure drops, particle collisions, variations of temperature) could have compromised the chip integrity.

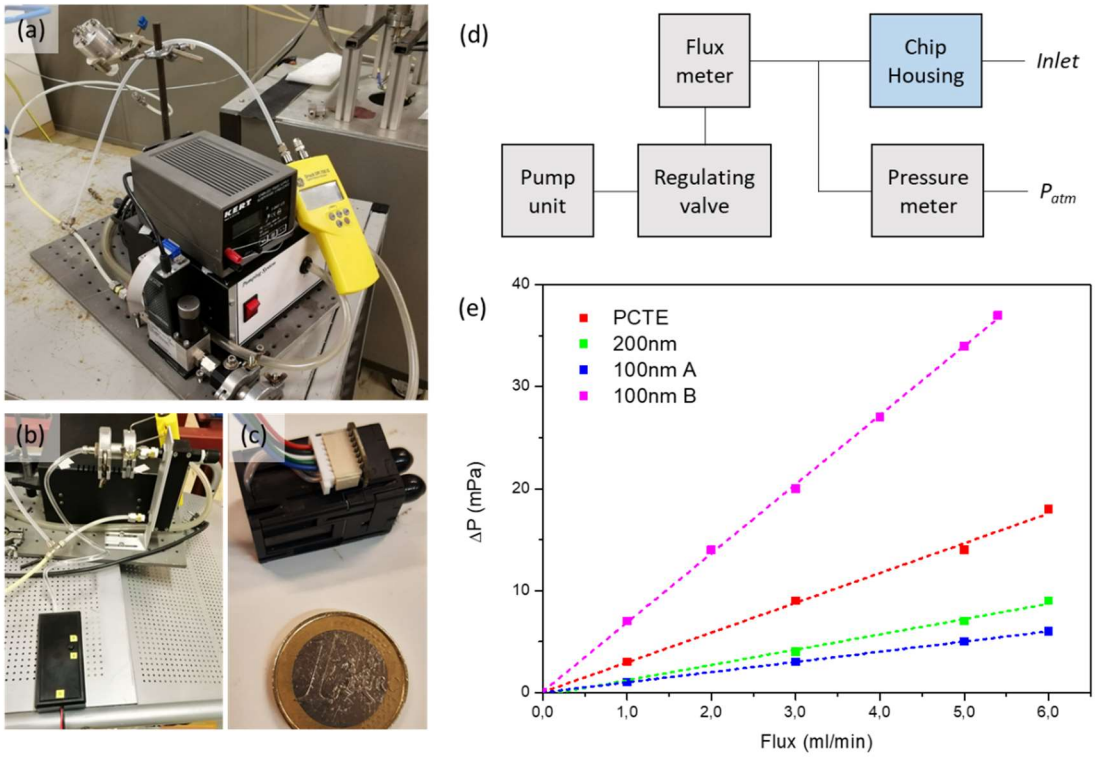

Figure 4.6: In-house built, portable flux-line, reported in (a) with its initial components and in (b) with portable pump and flux control units; (c) detail of the miniaturized pump, with a coin for reference; (d) Scheme of the line modules, with pumping unit, pressure drop regulation and control systems for flux and pressure; (e) measured flux (x-axis) as response to increasing pressure drop (y-axis) with different porous systems, where slope corresponds to the observed impedance. 100nm-thick membranes, with 600 nm pores (blue line) and 400nm pores (magenta line), cover the whole range of impedances including the values of both 200nm-thick membranes (green line) and PCTE filters (red line).

4.3 Generation of Airborne Micro- and Nano-particles

Straightforward observations and testing of the membrane collection capability can be performed by sampling, with the custom developed setup, a calibrated suspension of nanoparticles. To enable high-contrast images in SEM, to avoid overlapping of peaks in EDX spectroscopy, and to ensure the repeated use and regeneration of the membranes, we select pure, chemistry-grade sodium chloride (NaCl) nanoparticles as test analyte. After sample collection, once the chip holder is transferred in the SEM microscope, in order to extract statistical information about the particles' abundance and size distribution I acquire a set of six SEM images with predefined field of view (96x128 µm) and resolution (5120x3840 pixels) from the active area of each membrane, recording an overall surface area (290x260 µm) which covers almost completely the free-standing membrane portion. Given the large number of particles collected under the typical sampling conditions employed (in the range of 10^4) I employed a digital image processing program (ImageJ) to analyse the full set of images, so defining the statistical distribution of the geometrical parameters which represent the nano objects. The nanoparticle population is then represented in compact form as

histograms of particulate size distribution. During my thesis I developed and used three different setups for generating nanoparticles in air suspension.

In a first proof-of-concept system, defined as *dust generator*, solid grains of NaCl are milled to decrease the average size of crystals and the resulting powder is inserted in a small chemistry-lab flask which acts as a suspension chamber during the sampling experiment. Inside the flask a magnetic stirrer rotates in proximity to the bottom, keeping a fraction of powder constantly in suspension. As depicted in Fig.4.7a, the particle generation system is physically connected via a bent, long ⅛" stainless steel tube to the chip housing which holds the membrane, mounted in its core. The flask is sealed with a rubber plug and made airtight, with dry air entering through a syringe filled with silica gel. The air suspension is extracted from the flask using a thin-walled stainless steel tube with 2.1 mm inner bore diameter (see Fig.4.7b). The fraction of particles which survive flight in the small size tube are finally trapped and concentrated on the microfabricated Si_3N_4 membrane. The resulting collection is then analysed by SEM images of the porous area as the one of Fig.4.7c, where irregularly shaped agglomerates of particles are clearly visible and can be easily measured by the ImageJ processing tool. Since the nanoparticles are produced by mechanical milling their shape is always irregular and equilibrium shape cubic crystals are never observed.

The size distribution of the collected suspension presented in Fig.4.7d, summarised as counted particles per ranges of equivalent diameter, is the result of a 5 min collection test performed sampling through the membrane with a flux of 5ml/min, equivalent to standard fluxes used on 47mm filters scaled to the miniaturized active area size. The statistical data reveal a great number of particles in the 0,1-1,0 µm range, but also a relevant quantity of objects above one micrometer. The histogram shape can be associated with the distribution of airborne dust, with a predominant fraction of volatile, small particles and a decreasing tail of counts related to bigger particles, gradually increasing in weight. At the lower limit, below 200 nm, the bin counts are drastically suppressed, due to agglomeration of smaller particles combined with the limit of detection in the analysis procedure of ImageJ where particle counts are triggered above a defined pixel's threshold. At the upper limit, the number of particles is gradually decreased as expected from hydrodynamic considerations since the narrow, bent tube cuts down bigger particles due to collisions with the inner walls. The distribution of collected particles is, therefore, the result of a cutting action of the connecting tube on the powder suspension generated inside the glass flask, where a random distribution of agglomerates and smaller objects is kept in motion by the magnetic agitator.

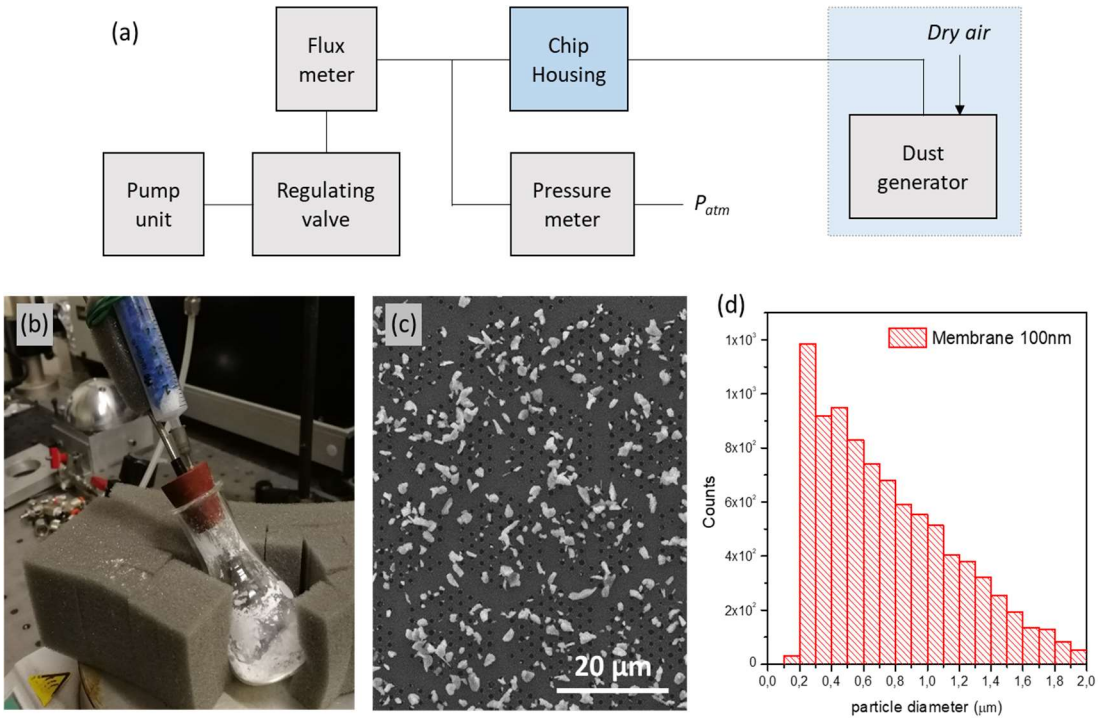

Figure 4.7: In-house designed, suspended particle generation system from solid powder (*Dust generator*). (a) Scheme of the overall configuration, with the chip housing unit of the portable flux-line attached to the dust generator; (b) picture of the chemistry-lab flask where a magnetic stirrer generates a cloud of suspended, small fraction powders; (c) SEM image of a collection test performed on a 100nm-thick membrane and (d) size distribution histogram calculated from SEM images of the collected sample.

A step forward in the controlled generation of particles is achieved with the design of a custom *Aerosol desiccation pipe*, a system where sodium chloride crystals are formed from the dehydration of saline aerosol droplets. The suspension of water droplets produced by the pneumatic nebulizer (Aerosol mini neb 1000, by Microlife®) turns out to have diameters in the range of a few micrometres. As described in ref. [4], the lifetime of such small size droplets at ambient temperature and humidity is limited to a few hundred milliseconds. This implies that already a few centimetres away from the source the droplets have evaporated, leaving the dry residue consisting of NaCl crystals. Different experimental parameters such as the concentration of the starting solution, the flow velocity inside the desiccation pipe and the length of the pipe itself can be tuned to achieve different distribution of particles. As schematically depicted in Fig.4.8a, when the inlet of the chip housing is placed at the end of the desiccation pipe (length of about 1 m), the porous sampling membrane is exposed to a stream of dried NaCl crystals released in the air flow by the medical aerosol generator. The speed of the resulting air flux exiting from the pipe is monitored by an anemometer placed at the end of the tube (in correspondence with the chip housing position) and can be regulated by varying the voltage supplied to the fan at the other end of the tube. In this way also the concentration of the NaCl nanoparticles per litre of air can be modified. Collection tests are performed with the chip housing placed in a reproducible position (see Fig.4.8b)

and optimized parameters including concentration of the NaCl solution (10% m/m in milliQ-grade de-ionized water), fan speed (0,5m/s flow) and collected volume (45 seconds at 3ml/min flux).

The results of this fast concentrated collection are summarized in Fig.4.8c and Fig.4.8d, with SEM images acquired on the sample revealing the formation of regular, multi-sized cubic crystals of sodium chloride resulting from the desiccation of droplets with different starting volume. Size-distribution histograms extracted from the images reveal a high number of small particles, in the range between 200-300nm, and a fast decrease of counts for bigger particles, most likely imputable to the fact that we are collecting a small fraction of particles from a macroscopic stream which flows out of the pipe with turbulent trajectories. In comparison with the 5m/s flux speed measured with the anemometer, the flux conveyed into the collection line is considerably slower. Also in this case, hydrodynamic arguments support the observation that smaller crystals are collected more efficiently than larger ones which get trapped on the tubing walls[132,133].

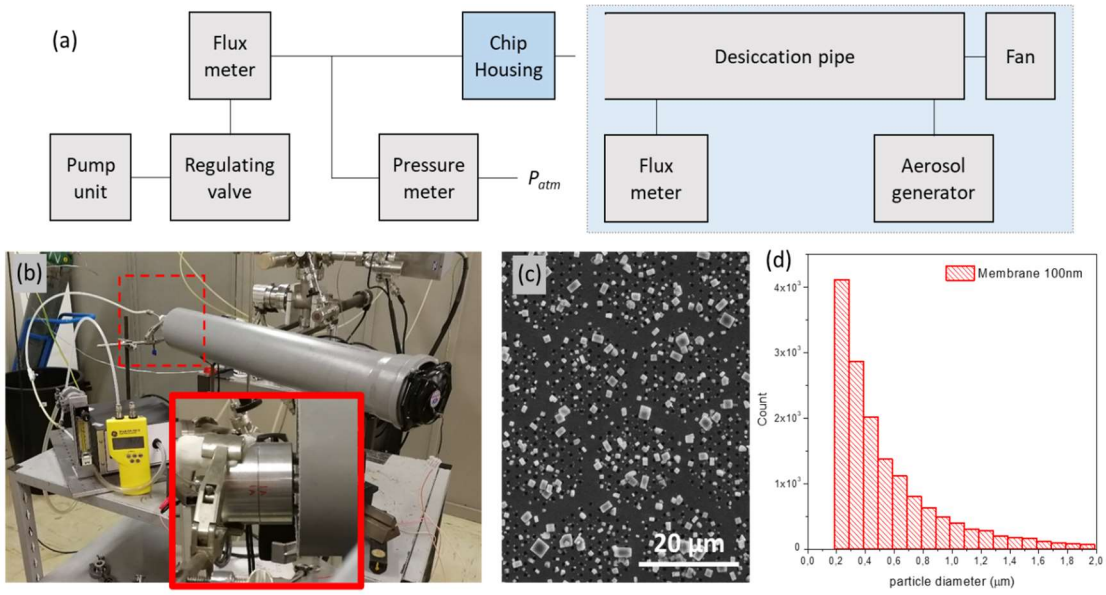

Figure 4.8: In-house designed, suspended particle generation system from liquid solution (*Aerosol desiccation pipe*). (a) Scheme of the overall configuration, with continuous aerosol generation and flux monitoring inserted among the desiccation air stream; (b) picture of the desiccation system and detail of the chip housing placed at the end of the tube; (c) SEM image of NaCl particles collected on a 100nm-thick functionalized membrane and (d) resulting size-distribution histogram of the NaCl crystals, calculated from SEM images of the membrane surface.

Finally, I also tested the membrane sampling efficiency recurring to a reference state-of-art technology for generation of particles available in the INFN environmental physics research labs jointly run by the group PM_TEN s.r.l., a spinoff of the University of Genova. The atmospheric simulation chambers, there available, allowed the study of various atmospheric processes under realistic but controlled conditions. In collaboration with PM_TEN, we had

access to this technology in a system called ChAMBRe (Chamber for Aerosol Modelling and Bio-aerosol Research)[134,135]. In an atmospheric chamber, we are able to reproduce stable particle suspensions and maintain them over extended spans of time. After injection of an aerosol of NaCl solution (using a Blaustein Atomizing Modules (BLAM) aerosol generator) into the cylindrical chamber of the instrument, desiccated droplets are kept in motion by the action of a stirring fan, rotating at the bottom of the cylinder. The suspended particles are thus continuously moved along the inner wall of the chamber, giving rise – on long timescales – to atmospheric ageing phenomena of the airborne objects[136], eventually leading to the narrowing of the size-distribution measured curves around a value determined by the initial aerosol concentration and the ageing (or *ripening*) parameters.

As schematically summarized in Fig.4.9a, the chamber is equipped with a particle monitoring unit (Optical Particle Sizer (OPS) 3330 by TSI®) constantly recording the particle density and size-distribution, and features extraction valves where our chip housing can be connected to the inner volume and the particles suspension (see Fig.4.9b). SEM imaging of the membrane after sampling, Fig.4.9c, demonstrates concentration of particles in registry with the hexagonal geometry of the pores. The resulting collection sample quantitatively analysed in terms of the size distribution and the histograms shown in Fig.4.9d, demonstrate that following aerosol generation substantial ripening takes place. The revealed particles are comprised in the range between 100 nm and 1µm, with the complete suppression of counts above 1,2 µm due to gravimetric sedimentation and an approximative balance of the smaller columns of the histograms demonstrating coalescence of the smaller objects into bigger ones.

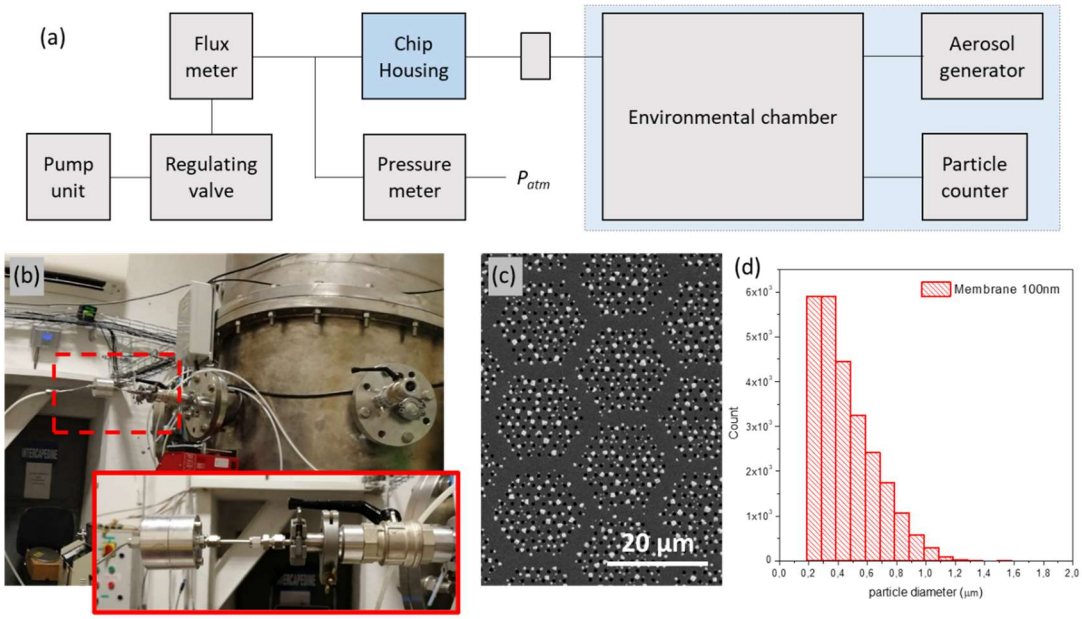

Figure 4.9: UniGe INFN environmental labs atmospheric simulation chamber for stable suspension of particles from liquid solution aerosols (*ChAMBRe*). (a) Scheme of the overall configuration, with initial injection of aerosol and continuous monitoring of the stable aerosol conditions; (b) picture of ChAMBRe with the chip housing unit connected to one of the chamber extractions valves (detail); (c) SEM image of the resulting collection on a

100nm-thick, porous membrane and (d) size-distribution histogram of the submicron particles, ranging from hundreds of nanometers to one micrometer.

4.4 Test and validation of airborne particle collection on nanofabricated membranes

The fact that our nanofabricated membranes and the miniaturised sampling setup are suitable for the collection of submicrometric airborne particles represents a success in its own for applications aiming at the development of imaging techniques for high-resolution observation of particulate matter characteristics. The resulting measurements, however, have to be - in perspective - applied in parallel to standard collection systems regulated by international standards and directives (see e.g. the European Directive 2008/50/EC). Is therefore necessary to determine the relation of our collection results with the ones obtained by other filtering/sampling systems which are certified according to reference standards, to understand and evaluate the information extracted by our samples in the context of particulate matter analysis. The final goal in this context is thus to define a transfer function which allows to determine quantitatively the density of particulate matter in the sampled air volume, reproducing in our system conditions analogue to standards. Thanks to the availability of the atmospheric simulation chamber of INFN, in first place, we can reproduce distributions of suspended reference particles, with ideal spherical geometry and monodispersed in size, chosen in the dimensional range of interest. Polystyrene (PS) spheres are a typical example of such reference particles, usually sold in the form of a liquid suspension that can be injected by a pneumatic nebulizer inside the simulation chamber and then allowing for the collection of particles on filters.

We dispersed 0.7µm PS spheres in ChAMBRe, with an initial concentration of about 700 #/cm^3 and monitored their concentration and size distribution with the available OPS particle counter. The optical particle sizer has an almost a real time measurement rate (1Hz), since the particle distribution is based on diffuse optical scattering from the microparticles distributed in size in the range between 0.3-10 µm (see e.g. Figure 4.10.d). The size of the particles and their distribution is determined according to an optical model of scattering according to Mie theory which assumes a reference value for the refractive index of the particles. The downside of this approach is, therefore, an uncertainty related to variations of the refractive index and shape of the particles, which can lead to a slightly shifted reading of the particle sizes when e.g., liquid droplets are still present in the monitored volume. This error must be taken in account when analysing the histograms reported in the following, resulting as shifted counts among size-distribution statistics.

After sampling the polymeric particles on the membranes, we conducted standard Imaging in the scanning electron microscope. For this specific kind of particles, a conductive gold coating had to be applied prior to SEM imaging, since the insulating Polystyrene particles become electrostatically charged by the electron beam and tend to be deflected and blur the scanning beam. As shown in Fig.4.10a, after particle collection and immobilization on the membranes, we deposited 40nm of gold (at a glancing incidence angle of 45 degrees) to

establish a conductive coating above the spheres and, at the same time, to highlight their geometrical features thanks to their projected shadow (see Fig.4.10b). We performed reproducible tests by extracting the air sample from the chamber at 5ml/min rate for 8 minutes, collecting in total several hundreds of PS spheres as visible in Fig.4.10c. The comparison of the particle size distribution derived from the OPS reading, recorded in real-time during the experiment, with the distribution resulting on the membrane confirms the collection capability of our nanofabricated perforated filtering systems and the almost monodisperse PS particle distribution, peaked in the range of 0.7 µm.

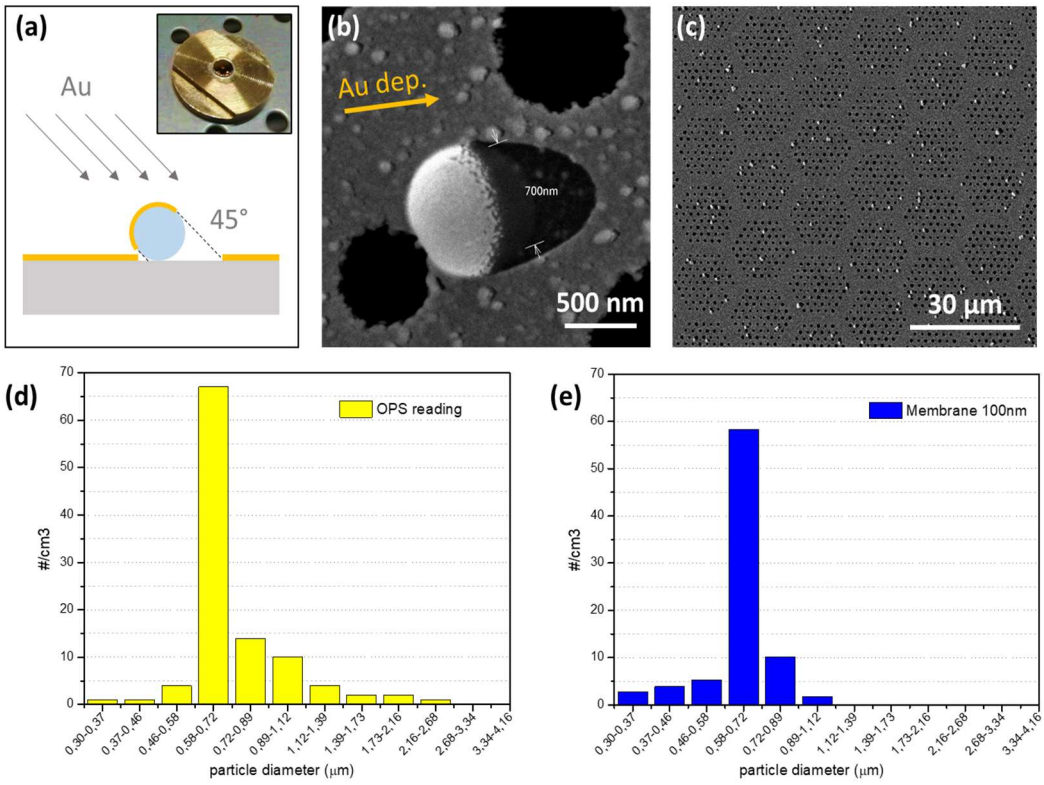

Figure 4.10: Collection efficiency of 0.7µm PS particles with respect to the OPS reference. (a) Scheme of the gold coating required for analysis of polystyrene spheres, picture of the gold-coated chip holder; (b) detail of a 0.7µm PS sphere and its deposition shadow; (c) SEM image of a 100nm-thick membrane with the collected PS spheres; (d) OPS reading of particle-density distribution in ChAMBRe during the collection and (e) collected particle distribution measured from SEM images of the membrane.

In addition to the reference measurement provided by the OPS setup, I also tested the nanoparticle suspension by sampling an equivalent volume of air driven from the chamber on commercial large area polymeric Cyclopore PCTE reference filters. Sampling took place in parallel with the collection performed on the Si_3N_4 membrane by attaching to the extraction valves parallel collection lines. The sampled particulate matter collected on the PCTE filter has then been analyzed quantitatively recurring to SEM analysis as discussed above. Following this approach, I have been able to determine quantitatively the transfer function, and the hydrodynamic size cut-off determined by the tubing and connections to the membrane with respect to a recognized standard.

The same sampling volume per unit surface of the membrane is fluxed in the two systems, based on international standards for atmospheric particulate matter collection procedures applied to the 47mm PCTE filter. This means that while a flux of 16,6l/min is conveyed to the polymeric filtering setup, an equivalent volume of 5ml/min is calculated scaling respect to the active area of the fabricated Si_3N_4 membrane. The collection is performed for 8 minutes, and the results are shown in Fig.4.11a and Fig.4.11b, respectively on 100nm-thick Si_3N_4 perforated membrane and PCTE commercial filter, highlighting how the active area of the custom fabricated membrane is confined in correspondence to the hexagonal geometry of the patterned region, where the particles are concentrated leaving almost blank the space between the holes. A qualitative comparison of the resulting collection (Fig.4.11c), anyway, reveals comparable efficiency with respect to the Cyclopore PCTE filter for particle sizes above 700 nm (the relative sampling efficiency for particles in the range 720nm-1,12um amounts to 60-70%), while a lower efficiency (around 40-50%) is found for particle size between 300-720nm (Fig.4.11d, red). These relative sampling efficiencies are mainly determined by the intrinsic size-selective features of the miniaturised sampling setup, in particular the lower diameter of the pumping line employed (1 mm vs. 47 mm diameter respectively) and the size of the membrane pores which are slightly larger in the Si_3N_4 membrane.

With this respect in figure 4.11d an interesting observation can be done in relation to the cut-off in particle sampling induced by the tubing connection between the chip housing and the chamber extraction port during collection: the presented SEM images and values refer either to a configuration (inset [A]) in which the inlet of the membrane chip is placed right in front of the ChAMBRe extraction valve via a large bore KF25 adapter (inner diameter 13.1 mm), or to a configuration (inset [B]) consisting in a 10cm long stainless steel tube with a small inner bore of 2.1 mm in diameter. In the latter case due to the hydrodynamic cut-off the resulting transfer function values are lowered to an almost constant 20-30% of efficiency in the whole range of particle sizes (Fig.4.11d, green). This highlights once more the importance of the inlet tubing geometry in the selection of particle size and demonstrates how the relation between the prototype and a reference filtering system could be tuned by accurate modification of the setup design. The choice of the design is eventually dictated by the context of application: for the collection of small particles (e.g. with diameters below 400 nm), as an example, it would be convenient to apply the inlet tubing of configuration [B], cutting-off bigger particles to optimize the relative abundance of the particles of interest.

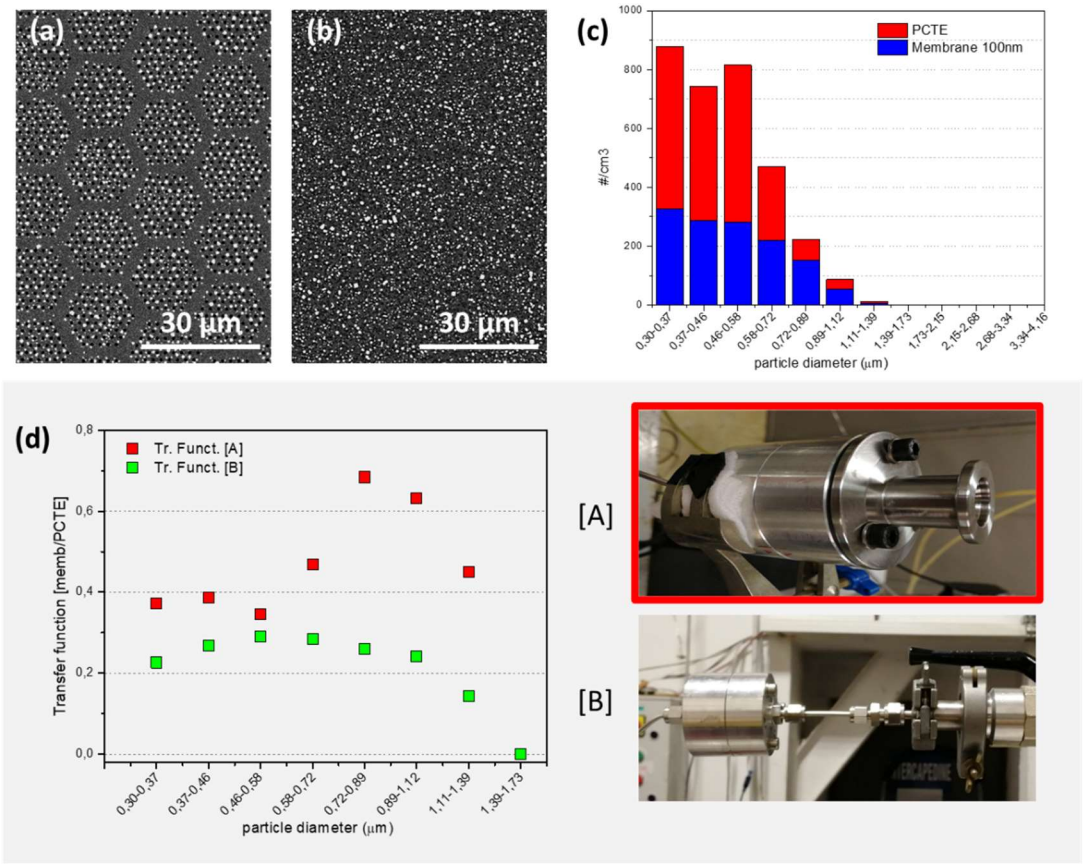

Figure 4.11: Transfer function of particle collection from membranes to Cyclopore PCTE filters. (a) SEM image of the collected particles on the 100nm-thick membrane and (b) on the PCTE filter; (c) compared particle-density distribution, calculated for PCTE filter (red) and fabricated membrane (blue); (d) resulting transfer function with [A] *direct* connection (red) and [B] *in-tube* connection (green).

Chapter 5 – Nanofabricated free-standing membranes for co-localized and enhanced spectroscopies

In this chapter, we finally focus on the application of the fabricated perforated membranes to perform co-localized experiments which allow to combine different spectroscopic techniques, addressing the same individual nanoparticles immobilised on well-defined coordinates of the membrane. The portable and miniaturised chip holder is designed to allow easy transfer of the sample between the collection setup where airborne particles are collected, and the different analytical instruments for analysis. The choice of a square shaped free-standing membrane, moreover, gives us the possibility to define unambiguously a coordinate system for localizing the particles, assigning the origin of the axis to a corner of the membrane and a pair of cartesian axes aligned along the 500µm long edges of the membrane frame. The free-standing area can thus be mapped with nanometric precision in a SEM microscope in order to identify and record the position and dimension of specific particles. The chip holder also allows easy transfer of the sample in different spectroscopic setups without recurring to complex and expensive pre-aligned manipulation stages, for performing complementary spectroscopic analysis on the specific particle of interest.

As demonstrated in chapter 4, the choice of silicon nitride membranes also derives from the advantageous properties of free-standing substrates, which positively affect spectroscopic observations in terms of reduced background. On the other side a common disadvantage of polymeric filters, as PCTE Cyclopore, is the electrostatic charging occurring on the substrate during SEM or EDX analysis, requiring graphitization or alternative methods to overcome the issue. Finally, another difficulty must be faced when performing vibrational spectroscopies such e.g. Raman spectroscopy, as the polymeric substrate is responsive to laser excitation or even damaged in case of high spot intensity. Silicon nitride thin membranes are thus ideal substrates for investigation with both electron and optical spectroscopies, due to the strongly reduced interaction with the electron beam and quasi-zero response to the excitation with commonly applied lasers.

5.1 Identification of particles by EDX Spectroscopy and mapping

After performing collection of multi-component airborne particulates and determining their size distribution and localization via SEM imaging, one of the primary challenging interests is the assessment of the elementary composition at the level of individual particles labelled with coordinates and eventually investigate them separately. EDX spectroscopy, especially if integrated into a SEM setup, is a straightforward method for elementary identification of spatially resolved components, and together with the topographical imaging of SEM can be applied to create spectral maps of the sample with localization of the different compounds.

Here I illustrate an application example of our fabricated membranes, for the assessment of a mixed airborne suspension thanks to the spectrally different X-ray fingerprints of the components. In this seminal example I used a collection of sodium chloride and iron oxide

particles, which have markedly different spectral fingerprints in their X-ray fluorescence spectrum. EDX spectroscopy excited by an electron microprobe, as already introduced at the beginning of chapter 4, is characterised by high spatial and spectral resolution and allows mapping and identifying submicrometric particles supported on the free-standing membranes. While the “point and shoot” (P&S) acquisition mode is ideal for extraction of strong signal by continuous illumination of a particle located in a selected predefined position, in the case of unknown samples decorated with randomly dispersed particles the acquisition of 2-dimensional spectral maps becomes necessary to reveal the presence of the particle within the field of view.

The software-controlled stage of the electron microscope allows to register the coordinates of objects revealed on the membrane, respect to the reference system aligned along the edges of the membrane frame – with sub-micrometric precision – thus combining images and u/v coordinates to localize each particle for further investigation with the EDX setup.

This is the case of the experiment reported in Fig.5.1, where we combined SEM imaging, spectral imaging and P&S to detect and discriminate sodium chloride and iron oxide particles, collected on a fabricated 100nm-thick porous membrane. The reported high-resolution SEM image (Fig.5.1a) reveals particles with different size, shape and contrast, suggesting the presence of both the components inside the selected field of view. This is confirmed by spectral images of the area of interest (Fig.5.1b, Fig.5.1c), which register the coordinates of pixels where sodium and iron EDX peaks are revealed, recreating an equivalent 2D elementary map of the sample while the electron beam is scanning the surface. An overlay on the two elementary maps on the SEM topographical image of the area of interest (Fig.5.1d) allows a one-to-one identification of particles as sodium chloride and iron oxide, with sufficient resolution to discriminate agglomerated particles of the two species (as the ones near the bottom left corner of the image). Once recognized the components of the collected sample, point and shoot analysis (Fig.5.1e) can be performed selecting a pair of different objects from the surveyed area, revealing signal arising from the substrate (silicon, nitrogen and gold), and from the elements composing the particles (oxygen, iron, sodium and chlorine). The observed EDX spectra, following a first identification in the spectral map, allow to recover complementary information as e.g. the weighted percentage composition of the two particles, a key aspect in the case of particles with different stoichiometry.

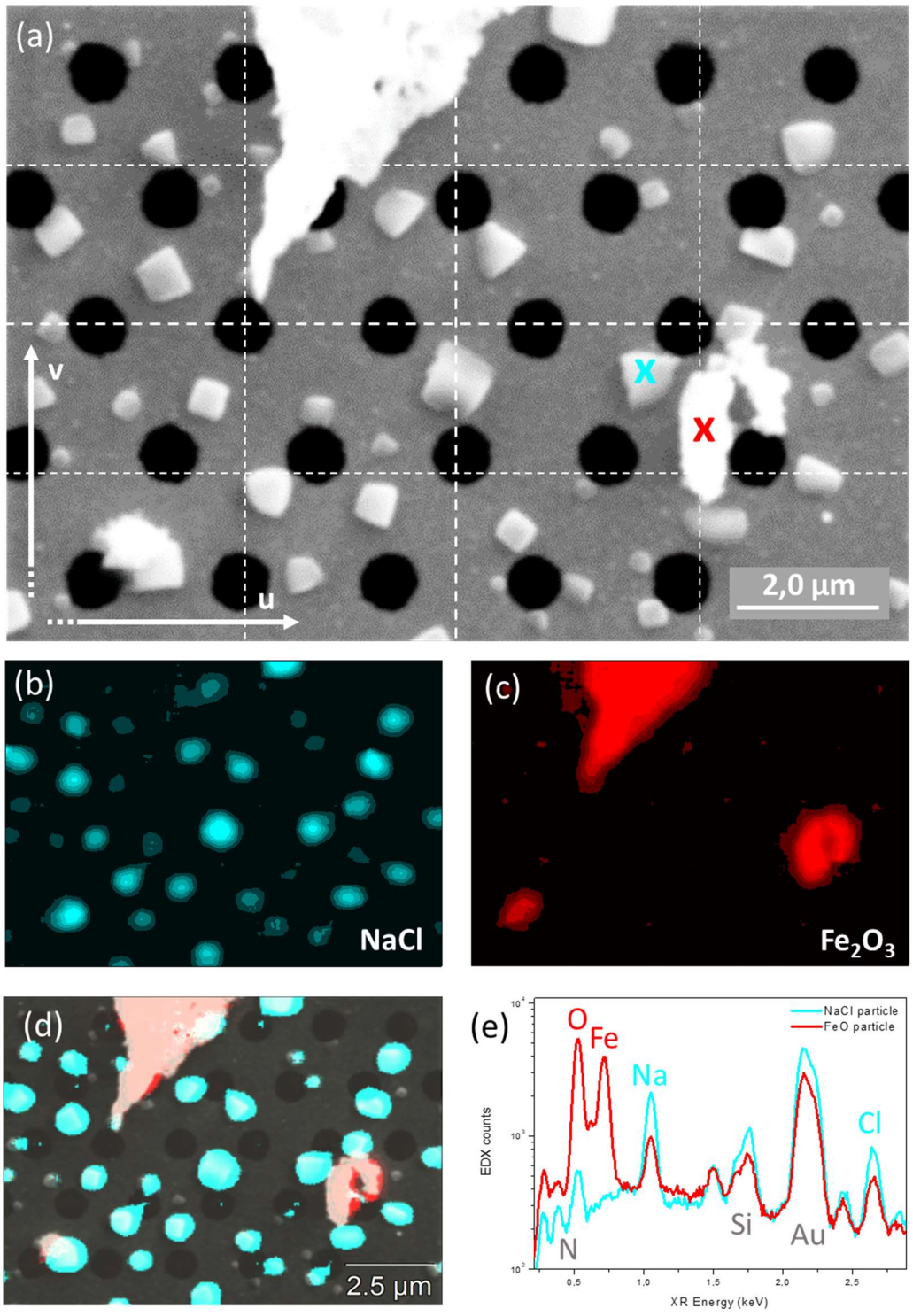

Figure 5.1: EDX identification of different particles collected on a 100nm-thick porous membrane. (a) SEM image of the investigated area (FoW=15x10µm) with u/v coordinates enabling the co-localization of the particles of interest; (b, c) EDX spectral images of the surface, referred respectively to sodium (cyan map) and iron (red map); (d) overlay of the spectral EDX images of sodium (cyan) and iron (red) with the SEM image of the analysed area; (e) Point and Shoot EDX spectra extracted from two identified particles, labelled with cyan and red markers in panel (a).

5.2 Co-localized Raman-EDX Spectroscopy for discriminating particles

The iron oxide powder (Fe_3O_4) implied in the experiment of Fig.5.1 is a combination of two different phases, with identical elementary composition and stoichiometry but different crystal structure (hematite and maghemite). As shown in Fig.5.1c this difference cannot be unveiled by elemental spectroscopies as EDX but can be possibly addressed in a vibrational spectroscopy such as Raman. We thus take advantage of the co-localization capability of membranes to identify suitable particles of the right size with SEM, verify with EDX if their elementary composition corresponds to iron oxide (and exclude, e.g. that we are investigating a grain of dust) and finally move the sample to a micro-Raman facility (Raman Horiba® J.Y. micro-Raman Explora_Plus, in collaboration with professor Marco Scambelluri) where the different phases can be studied with submicrometric spatial resolution.

We report an example of this procedure, with particles casted on a 200nm-thick porous membrane. Adopting a reference system centred in the bottom left corner of the free-standing membrane (Fig.5.2a), we assign u/v coordinates to particles imaged by SEM on the membrane, looking for objects in the 1-10 µm size range. As one can see in Fig.5.2b, we assign coordinates to selected particles with micrometric precision, thanks to the motorized stage of the electron microscope. In the example particle A is located in a position u = 332.00 µm v = 85.00 µm from the reference origin with an accuracy determined by the SEM stability at the 10 nm level.

EDX point and shoot analysis is performed on particles of interest (Fig.5.2c), clearly identifying the objects as composed of oxygen and iron atoms, with different intensity most likely related to the geometry of the particles inducing different X-ray photons extraction. The two particles A and B are analysed by spectral imaging of the area, revealing no difference in the composition of the objects in terms of iron and oxygen signals (reported in Fig.5.2d and Fig.5.2e), as expected for maghemite and hematite iron oxides.

Thanks to co-localized analysis of particle A and B in a micro-Raman spectroscopy setup with 785nm pump laser (implying safe transport of the sample to a different department with the chip holder technology), we are eventually able to detect different vibrational signals from the two iron oxide phases (Fig.5.2f). Particle B indeed demonstrates a characteristic response corresponding to the hematite phase spectra available in literature[137], with a triplet of peaks centred between 200 and 450 cm^{-1} Raman shift, and a single peak around 600 cm^{-1}. Particle A, instead, reveals an overall unstructured signal showing a single excitation mode at 350 cm^{-1}, appearing in both spectra, thus leading us to the deductive identification as maghemite phase. Unbiased recognition of the two particles can therefore be achieved by performing 2-dimensional spectral imaging, and selectively mapping the intensity of one of the characteristic peaks of hematite (294 cm^{-1}), so that a high signal corresponds to hematite particles while a low signal to maghemite particles. As shown in Fig.5.2g and Fig.5.2h, particle B confirms our expectations, clearly exhibiting the spectral fingerprint of hematite signal, while the shape of particle A is barely outlined due to the low signal which is almost indistinguishable from the background.

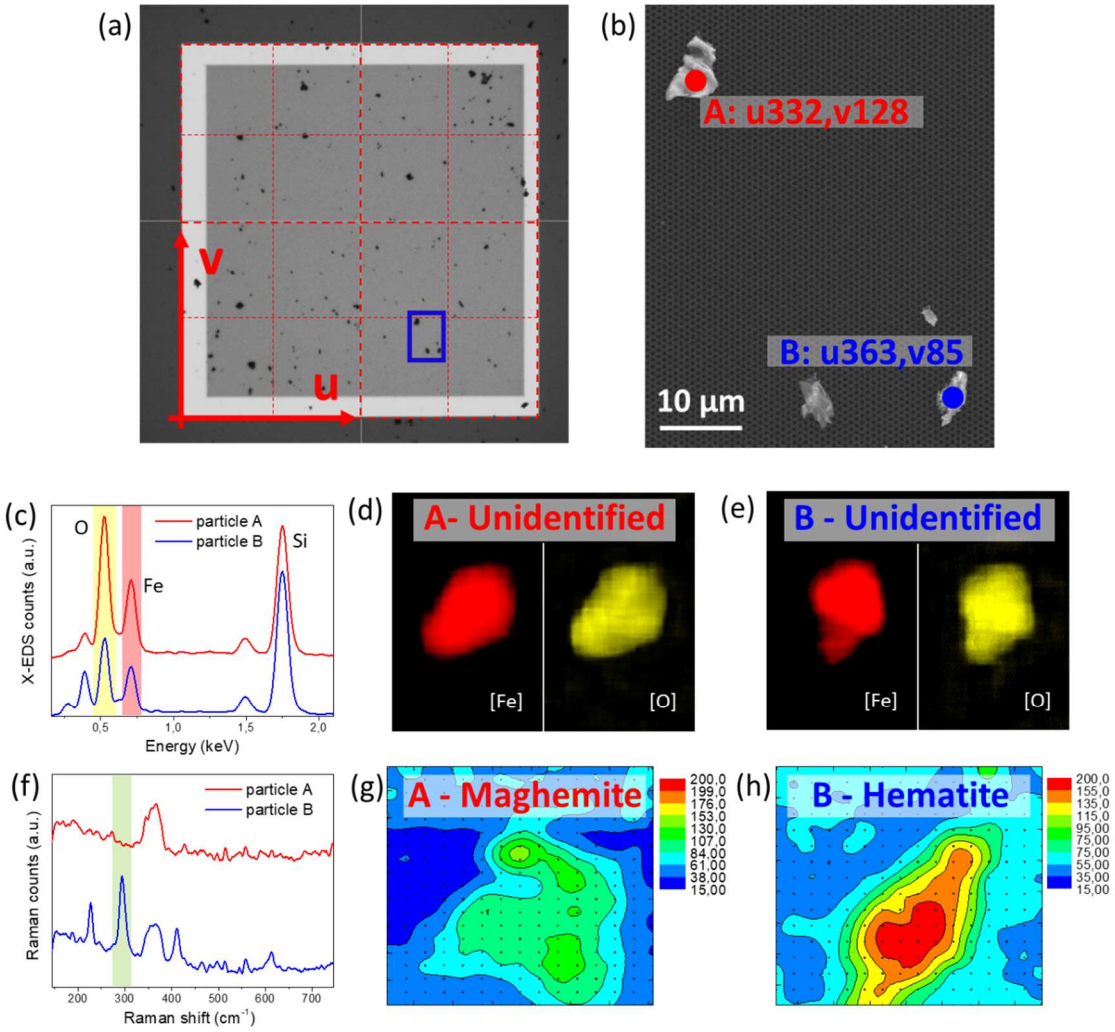

Figure 5.2: Co-localized analysis of iron oxide particles with different crystal structure, casted on a 200nm-thick membrane. (a) Reference coordinates system for co-localization of particles in different instruments, with axis origin established in the bottom-left corner of the free-standing window; (b) SEM image of a portion of the membrane, highlighted in blue in panel (a), and u/v coordinates of two particles "A" and "B"; (c, d, e) EDX spectroscopy of A and B iron oxide particles, with (c) compared spectra of particle A (red) and B (blue), and (d, e) corresponding spectral images of iron-peak (red) and oxygen-peak (yellow) signals; (f, g, h) Raman spectroscopy of A and B, with (f) compared signal and (g, h) intensity map referred to one of the hematite characteristic peaks, labelled in green in panel (f).

This experiment demonstrates how the system is capable of co-localization and how it is possible to integrate information arising from different techniques to reach complete identification of a particle with sub-micrometer spatial resolution. In the previous example however, we opted working with relatively large particles sized in the range of several micrometers.

To investigate the limit of detection of the Raman setup in the presented experimental conditions I thus performed a further set of co-localised spectroscopic experiments searching for a set of increasingly smaller Hematite particles to be co-localised and identified on the membrane's surface with EDX and Raman spectroscopy (see Fig.5.3a).

The measured Raman signal decreases according to the scaling size of the particles as shown in the spectra of Fig.5.3b, where the representative hematite peak is highlighted by the yellow band and the membrane-related peak grey band. Interestingly, by increasing as the volume of the probed hematite particle the signal from the underlying Si_3N_4 membrane decreases since shadowing of the excitation beam affects the Raman cross section according to a fourth power of the excitation intensity. The limit of detection (LoD) in these experimental conditions can be estimated by plotting the amount of counts observed for each of the three particles with respect to their size, as reported in Fig.5.3c. Fitting the values with a power function (with exponential factor <1), we find an initial rapid increase of signal for small particles and saturation for larger particles, when the volume of the investigated object becomes larger than the laser pump spot. For particles below 1 µm, in consequence, the particles signal would decrease in the range of 10-30 counts, disappearing in the observed noise.

To improve the detection capability of the system, an option is the fabrication of plasmonic structures on the surface of the porous membranes, inducing EM field enhancement features and amplifying the Raman signal as introduced in the second section of chapter 1. In the next section of chapter 5, indeed, a similar functionalization approach will be discussed.

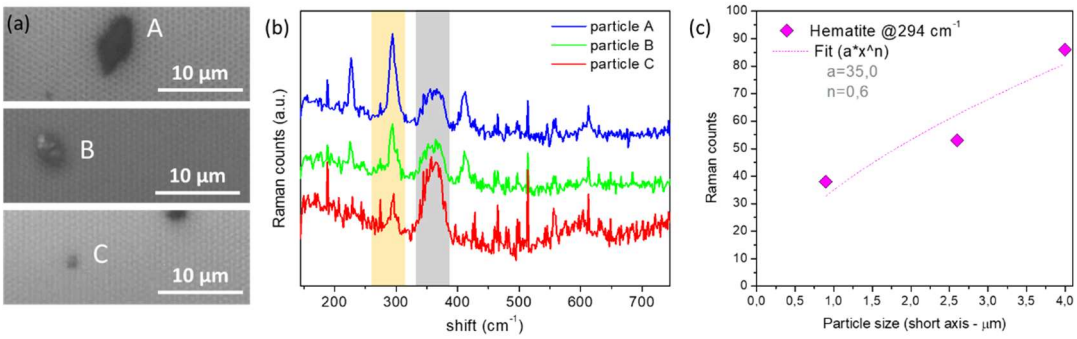

Figure 5.3: Limit of Detection (LoD) for hematite Raman signal in the presented experiment. (a, b, c) Hematite particles of scaling size, short-axis corresponding to 4.0µm (A), 2.5µm (B) and 1.0µm (C); (d) compared Raman spectra of the three particles and (e) plotted scaling intensity of the hematite characteristic-peak signal (294cm^{-1}).

5.3 Functionalization of Si_3N_4 membranes for plasmon-enhanced Raman spectroscopy

In the previous paragraph we have seen that the Raman signal from nanoparticles supported on unfunctionalized SiN4 membranes drops substantially when the size of the particle becomes comparable or smaller than the focal diameter and depth of the objective (a figure typically in the range of several hundred nanometers). Spectroscopic detection of particulate matter and molecules down to the nanometer level requires some smart functionalization of the active surface recurring to solutions derived from nanophotonics.

The concept of EM field enhancement with plasmonic structures has been introduced in chapter 1, demonstrating how the free-electron cloud of confined metallic nanostructures can be resonantly excited by the electromagnetic field. In correspondence to the resonant wavelength the scattering and absorption cross sections are strongly increased, and the electromagnetic field strength is strongly enhanced in the near-field regions which extend few tens of nm's from the nanoparticle surface where Raman-active "hot spots" are created. Under the point of view of Raman signal enhancement from the collected particles, a significant improvement can be achieved by doping the active surface area, in contact with the analytes, with highly dense arrays of plasmonic structures in correspondence to which Raman active hot spots are formed. Among possible choices for fabricating the highly dense plasmonic nanoantennas we excluded electron beam lithography (EBL) especially in consideration of the porous nature of the perforated Si_3N_4 membranes which would hinder the uniformity and regularity of the lithographic steps[138–140]. We instead preferred to adopt a bottom-up approach exploiting self-organized growth of sub-monolayer films by glancing angle deposition (GLAD)[125,127]. This fabrication method has been discussed at the end of chapter 2 and takes advantage of the self-shadowing instability which sets-in during evaporation at glancing angles via random nucleation of nanometer scale condensation clusters which grow separated from each other by nanometer scale gaps which can be tailored to provide maximum field-enhancement in correspondence to the Raman wavelength[141,142].

The technique has been initially tested on transparent fused silica samples, exploiting the laboratory vacuum growth chamber which allows to monitor in-situ and in real-time the optical extinction spectra of the nanostructures at deposition intervals of 2nm-steps (see methods section in Chapter 3.1 for further details). In Fig.5.4a, a sketch of the deposition geometry and the optical measure position illustrate how the sample can be rotated with the manipulator stage to match two different conditions. In position 1, the sample is held directly on top of an evaporation crucible for gold PVD, with an evaporation angle of 80° respect to the normal of the sample surface. When in position 2, instead, a shutter covers the evaporation crucible and the sample is crossed by a collimated beam of light, conveyed by optical fibers and coupled to an Ocean Optics HR-4000 spectrometer which acquires spectra in the Vis-NIR range of frequencies. A set of deposition steps is performed, leading to the growth of nanometric gold islands which gradually increase their size (see the SEM

topography acquired in the Backscattering channel shown in Fig.5.4b) leading to modification of the optical response. The optical extinction spectra reported in Fig.5.4c demonstrate that the self-organised array of disconnected plasmonic nanorods hosts localized plasmonic resonances, identified by the broad transmission dip recorded between 500 and 800 nm. Following the increase of deposited Au thickness we observe the decrease in optical transmittance, and a gradual redshift of the plasmonic resonance frequency corresponding to the increase in average-size and cross-section of the metal nanostructures[52].

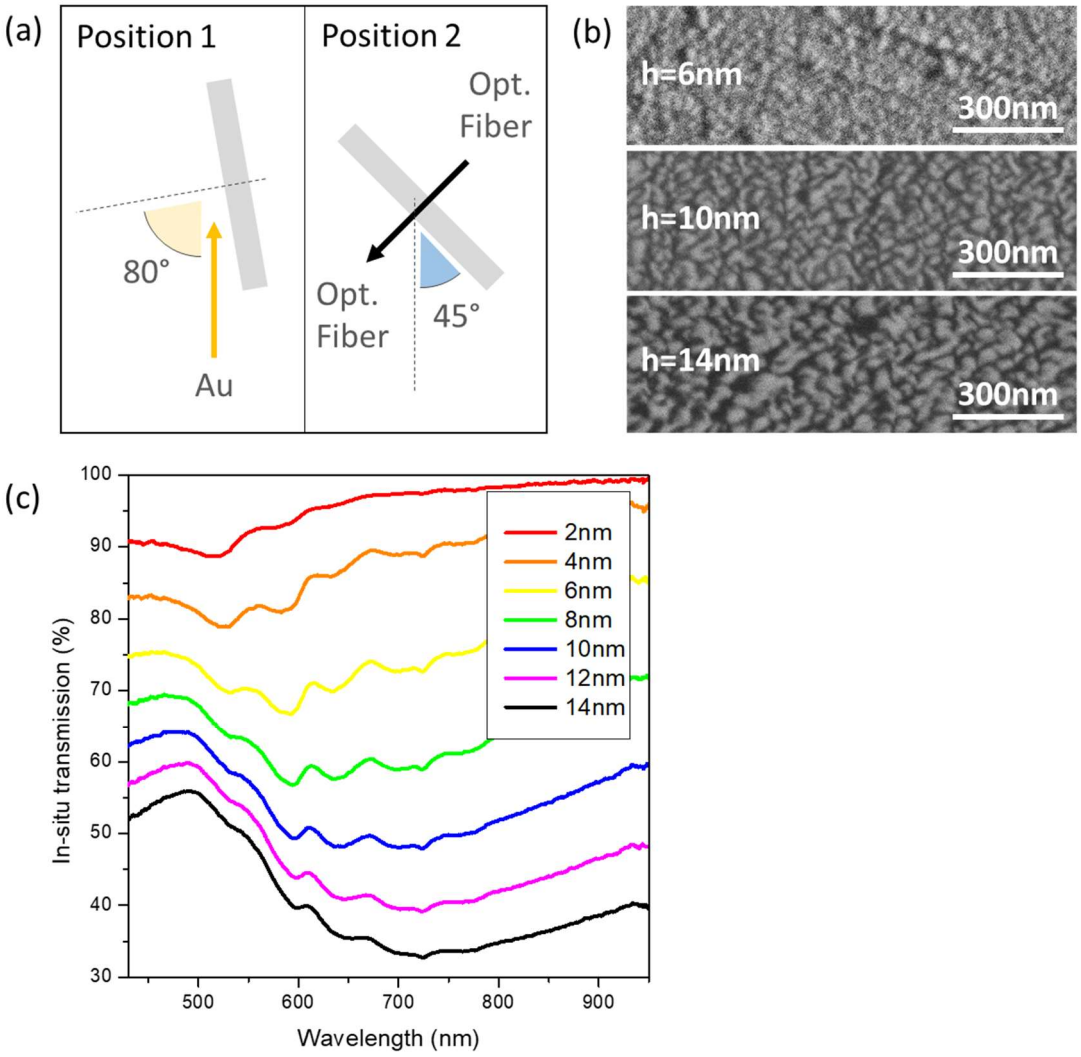

Figure 5.4: Self-assembled fabrication of high-density plasmonic features by glancing angle deposition (GLAD). (a) Schematic representation of the deposition geometry (1) and the in-situ extinction monitoring conditions (2); (b) SEM images of three different thickness deposited on flat silicon oxide substrates; (c) in-situ extinction spectra corresponding to a set of deposition steps, gradually increasing from 2 nm (red curve) to 14 nm (black curve).

Aiming to the application of functionalized samples to the enhancement of Raman signal using a 785 nm laser pump, we select the 10 nm- Au dose for the membrane modification, since for this film the plasmonic resonance matches closely the frequency of the pump laser.

To perform the fabrication on free-standing membrane chips, we mount a set of 200 nm-thick membranes with continuous (flat) and porous surface into the vacuum chamber. After the glancing angle deposition at 80° of 10 nm of gold, the samples are mounted on the chip holders (the same used for particulate collection - see section 4.2) and characterized optically in transmission using a customized optical micro-spectroscopy setup where a standard optical microscope (Labomed® Lx 400) is fiber-coupled to a spectrometer.

The investigation of free-standing membranes is performed with a spot size of about 20 µm, obtained collecting light through a Labomed 100x objective (RP Plan Achro 100x, NA 1.25 oil /0.17) and delivering the signal through thin-core optical fibers (P-100-2-UV-VIS and P-600-2-UV-VIS, Ocean Optics®) to a high-resolution solid-state spectrometer (HR4000, Ocean Optics®). The resulting micro-extinction spectra (Fig.5.5a) are acquired by normalizing the signal of the functionalized samples to the one of a bare Si_3N_4 membrane. Compared to the simple case in which a thick silica support is used, as shown in Fig.5.4c, the spectra now exhibit a much more complex response correlated to three different aspects. The first and fundamental feature is related to the reduced thickness of the involved silicon nitride membrane, since etalon interference phenomena involving light reflected at the top and bottom surfaces occur at wavelengths around 520 nm for the 200nm-thick Si_3N_4 substrate (see dashed-blue line in Fig.5.5a, normalized to air). Additionally, as a consequence of the bottom-up nanofabrication step at glancing incidence, both flat and porous membranes host the dense arrays of plasmonic nanorods. The resulting broad resonance, centred around 700 nm (green trace), is attributed to the response of such densely coupled plasmonic nanorod structures evidenced in the SEM image of Fig.5.5b. Finally in the case of the perforated Si_3N_4 the formation of new anisotropic Au features is observed as evident in the SEM image of Fig.5.5c. Due to GLAD deposition at glancing angles, on the vertical sidewalls of the circular perforations, crescent-like structures are formed and decorate periodically the top rim of the holes as highlighted in the sketch of Fig.5.5d.

In Fig.5.5a the red trace corresponds to the extinction spectra measured for the perforated Si_3N_4 membrane, decorated both with the dense array of self-organised nanorods, and with the periodic nanocrescents. The system complex response resembles that of a photonic crystal slab coated with a lossy plasmonic medium[143]. The periodic distributions of the holes and of the Au crescents efficiently couples light into the guided modes of the free-standing Si_3N_4 waveguide which are characterised by the sharp spectral features around 570 nm (GM3) and 880 nm (GM2) while the fundamental mode GM1 in the range of 1300 nm is not accessible to our spectrometer.

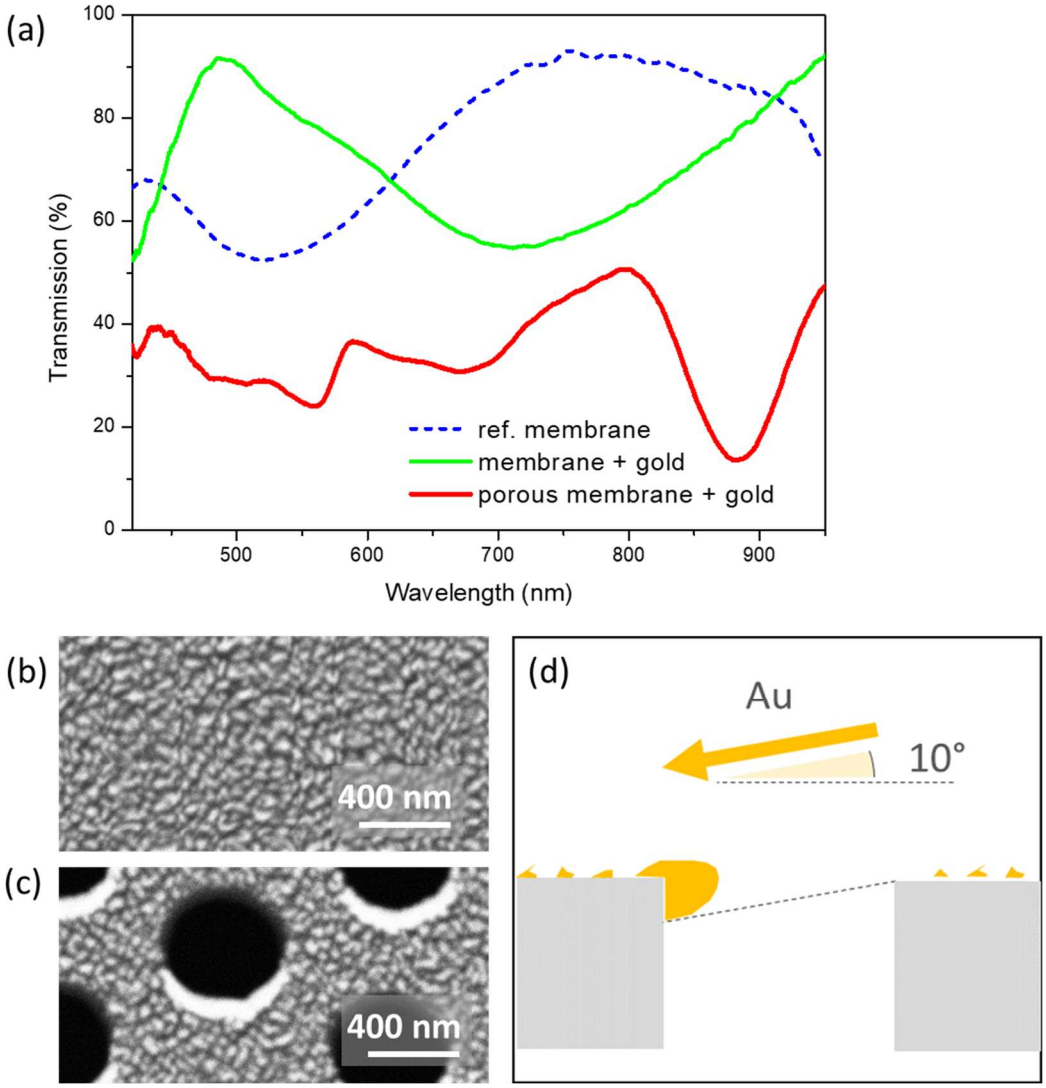

Figure 5.5: Ex-situ optical characterization of functionalized 200nm-thick free-standing membranes. (a) Transmission spectra of a continuous membrane (green) and a porous membrane (red) functionalized with 10nm of gold by GLAD, normalized to a bare membrane (blue dashed line); (b, c) SEM images of the samples, respectively depicting the functionalized continuous membrane and the functionalized porous membrane; (d) sketch of the gold nanocrescents deposition on the inner wall of the pores.

The anisotropy of the lattice, clearly observable in Fig.5.6a, can be described in terms of the asymmetric holes partially filled by the Au crescents. This biaxial anisotropy is reflected in the spectral shift of the guided mode GM2 when polarized light is oriented vertically or horizontally respectively. Changing the light polarization angle, in principle, one can couple differently with the wave guided modes supported by the anisotropic perforated array. As reported in Fig.5.6b, the two spectra are acquired on the porous membrane rotating the polarization by 90° show a 50 nm spectral shift of the guided modes (880 nm – 930 nm) attributed to the different filling factor of the anisotropic holes. On the other hand, it is important to highlight that, by rotating the polarization, the position of the plasmonic mode

attributed to the dense nanorod arrays (around 700 nm) does not shift since they are isotropically dispersed on the surface.

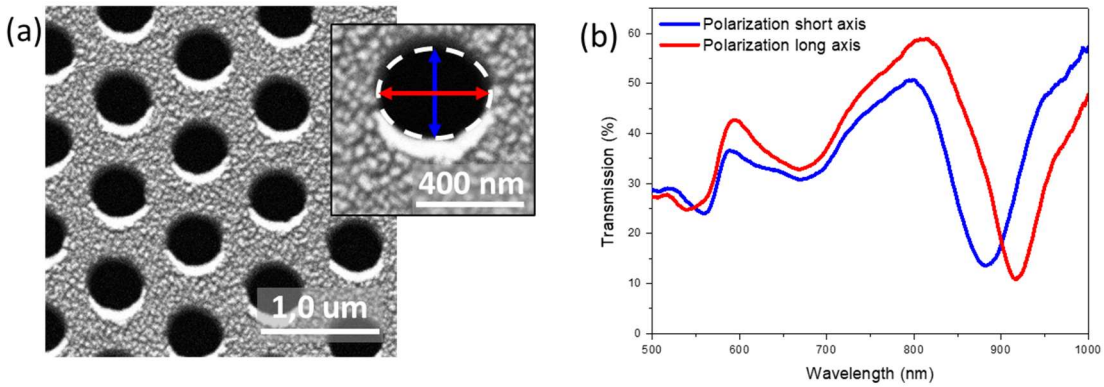

Figure 5.6: Polarization dependence of the optical modes observed in the porous 200nm-thick membrane. (a) SEM image of the functionalized membrane, highlighting the anisotropic biaxial filling of the holes by the nanocrescents; (b) transmission spectra of the porous membrane, acquired for two orthogonal polarizations labelled with arrows in the inset of panel (a).

5.4 Functionalized Raman-SERS amplification

In order to extend the sensitivity of the Raman-SERS spectroscopy, making possible the detection of particulate matter in the nm range, I tested the performance of the functionalized substrates doped with plasmonic nanoantennas in proof-of-concept Raman-SERS studies aiming at the detection of a sub-nanometer molecular probe such as Methylene Blue (MB) dye. The choice of such probe molecule is not only motivated by the abundance of reference works in the field of Raman-SERS enhancement[62,144–147], but also for the possibility of bonding a single layer of MB molecules to the surface of gold nanostructures following a straightforward and well-established method demonstrated by C. D'Andrea et al.[124,144,148].

Following[148], Methylene Blue monolayers have been deposited on our functionalized flat and porous membranes by immersion in a 10^{-5} M solution for 45 minutes followed, after rinsing in water, by a gentle blow-drying with nitrogen gas. The binding of a single (or a few) monolayer(s) of target molecule onto the membrane surface not only gives us the chance of demonstrating detection of low-concentrated samples, but also grants the presence of dye molecules in the plasmonic hot-spots formed in proximity of gold nanostructures.

Spectroscopic measurements have been conducted in a micro-Raman facility, operating a 785 nm laser with 100x objective at 0,1 % power, being able to detect meaningful and reliable signal with fast – 1 minute – acquisitions (10 sec acquisition, six accumulations). Measurements are performed keeping fixed the sampling parameters also on a reference flat gold film, exposed to the MB molecules with the same procedure adopted for the membranes, which represent the blank spectrum for evaluating the enhancement factor.

In a first experiment, I studied the Raman-SERS enhancement of the MB signal on the 200nm-thick flat Si_3N_4 membrane functionalized with GLAD nanostructures in two different configurations: membrane supported on the silicon frame or free-standing. The two regions (Fig.5.7a) are easily distinguished in the SEM images thanks to the different reflectivity of backscattered electrons, higher in presence of the Silicon frame. The optical transmittance and micro-Raman spectra are collected on both supports for comparison. The spectra shown in Fig.5.7b quantitatively confirm the SERS enhancement induced by the plasmonic nanostructures densely packed on the membrane surface: the intensity of the characteristic MB Raman mode peaked at 448 cm^{-1} is remarkably increased by more than four orders of magnitude with respect to the reference flat gold film shown in the bottom panel. The MB signal detected in the two functionalized areas, however, reveals a remarkable difference when the membrane is supported on the frame or free-standing (top and middle panel in figure 5.7c). The higher Raman signal in the free-standing case is to be attributed to light-trapping of the incident light scattered from the plasmonic nanoantennas and redirected into the free-standing membrane where it is trapped and waveguided by total internal reflection. Conversely when the Si_3N_4 membrane is supported by the silicon frame which is characterised by a higher refractive index, leakage and absorption of radiation into the silicon substrate becomes the dominant process.

It is worth to say that in the spectra presented in figure 5.7c, the enhancement factor calculated by comparison with the reference gold film represents only an underestimate of the real enhancement, since the MB signal on the reference is comparable with the overall noise at this laser power (see Fig.5.7c). Replicating the observation on the porous membranes which couple light more strongly, however, we expect an even higher Raman enhancement since the Raman cross section depends on the fourth power of the excitation field[144].

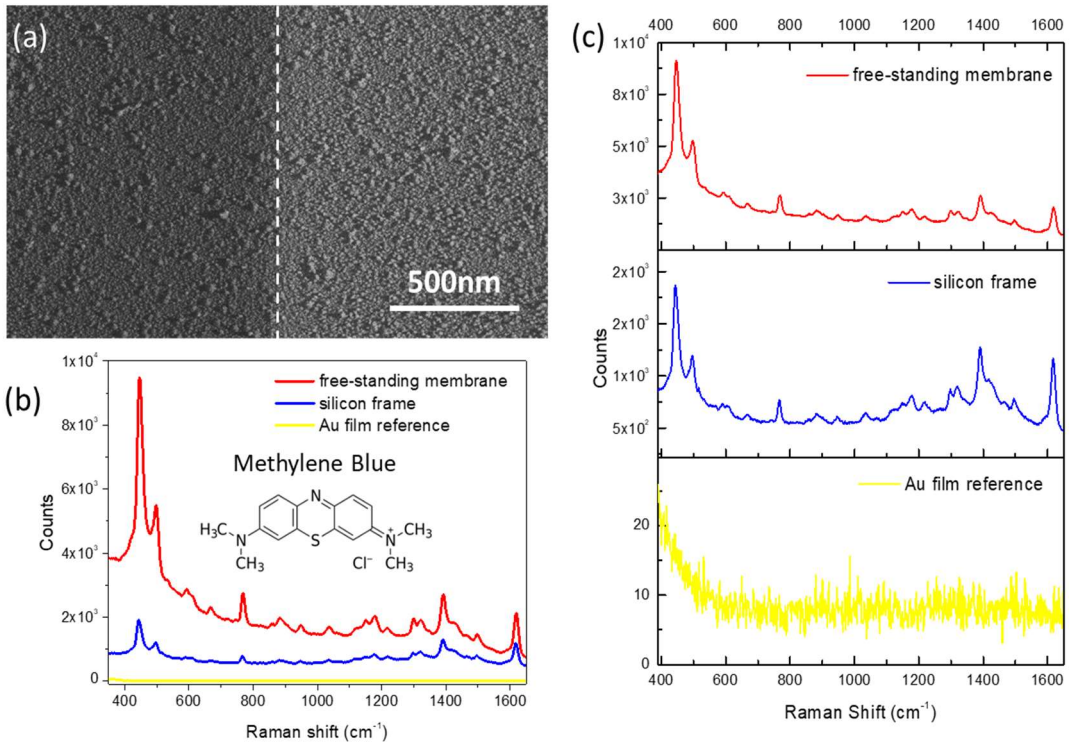

Figure 5.7: Raman-SERS response of a Raman-active dye (methylene blue, MB) monolayer, detected on a functionalized 200nm-thick membrane. (a) SEM image of the nanostructured surface, depicting the boundary between the free-standing window (darker, left side) and the silicon frame (brighter, right side); (b, c) Raman-SERS spectra acquired on the free-standing window (red), on the frame (blue) and on a gold reference flat film (yellow).

In Figure 5.8 I describe the same Raman investigations of MB adsorption, comparing the MB signal from a 200nm-thick functionalized porous membranes, with that of a flat membrane. We perform the micro-Raman acquisition employing identical parameters, so that any difference in the resulting spectra is due to different amplification of the methylene blue signal (apart from slight differences in the focusing conditions).

Additionally, in Fig. 5.8 we also compare the signal with the one of the membrane supported on the silicon frame. Remarkably the signal detected on the porous area is almost one order of magnitude higher than that on the flat free-standing area, and two orders of magnitude higher respect to the functionalized frame (Fig.5.8b).

The different enhancement measured in the three regions can be explained by referring to the optical features observed in the previous paragraph. The porous membrane exhibits the highest Raman enhancement since the hexagonal lattice of holes and crescent-shaped antennas behaves as a photonic crystal slab which efficiently couples the incident Raman pump photons into the 200 nm-thick membrane. Actually, the fact that the Raman pump wavelength at 785 nm does not match the GM2 guided mode excitation around 880 nm implies that the observed amplification is not even resulting from a resonant-Raman configuration, and in principle a further substantial enhancement of Raman-SERS gain should

be achieved by tuning the holes size, periodicity and membrane thickness until to match the guided mode matches with the laser pump. I finally stress that the remarkable SERS gain observed on the functionalised membranes depends on the very high density of active hot spots, in the range of 10^{11} #/cm^2 which are produced by means of the self-organised GLAD deposition process. Any other top-down nanofabrication process like EBL would not be able to compete with the self-organised process in terms of areal density of nanostructures.

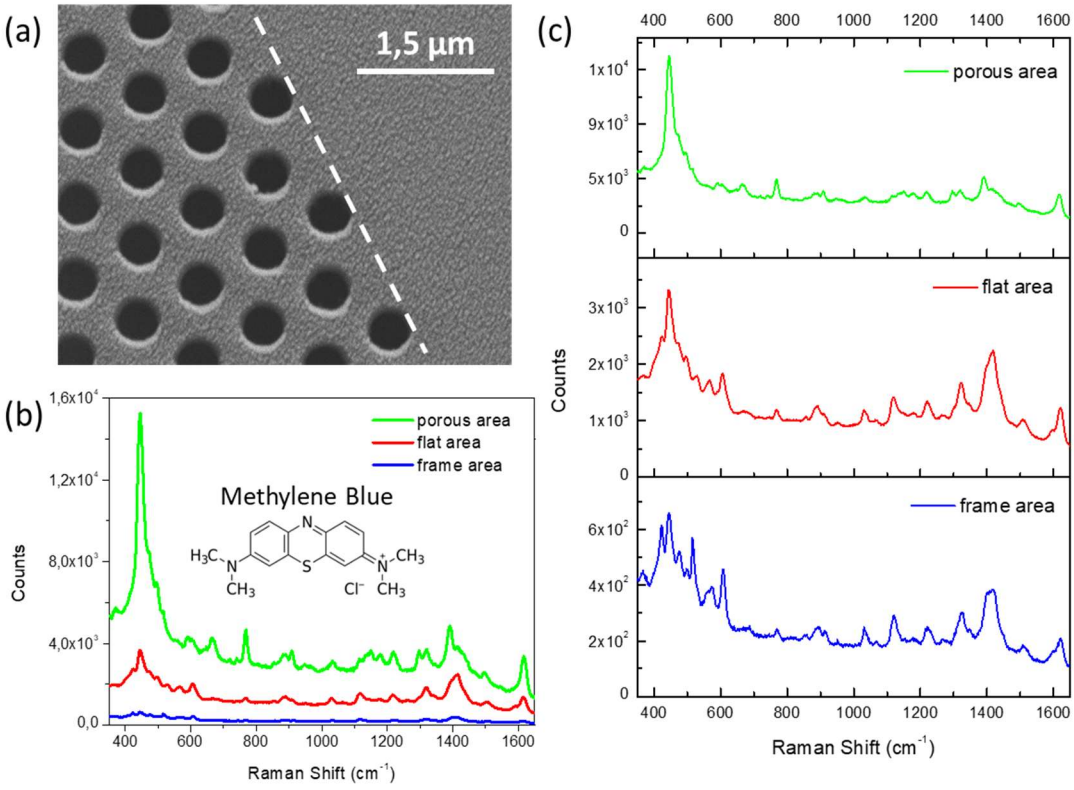

Figure 5.8: Raman-SERS of a MB monolayer, detected on a functionalized 200nm-thick, porous membrane. (a) SEM image of the nanostructured surface, acquired at the boundary between the porous and the continuous (flat) region of the free-standing window; (b, c) Raman-SERS spectra acquired on the functionalized chip, respectively on the free-standing porous area (green) and flat area (red), and on the adjacent frame area (blue).

Chapter 6 – Flat-optics nanogratings for liquid RI sensing

The nanofabrication of periodic gratings has been introduced in chapter 2.2 as one of the more interesting applications of Laser Interference Lithography (LIL). In the first period of my doctorate, I contributed to the development of a new LIL setup within my research laboratory. In particular we optimised the nanofabrication of periodic nanogratings extending homogeneously over large areas (cm^2 scale), demonstrating a strong dichroic plasmonic response giving rise to a resonant near-field enhancement with potential application in sensing[149–151].

Various sensing templates and configurations have been so far proposed, demonstrating high sensitivity at the surface of thick solid-state substrates thanks to the strong near-field confinement supported by plasmonic thin films[152–157]. However, the state-of-the-art sensors based on thin metallic films require bulky optical setups, opening a serious issue in view of sensor miniaturization and integration within ultra-thin supports. A promising alternative, compatible with ultra-compact systems, is based on plasmonic nanoantennas that can be easily arranged, forming periodic arrays. The latter are characterized by resonant 'hot-spots' localized in the inter-antenna nanogaps that give the peculiar possibility to strongly enhance weak signals emitted by molecules lying in proximity of the nanoantennas. In this way a plasmonic metasurface behaves as an ultra-thin sensor that enables the detection of very weak optical signals, such as in Raman or in non-linear optical spectroscopies[158,159].

In parallel, plasmonic metasurfaces can be easily exploited as refractive index sensors thanks to their strong spectral sensitivity to the dielectric environment[160,161]. However, in this context the spectral sensitivity is typically limited due to the broadband nature of the plasmonic resonance. In order to overcome this issue, plasmonic nanoantennas can be arranged in the form of periodic nanogratings. Under this condition narrowband Rayleigh Anomalies (RAs) can be excited thanks to the coupling of light momentum to the periodic lattice (as discussed in chapter 1.1.1), achieving strong electromagnetic confinement at the interface. Interestingly, two different optical effects can be engineered in these diffraction nanogratings in order to optimise their sensing and/or photon harvesting performances, and this will be the focus of this chapter. In section 6.1, resonant coupling of the RAs to the localised plasmon resonance is discussed, resulting in narrowband Lattice Resonances due to Fano interference and improving the spectral sensitivity to the refractive index of the surrounding medium[162–164]. In section 6.2, instead, guiding and/or waveguiding of the propagating RA mode within the substrate is discussed, such as Guided Mode Anomalies (GMA), representing a very effective way to amplify light coupling to the metasurface, promoting high sensitivity in Raman spectroscopy,[165] or strong photon absorption enhancement in ultrathin two-dimensional (2D) layers[57,58].

Under the point of view of nanofabrication, chapter 6.1 is focused on the application of large area methods (LIL), briefly introducing the nanofabricated structures and their influence on sample properties, and the sensor mechanism (more details about LIL have been discussed

in chapter 2 and 3), while chapter 6.2 is focused on the high-resolution Electron Beam Lithography (EBL) fabrication of periodic nanogratings on ultra-thin dielectric membranes.

6.1 Large-area flat-optics nanogratings on transparent substrates

Large area fabrication of ordered polymeric gratings has proven a successful and highly reproducible method to prepare plasmonic templates, as discussed thoroughly in chapter 2.2 and in the section reserved to LIL in chapter 3. In a work published during 2020[166], we have demonstrated successful nanofabrication of a Refractive Index (RI) sensor based on highly ordered plasmonic lattices, extending over large-area templates (cm^2 scale). These nanogratings can be optically probed within a fast, compact, and sensitive detection scheme, enabling flat-optics RI sensing into a microfluidic device capable of sampling liquid volumes at the sub-picoliter scale.

6.1.1 Fabrication of large-area nanoantenna arrays

Anisotropic 1D arrays of subwavelength gold nanostripes have been fabricated over large-area templates exploiting an original variant of LIL specifically developed for patterning transparent substrates, Au thermal evaporation, and chemical lift-off. The method enables combining a high degree of order, provided by the polymeric LIL mask, and large-area homogeneity of the pattern as shown in Fig.6.1a. Here, the picture of the sample highlights the presence of optical diffraction fringes corresponding to the nanopatterned polymeric film area (~2 × 2 cm^2). The AFM image and the line profile shown in Fig.6.1b and Fig.6.2c demonstrate the high degree of order in the 1D Au nanostripe arrays, which are characterized by periodicity, $p = (293 \pm 6)$ nm, as evaluated by the self-correlation pattern of the AFM topography. This value is in good agreement with the theoretical periodicity $p = \lambda/(2\,sin\,\theta) = 287$ nm for a Lloyd interference pattern generated by coherent laser illumination at the wavelength $\lambda = 406$ nm and the incidence angle $\theta = (45 \pm 1)°$. The laser beam is tuned at 406 nm in order to impress the photoresist layer (AZ701MIR) within its sensitive window. The nanofabrication method also enables controlling the characteristic peak-to-valley height of the nanostructures, h, here reading about 17 nm (Fig.6.1c), by tailoring the Au thickness deposited on the substrate during the thermal evaporation process. The SEM image shown in Fig.6.1d clearly evidences the high degree of order of the pattern and the lateral disconnection of the nanostripes (brighter regions), whose characteristic width reads about 96 nm. Remarkably, the subwavelength Au nanostripe continuously extends over the macroscopic distance (~ cm), enabling optical and/or electrical probing of these samples over a large area.

Here, the optical response of the nanostripes (NSs) was investigated by far-field optical extinction spectroscopy under normal incidence illumination of the sample over a broadband near-UV to VIS and NIR spectrum (Fig.6.1e). In accordance with the morphological anisotropy, we detect a strong dichroism in the optical response excited with polarization of the incident light either longitudinal (TE-pol, dotted line in Fig.6.1e) or transversal (TM-pol, continuous line in Fig.6.1e) with respect to the NS's long axis.

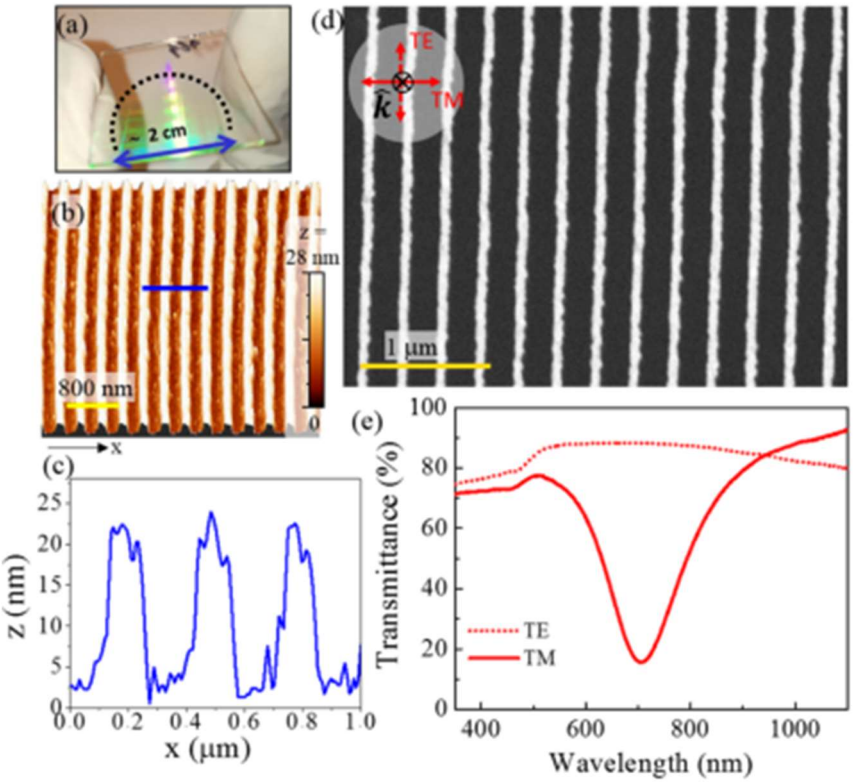

Figure 6.1: (a) Photograph of the 1D photoresist gratings supported on the large-area glass template. The green fringes due to optical interference in the gratings are clearly detected over a large area on the cm2 scale. (b) AFM topography of the 1D gold NS arrays and (c) AFM-cross section profile relative to the blue line in (b). The yellow scale bar corresponds to 800 nm. (d) Top-view SEM image of the Au NS arrays acquired in the backscattering channel. Corresponding yellow scale bar denotes 1 μm. (e) Corresponding optical extinction spectra detected under normal incidence large-area NUV–VIS–NIR illumination for longitudinal (TE-pol, dotted line) and transversal (TM-pol, continuous line) polarization, respectively.

6.1.2 Narrowband modes and Rayleigh anomaly

For excitation with TE-polarized light, we observed high optical transmittance, above 80%, and the spectrum shows a behavior similar to that of a flat continuous Au thin film,51 characterized by the onset of s–d interband transitions at about 530 nm wavelength. Conversely, the TM spectrum exhibits a strong transmission dip tuned at about 706 nm wavelength, due to the excitation of a LSP resonance confined along the short axis of the metallic NSs. The high homogeneity of the pattern enables exciting the LSP mode with high efficiency, recording a narrowband resonance whose Full Width Half Maximum (FWHM) reads about 197 nm. The possibility to further reduce the resonance bandwidth represents a desirable feature in view of RI sensing applications; however, a significant reduction is generally limited by the intrinsic ohmic losses inherent to the metallic nanoantennas. In order to overcome this issue, the excitation of plasmonic LRs in highly ordered plasmonic gratings can be exploited to increase the spectral sensitivity when these photonic modes, are

coupled to LSP resonances achieving narrow band Fano interference[163,167]. The morphology of the Au NS gratings described here reveals long-range order and homogeneity, which suggests the possibility to tailor the LR excitation.

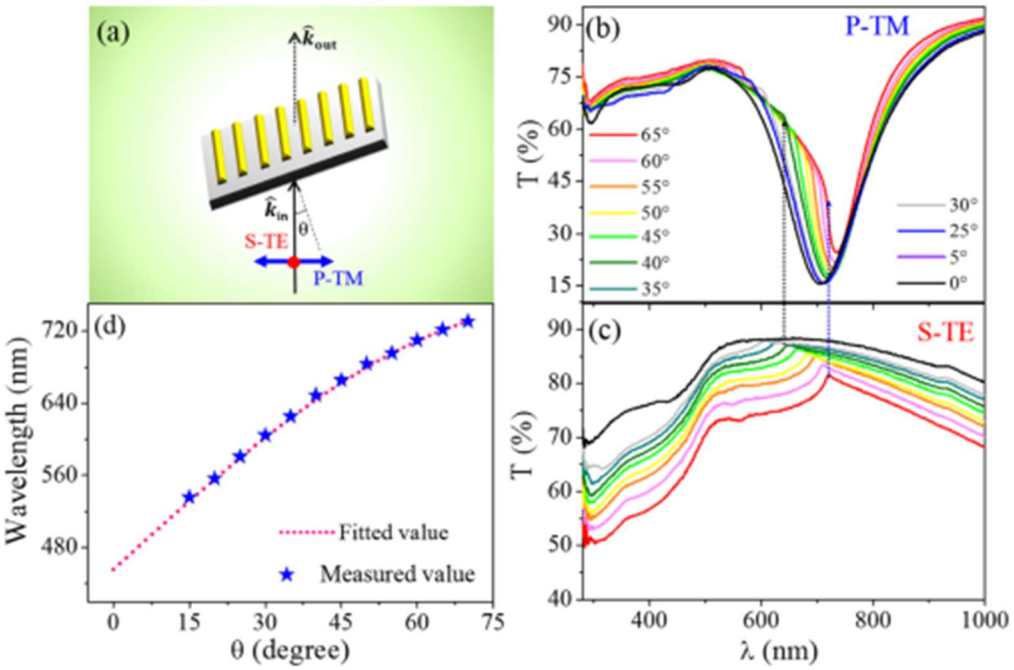

Figure 6.2: (a) Schematic diagram of the optical configuration adopted in the angle-resolved extinction measurements. The sample was rotated parallel to the light incidence plane and was excited with p-TM and s-TE polarized light. (b,c) Transmission spectra of Au nanostripe arrays detected under an increasing light incidence angle, θ, from 0° (black curve) to 65° (red curve). The investigated sample is based on Au NSs characterized by a height of 17 nm, a periodicity of 293 nm, and a width of 96 nm. (d) Dispersion of the diffraction mode detected in (c) (blue stars) and the fit (pink dotted line) of the experimental data based on the RA eq. 6.1.

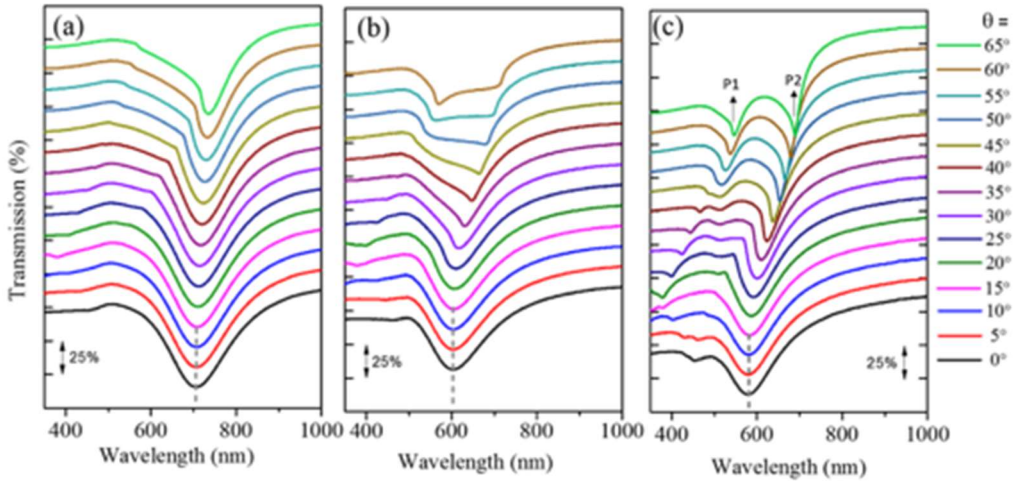

Figure 6.3: Figure 4. Angle-resolved transmittance detected for p-TM polarization of the incident light on Au NSs of height, respectively, reading (a) 17, (b) 25, and (c) 65 nm. The

periodicity and width of NSs are kept constant in all the three samples and read 293 and 96 nm, respectively. The incidence angle of light with respect to the substrate normal was varied from 0° to 65°.

In particular, we detected the optical transmittance in the extinction configuration for different incidence angles θ of the photons, which were either p-TM or s-TE polarized as shown in Fig.6.2a. These optical configurations allow to effectively couple the incident photons to the grating. For excitation along the p-TM direction (i.e. when the light is polarized along the nanostripe's short axis) (Fig.6.2b), as θ increases, the LSP resonance gradually modifies its shape with a sharpening and a gradual red-shift is observed. In particular, a strong asymmetry and narrowing of the LSP resonance, recalling a Fano-like interference, is observed at grazing incidence (i.e., $\theta = 65°$, red curve). This effect can be attributed to a resonant coupling between the broadband-localized plasmonic resonance and the lattice mode resonance sustained by the NS gratings[167]. The possibility to switch-off the LSP resonance by changing the incident light polarization to s-TE (i.e., when the incident light is linearly polarized perpendicular to the incidence plane and perpendicular to the nanostripe short axis) (Fig.6.2c) allows us to independently highlight the presence of the extraordinary transmittance LR feature, which spectrally overlaps with the Fano-interference mode detected for p-TM excitation of the nanogratings (Fig.6.2b). The latter gradually red shifts from 630 nm wavelength up to 725 nm as θ increases from 0 to 65°, where a stronger coupling between the two modes is observed. Remarkably, a dispersive behavior, characteristic of a LR, is highlighted in Fig.6.2d where the resonant wavelength (i.e., the extraordinary transmittance maximum in the s-TE spectra, Fig.6.2c) is plotted as a function of incidence angle. In particular, we can consider our system as a plasmonic lattice of periodicity $p = 293\,nm$, which exhibits light diffraction at the resonant angle (Rayleigh condition) when a diffracted order propagating in the upper/lower half-space (respectively air/liquid or substrate) crosses the boundary, according to the following equations[168]:

[eq. 6.1]

$$m\lambda_{RA\_s} = p(n_s\, sin\theta + 1)$$

[eq. 6.2]

$$m\lambda_{RA\_a} = p(n_a\, sin\theta + 1)$$

where m corresponds to the diffraction order, λ_{RA_s} and (λ_{RA_a}), respectively, denote the wavelength of the RA propagating at the substrate/air interface, ns represents the RI of the substrate (in the case of glass $n_s \approx 1.5$), and na represents the RI of the external medium ($n_a \approx 1.0$ in the case of air). The fit of our experimental data according to eq. 6.1 (dotted red line in Fig.6.2d) clearly demonstrates the nature of the detected LR mode, corresponding to a first-order RA confined at the substrate interface λRA_s. The RI of the substrate calculated from the fit of the diffraction mode according to relation (eq. 6.1) reads ns = 1.5, which is well compatible with the expected value for glass.

The experiment described in Figure 3, employing thin Au NSs of height $h \approx 17$ nm, successfully demonstrates that it is possible to deeply manipulate light propagation through a large-area plasmonic lattice by simply tailoring the illumination conditions in order to achieve spectral overlap between the RA mode and LSP resonance. We stress that in Figure 3c the visibility of the external RA, λ_{RA_a}, confined at the air interface is limited by both the weak extinction cross section of the NSs, which scales with their volume (height), and by the poor spectral overlap with the LSP resonance. Indeed, in order to achieve high sensitivity in the RI detection, it is the λ_{RA_a} mode, which should be monitored because, according to eq. 6.2, its wavelength directly depends on the dielectric properties of the medium in the outer half space. In order to optimize the detection performance of our systems, we tailored the height of the NSs, keeping fixed their width $w = 96$ nm and periodicity $p = 293$ nm.

In particular, we characterized via angle-resolved optical spectroscopy, the extinction spectra of three different samples corresponding to $h = 17$, $h = 25$, and $h = 65$ nm (Fig.6.3a to Fig.6.3c, respectively, the spectra were vertically shifted of 15%). As the NS thickness increases, we observe a strong change in the optical response of the plasmonic nanoarray. This originates from a stronger coupling between LR and LSP resonances because their respective extinction efficiencies scale with the volume of the individual nanoantenna. Moreover, the bare LSP resonance detected at $\theta = 0°$ (black curves) shows a blue shift from 706 nm wavelength (Fig.6.3a, $h = 17$ nm) to 600 nm (Fig.6.3b, $h = 25$ nm), and to 590 nm (Fig.6.3c, $h = 65$ nm).

This effect is induced by the gradual increase of the nanoantenna aspect ratio h/w,[52] which is tailored from 0.18 up to 0.68. We also notice that additional effects can be observed for higher incidence angles: (i) for the thinner nanoantennas (Fig.6.3a), the nondispersive nature of the LSP resonance dominates the spectra at all angles, and the coupling with the substrate RA, λ_{RA_s}, is substantial only at large incidence angles; (ii) for the thicker NSs (Fig.6.3b,c), the stronger coupling between the LSP mode and both substrate and external RA determines a substantial reshaping of the extinction spectra even for low-incidence angles. The degree of asymmetric reshaping of the LSP resonance becomes already evident under illumination angles as low as 30° and strongly increases at more grazing incidence, eventually splitting into two narrow transmittance dips (P_1 and P_2), which are endowed with a clear dispersive nature. For $h = 65$ nm and $\theta = 65°$ (Fig.6.3c), one observes intensity narrowing in between the dips P_1 and P_2, respectively, detected at 545 and 690 nm, and a substantial narrowing of their linewidth, which shrinks down to a FWHM of 35 and 22 nm, respectively. In order to unambiguously identify the origin of these modes in Fig.6.4a we show their optical dispersion behaviour detected in spectroscopy (i.e. resonant wavelength vs θ). In the same plot, we added the theoretical values of λ_{RA} at the substrate and external interface, evaluated according to eq. 6.1 and 6.2 and assuming no free fitting parameters ($p = 300$ nm, $n_s = 1.5$, $n_a = 1.0$). Because of the sensitivity of the resonant wavelength λ_{RA_a} to the external RI, n_a, and considering the narrowband nature of P_1 and P_2, this mode represents the ideal candidate for evaluating the RI sensitivity of our low-cost and large-area templates.

6.1.3 RI sensing application

The transparent substrate enables an easy integration of the plasmonic arrays into a simple microfluidic device active over macroscopic areas. By exploiting the large-area homogeneity of these plasmonic templates, RI sensing can be indeed performed employing a standard spectroscopic extinction configuration based on a macroscopic collimated beam (diameter = 1 mm), without need of focused optical setups. A large-area microfluidic cell (size 18 × 15 mm^2) was prepared on top of the plasmonic gratings by exploiting a suspended glass coverslip, which enables the vertical confinement of the liquid within a tiny gap (~500 µm), while two microfluidic tubes sealed on the opposite sides of the cell control the liquid flow. In the microfluidic configuration employed, the active volume of the sampled liquid illuminated by the optical beam amounts to 0.4 nL. The optical transmittance through the cell was detected under glancing angle illumination ($\theta = 65°$) in order to exploit the narrowband P_1 and P_2 spectral features (Fig.6.3c) for sensing purposes.

Subsequently, the RI of the external medium n_a was gradually increased from 1 (green curve) to 1.45 (red curve) as shown in Fig.6.4b, detecting a significant RI sensitivity of both the optical features P_1 and P_2, which red shift in response to an increase of RI in the external medium. A quantitative analysis of the resonant wavelength of P_1 and P_2 is shown in Fig.6.4c and Fig.6.4d, which demonstrates that both λ_{RA_a} and λ_{RA_s} follow a clear linear trend versus external RI. A linear fit of the resonant wavelength plotted as a function of the RI allows estimating the RI sensitivity, $S_\lambda = \partial\lambda/\partial RI$, defined as the slope of the curve. Here, the sensitivity calculated exploiting the experimental data reads $S_\lambda = (275 \pm 4)$ nm/RIU for P_1 and $S_\lambda = (19.5 \pm 1.0)$ nm/RIU for P_2. The different behaviors of the two resonant features can be explained by considering their different origin: the optical mode P_1 corresponding to the external RA λ_{RA_a} is directly sensitive to the RI na of the outer half-space occupied by the liquid (eq. 6.2), while in the case of mode P_2 corresponding to the substrate-confined RA, λ_{RA_s}, the sensitivity to the outer medium is very limited because it derives from the weak evanescent coupling. According to eq 6.2, we can estimate the theoretical RI sensitivity for the substrate-confined RA, $S_{\lambda RA} = \frac{\partial \lambda RA}{\partial na} = p\, sin\theta = 275$ nm/RIU, by assuming the experimental conditions employed here ($p = 300$ nm, $\theta = 65°$). The agreement between the experimental and theoretical sensitivity is remarkable and further confirms the validity of our assumptions. Based on the above considerations we can also anticipate that the sensitivity $S_{\lambda RA}$ could be enhanced up to values in the 10^3 range by increasing the period p of the grating (and the wavelength of the external RA λ_{RA_a}) around 1000 nm where low-cost spectrometers equipped with Si detectors can still be employed.

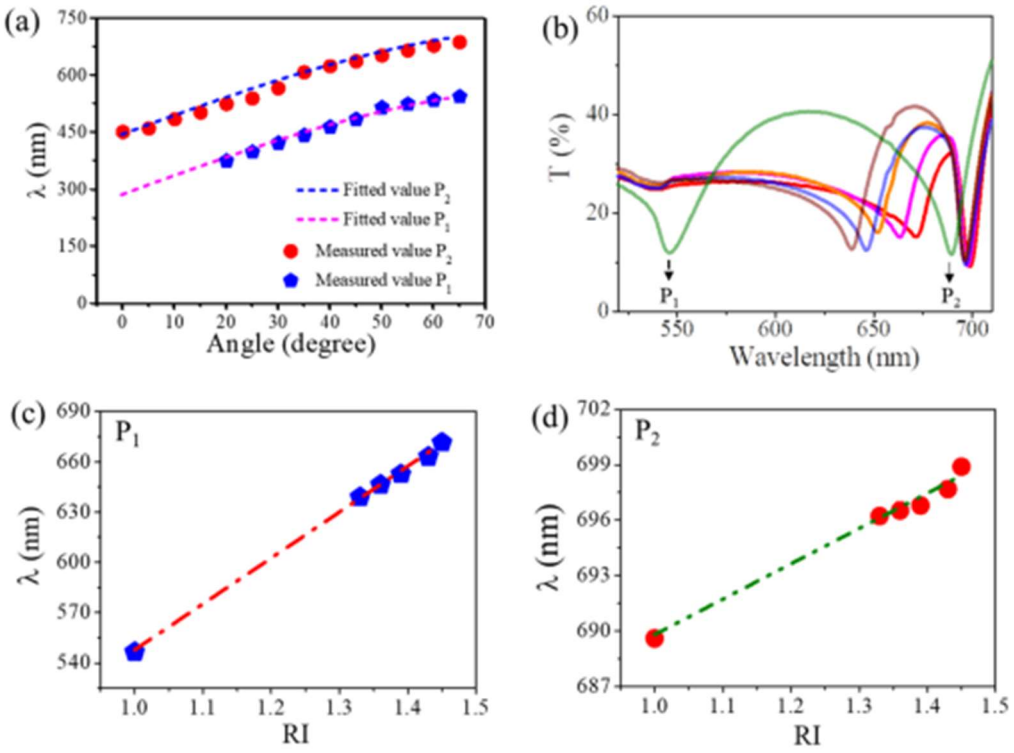

Figure 6.4: (a) Detected dispersion of the diffraction modes in Fig.6.3c (red dots and blue pentagons) and fit (magenta and blue dotted line) of the experimental data based on the RA eq. 6.1 and 6.2, respectively. (b) Optical transmission spectra of Au NS detected at $\theta = 65°$ (p-TM polarization of the incident light) in the presence of different dielectric media characterized by increasing RI from 1.0 (green line) to 1.33 (wine line), 1.36 (blue line), 1.39 (orange line), 1.43 (magenta line), and 1.45(red line). (c,d) Plot of the resonant wavelength of the optical features P1 and P2, respectively, detected at the incidence angle $\theta = 65°$ as a function of the RI of the dielectric medium. The RI sensitivity S_λ, corresponding to the slope of the fitted linear curve, corresponds to 275 and 19.5 nm/RIU, respectively.

We stress that such a high value of RI sensitivity is competitive with those obtained in the state-of-the art approaches, generally requiring complex optical detection schemes[169–171] (e.g. localized and high- resolution surface reflectivity measurements[172]) or nanofabrication techniques, which limit the active area of the device[173,174] (e.g. electron beam lithography). Few experiments can be found, which aim at RI sensing using 1D/2D NS gratings in the extinction configuration at normal incidence[167,175,176]. Among these examples, RI sensing is also demonstrated for a self-assembled film of gold bipyramids synthesized using a chemical route, with LSP resonance linewidths in the 100 nm range and comparable sensitivity[177]. Our RI sensing configuration, which exploits a simple extinction setup combined with an original tilted sample configuration, enables cost-effective and narrow-band RI sensing showing substantial advantages with respect to previously mentioned reports. Remarkably, we have, here, achieved competitive RI sensing performances with a sensor active area extending over macroscopic areas (cm^2 scale), thus enabling cost-effective integration of these flat-optics plasmonic templates in real-world biosensing devices. In perspective, by reducing the optical

beam diameters in the 50 µm range and the cell gap to the 100 µm range, the active volume of the sampled liquid could be easily reduced to sub-picoliter value area making possible multiplex microarray sensing.

In conclusion, this work demonstrates a cost-effective method able to combine large-area (cm^2 scale) fabrication of flat-optics nanosensors with a fast and compact optical detection scheme. We have shown high sensitivity of the flat-optics configuration to the dielectric environment by exploiting 1D plasmonic gratings, which extends homogeneously over large-area transparent templates. A cost-effective nanofabrication method based on LIL enables the nanofabrication of 1D gold NS gratings with a tunable shape and/or periodicity. By exploiting the potential of the large-area nanofabrication approach, an effective tuning of the dichroic plasmonic and flat-optics response can be achieved over a broadband spectral range, demonstrating resonant coupling between the polarization sensitive LSP and the RA at the air− and at the substrate− grating interface. Under this condition, narrowband Fano lineshapes enable homogenous sensitivity to the environmental RI enhanced up to 275 nm/RIU by exploiting an integrated microfluidic sensor. The detected RI sensitivity is competitive to state-of-the art sensors and, combined with the cost-effective nanofabrication and the simple optical scheme, is very promising in view of integration of this flat-optics platform into large-area microfluidic devices.

6.2 Flat-optics nanogratings on free-standing membranes

While LIL fabrication approach represents a cheap and versatile method, the application of LIL gratings to high resolution nanofluidic sensing requires tilted optical measurements which involve cumbersome setups and, together with the advantage of large area, carries an intrinsic limit in terms of sample volume required for a significant experimental output. A valid alternative can thus be the application of the free-standing chips mentioned in the previous chapters as nanofluidic platforms, where the transparent (500 µm side) window not only can be patterned with complete control over geometrical parameters using EBL, but also opens the possibility to achieve – for the right matching of aspect ratio and periodicity – the coupling of light into the free-standing membrane featuring waveguiding effects. The excitation of Guided Mode Anomalies (GMA) into these free-standing metasurfaces represents a very effective way to resonantly couple light to the membrane in view of sensing applications.

When high refractive index substrates are employed, efficient light-guiding can be achieved, and gratings can promote resonant electromagnetic confinement into the waveguide. Different schemes have been investigated so far, based both on plasmonic[178] and/or dielectric gratings[179], for launching waveguided modes which can be tuned across a broadband spectral range by properly engineering the metasurface (e.g. materials, antennas design). Both all-dielectric and hybrid plasmonic/dielectric gratings supporting Guided Mode Resonances (GMR) have been proposed and optimized for a broad range of applications, from diffractive elements to biosensors[180]. In particular, an hybrid scheme supporting both photonic and plasmonic modes has been recently proposed for biomolecules sensing[181].

Concerning GMR gratings, asymmetric light absorbers/reflectors have been fabricated on free-standing Si_3N_4 membranes in view of energy harvesting and wavelength multiplexing applications[182,183].

Thin and free-standing supports endowed with high refractive index represent a unique platform where flat-optics gratings can combine effective waveguiding properties with near field confinement at the interface, with crucial impact in optofluidics and biosensing. The possibility to design optically-active nanofluidic channels is intriguing since, on one side it opens the possibility to study interaction between light and fluid transport[184,185], while on the other it enables the development of compact free-standing nanosensors[186,187].

In our experiments, periodic plasmonic nanostripe arrays are fabricated on top of electron-transparent silicon nitride (Si_3N_4) membranes via high resolution electron beam lithography (EBL), achieving homogeneous patterned area extending over hundreds of square microns (Figure 6.5a, 6.5b).

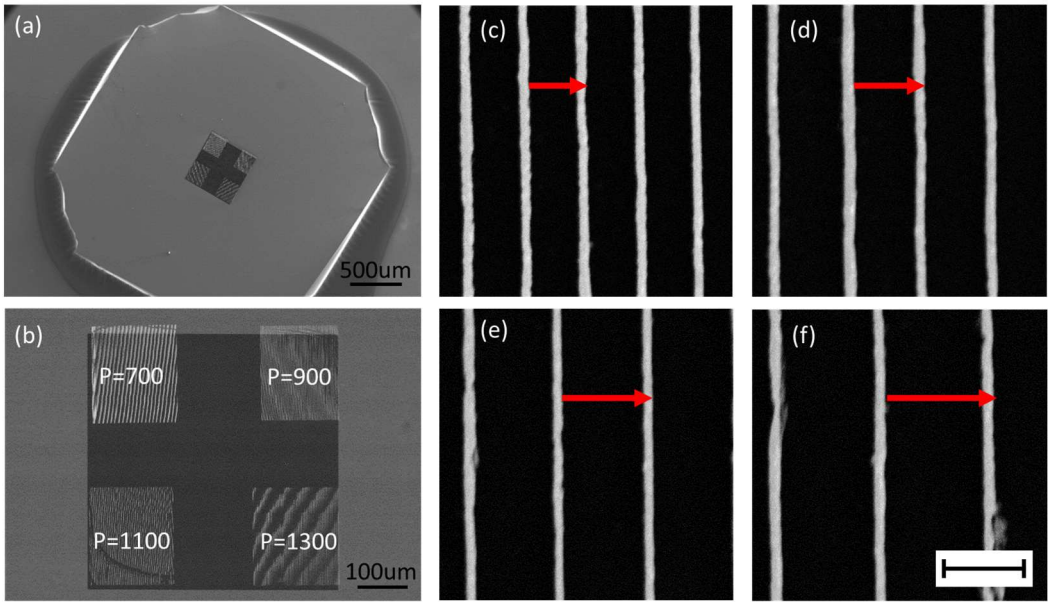

Figure 6.5: SEM images of the studied sample. (a) Low magnification image of the 3mm chip, with the square free-standing window visible in the middle; (b) detail of the free-standing area: four patterns with marked period have been fabricated without overlap. The apparent distortion of the patterns is simply a graphical artefact due to Moiré effect; (c-f) images of the nanostripes arrays with period respectively 700 nm, 900 nm, 1100 nm and 1300 nm. Magnification of the SEM images is the same (scale bar 1 µm).

The Scanning Electron Microscope (SEM) image of Figure 6.5b well highlights the presence of four patterns on the same substrate, which are characterized by different periodicity of the lattice, P, ranging from 700 nm to 1300 nm, thus enabling the fine tuning of the optical response of these free-standing gratings. SEM images shown in Figure 6.5c and Figure 6.5f, respectively corresponding to increasing periodicity of the pattern from $P = 700\ nm$ to P = 1300 nm, highlight the degree of order of the nanopatterns and the control on the periodicity and shape of the antennas. All the patterns are based on gold nanostripes characterized by

fixed aspect ratio w/h= 3 determined by nanostripes width w = 120 nm and thickness h = 40 nm. These morphological parameters have been engineered with the aim to tune the optical modes of the antennas within the Visible (VIS) and Near-Infrared (NIR) spectrum.

6.2.1 Optical properties of free-standing nanogratings

The optical response of these free-standing arrays has been investigated via optical micro-spectroscopy, using a custom modified optical microscope (see chapter 5.2 for details), operating in transmission configuration (Figure 6.6a) and fibre-coupled to a VIS-NIR spectrometer. A white light beam is shone from a halogen lamp through a polarizer and a condenser lens, finally illuminating the bottom surface of the sample at normal incidence (Figure 6.6a). A 100x magnification objective collects the optical intensity transmitted from a micro-spot (diameter ~20 µm).

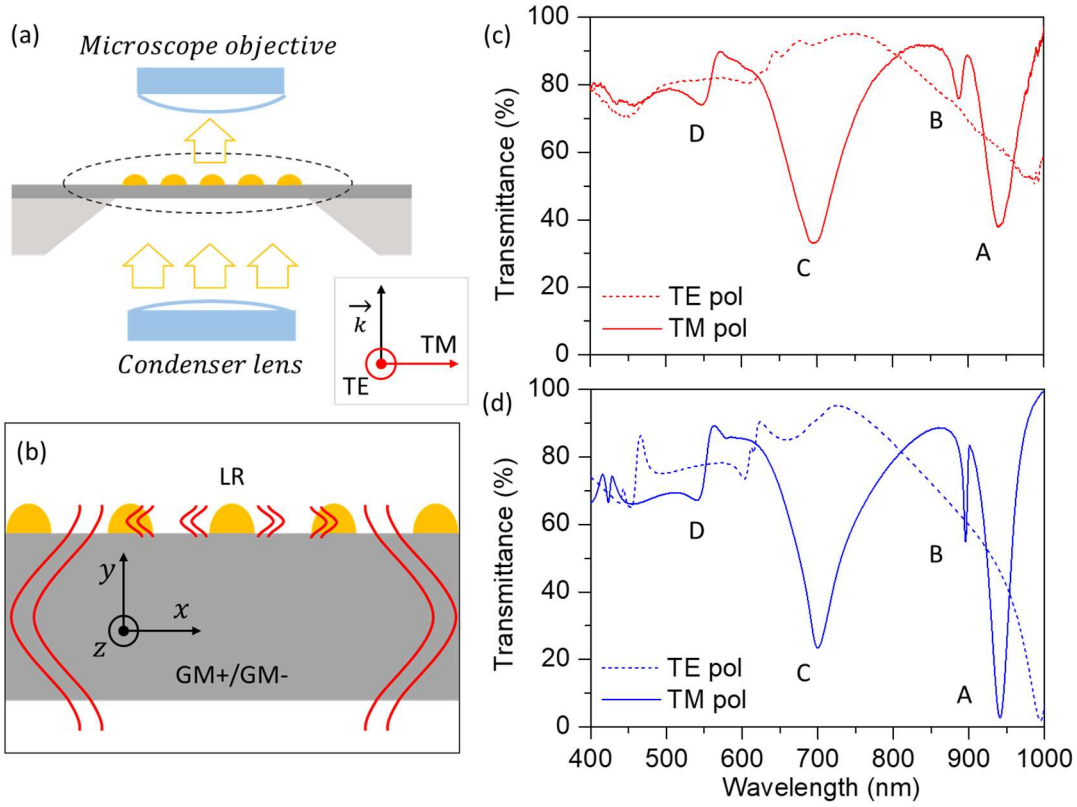

Figure 6.6: (a) Schematic representation of the optical setup, based on an optical microscope fibre-coupled with a spectrometer; (b) sketch of the photonic modes sustained by the nanoarrays: the plasmonic nanostripe gratings behave as plasmonic antennas supporting lattice resonances (LR) and launching guided modes in the high index substrate (GM+, GM-); (c,d) Experimental and simulated optical response of the P700 array, respectively. The transmission micro spectra were measured and calculated by sample excitation with polarized light, both perpendicular (TM- solid curves) and parallel (TE - dashed curves) to the nanostripes long axis.

Due to the order of these periodic arrays and to the subwavelength size of the Au nanostripes, different optical modes are expected to occur in the VIS and NIR spectral ranges.

Indeed, the Au nanostripes behave as plasmonic nanoantennas and, at the same time, the periodic grating may support Rayleigh Anomalies (RA). Under this condition the so-called Lattice Resonances (LR) confined at the surface (see sketch in Figure 6.6b) can be observed due to resonant interference between RA and plasmonic mode[56]. Additionally, guided modes (GM+/GM-) can be launched into the high index substrate, due to resonant interaction with the periodic nanograting (see sketch in Figure 6.6b).

In Figure 6.6c the normal incidence transmission micro spectra of the pattern P700 are shown, corresponding to two perpendicular polarizations of the excitation beam. The light is polarized either parallel (TE-pol, dashed curves) or perpendicular (TM-pol, solid curves) to the long axis of the nanostripes. A strong optical dichroism is detected in these anisotropic arrays. For TE polarization, a slight decrease of transmittance is observed for wavelengths below 500 nm, due to inter-band transitions in gold, in resonance with high order optical modes. Additional weak modes are observed at higher wavelengths. For TM polarization, we detect high-energy optical modes ($\lambda \sim$ 400-450 nm) that can be associated to the presence of the SiN waveguide beneath the pattern, and/or to the generation of high order guided modes[188]. At higher wavelengths, four sharp modes are detected within the VIS and NIR spectrum. The first minimum is visible at 540 nm (mode D in Figure 6.6c), a broader lattice resonance is detected at 700 nm and marked as mode C. Given the geometrical aspect ratio of the nanostripes, we indeed expect a localized plasmon resonance within this spectral range. This feature provides a good coupling efficiency between the grating and the photonics guided modes leading to possible plasmonic/photonic mode hybridization over a broadband range. Two further narrowband minima are visible in the NIR spectrum (mode B at 900 nm, mode A at 940 nm) corresponding to the first order guided modes. Experimental spectra have been confirmed by finite-difference time-domain (FDTD) calculations of finite structures (removing periodic boundary conditions), considering an incident Gaussian field of 10 μm beam waist. Numerical results depicted in Figure 6.6d are in remarkable agreement with the experimental data (Figure 6.6c). Due to the symmetry of the system, using finite size spots fulfilling normally incident plane wave approximation, one would expect the resonant excitation of left to right (LTR) or right to left (RTL) guided modes that are degenerate in frequency. Conversely, in our system we observe a peculiar double peak behaviour (modes A, B and modes C, D) that can be attributed to the transverse components of the wavevector with respect to the surface normal. Indeed, a plane wave expansion of a real focused beam contains also wavevectors components corresponding to nonzero incidence angles (θ). These components can couple to the guided modes according to the following equation:

[eq. 6.3]

$$\frac{2\pi}{\lambda} sin(\theta) + \frac{2\pi}{\Lambda} m = \pm \frac{2\pi}{\lambda} n_{eff}$$

where λ is the wavelength, Λ is the periodicity of the grating, the integer *m* is the diffraction order of the grating and the sign + (-) stands for the same (opposite) direction of propagation of the guided mode (of effective refractive index n_{eff}) with respect to the incident light. The (+) and (-) solutions of Eq. 6.3 respectively correspond to modes such as A (GM+) and B (GM-), and to all the higher order pairs.

Since for a symmetric normal incident Gaussian beam the amount of LTR and RTL coupled energy is the same, we are not able to distinguish the two contributions. To validate our hypothesis about the nature of the peaks we run simulations (in collaboration with Prof. Centini, La Sapienza University of Rome) calculating the field distribution of the four labelled modes. In the case of the lattice resonance, we expect the electromagnetic field to be confined at the nanoantenna's surface, while for pure guided modes we expect the typical single layer symmetric waveguide field distributions[189–191]. In Figure 6.7 we observe the spatial distribution of both magnetic (H/H_0 - first two columns on the left) and electric (E/E_0 - right columns) field. The system supports a combination of different leaky waveguided modes with symmetric optical field distribution perpendicularly to the guide (y axis). The calculated distribution of the magnetic field of mode A, B and D (Figure 6.7a, 6.7e, 6.7m) suggests a symmetric behaviour. Conversely, in the case of mode C, calculations show an asymmetric magnetic field distribution (Figure 6.7i), with strong localization in proximity of the nanoantenna grating attributed to the resonant interference with the broader lattice resonance supported by plasmonic nanoantennas.

Additionally, strong interference fringes are observed along the waveguide (x axis), arising from the superposition of LTR and RTL counter-propagating guided modes. While A, B and D (Figure 6.7a, 6.7e, 6.7m) are based on the unperturbed fundamental TM0 guided mode of the Si_3N_4 slab, mode C (Figure 6.7i) displays the typical central node of the TM1 mode.

A deeper analysis of the zoomed magnetic and electric field distributions across the slab section reveals high symmetry for modes B (Figure 6.7f, 6.7g) and D (Figure 6.7n, 6.7o), typical of dielectric waveguided modes. On the other hand, in the case of mode A (Figure 6.7a, 6.7b) and C (Figure 6.7i, 6.7j) the optical field distributions are asymmetric and mainly confined on the grating side. In particular, mode C with plasmonic character shows electric field strongly confined within a few nanometres at the surface (Figure 6.7k), while mode A shows broader distribution out of the substrate (Figure 6.7c). It is worth noticing that all the waveguided modes detuned with respect to the lattice resonance are characterized by electric field (Ey/E0) strongly amplified within a gap extended 100 - 150 nm out of the guide. These wide hot-spots are very promising in view of nanofluidic and/or molecular sensing applications.

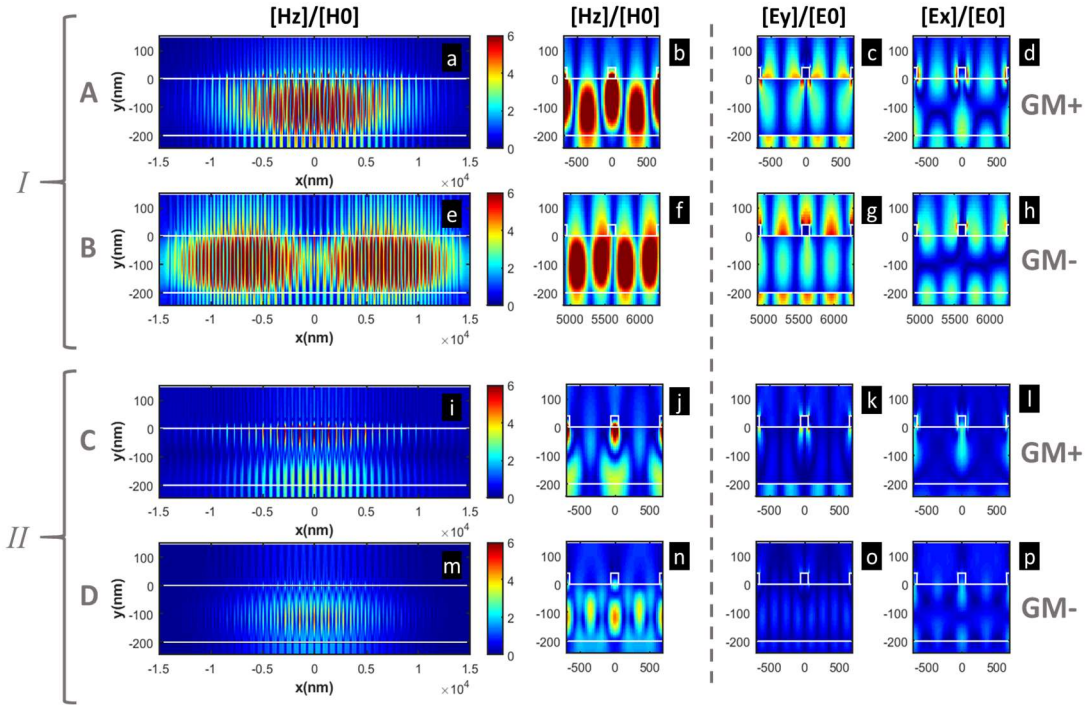

Figure 6.7: Calculated field maps of the four detected modes, represented along the cross section of the membrane with the nanostripes on the upper surface and the axis aligned as depicted in Figure 6.6b. (a,e,i,m) Extended [Hz]/[Ho] maps of modes A, B, C, D divided in first (I) and second (II) order modes; (b,f,j,n) detail of the [Hz]/[Ho] maps, two periods of the grating are visible on the upper surface; (c,g,k,o) and (d,h,l,p) detail maps of the electric field components along the y and x axis. GM+ and GM- distinction refers to higher wavelength (A, C) and lower wavelength (B, D) modes among the peak pairs, as resulting from Eq. 6.3.

6.2.2 Tuning optical modes in free-standing nanogratings

In order to tune the waveguided modes supported by the nanogratings over a broadband spectrum, we engineer nanopatterns formed by nanostripes of identical cross section and different periodicity (Figure 6.5c, 6.5d, 6.5e, 6.5f). Figure 6.8 compares the detected micro spectra with calculated responses of four different samples with increasing periodicity. Figure panels are sorted by increasing the pattern periodicity from top (P = 700 nm - Figure 6.8a) to bottom (P = 1300 nm - Figure 6.8j), while the side panels (Figure 6.8b, 6.8e, 6.8h, 6.8k) show the corresponding simulated response. As previously noticed, every pattern is characterized by interband transition in Au below 500 nm wavelength, and by multiple absorption minima in the red-shifted part of the spectrum. For TM polarization, a broadband mode is clearly detected at about 700 nm wavelength, corresponding to the plasmonic lattice resonance. The spectral position of this mode is kept constant in the different arrays provided the fixed aspect ratio of the nanostripes. However, the broadband plasmonic mode is resonantly coupled to guided modes at detuned frequencies depending on the grating periodicity. Conversely, the guided modes excited in sample P700 at 900 nm and 940 nm respectively (Figure 6.8a), display a different behaviour: a gradual red-shift is detected as the grating periodicity increases. In particular, for P = 900 nm, the modes red-shift to about 1050

nm and 1090 nm as shown in the VIS-NIR experimental spectra of Figure 6.8d and labelled as first order (*I*) in the simulations of Figure 6.8e and Figure 6.8f.

Figures 6.8c, 6.8f, 6.8i, 6.8l correspond to simulated spectra within the NIR range (1000-1500 nm) and allow us to follow the spectral position of the first order modes for the higher periodicity samples outside the experimentally observable range. The first order guided modes detected for P700 gradually red-shift as periodicity increases, in parallel the second and third order excitations are detected in sample P900 and P1100 (Figure 6.8d and 6.8g), and the fourth order emerges in sample P1300 (Figure 6.8j).

Observing the stitched full range simulated curves (the two columns on the right in Figure 6.8), up to four pairs of modes can be recognized for the patterns with larger periodicity. Array P1300 exhibits its first order guided modes (*I*) at 1400 nm, its second order (*II*) at 850-900 nm, the third (*III*) at 650-700 nm, and the fourth (*IV*) at 550-600 nm.

The second order modes in samples P700 and P900 – or the third order in P1100 and P1300 – are broader with respect to the other modes arising from the same array. When the modes are interacting with the plasmon, indeed, they show an increased intensity of the absorption peaks and relative broadening of the resonance due to the plasmonic dampening. This consideration assumes critical importance in the context of the sensing applications. Indeed, the spectral width of the mode is a key parameter in view of refractive index sensing, limiting the resolution of the spectroscopic detection and the sensitivity of the technique.

Within the set of samples described in this work, the tuning capabilities allowed us to achieve different coupling conditions between the narrowband waveguided modes and the plasmonic resonance. This is highlighted by the different shapes of the resonance detected at about 700 nm wavelength in all the samples and confirmed by corresponding calculation of both spectra and near-field distribution. Among the observed responses, P1100 displays high intensity and narrowband second order waveguided modes excitation at about 800 nm wavelength (Figure 6.8g). As confirmed by calculation of the spectra (Figure 6.8h), the second order waveguided modes are here detuned from the plasmonic resonance and show a dominant waveguided behaviour. In particular, we would like to exploit its characteristic electric field amplification – localized within a broader liquid volume – for refractive index sensing.

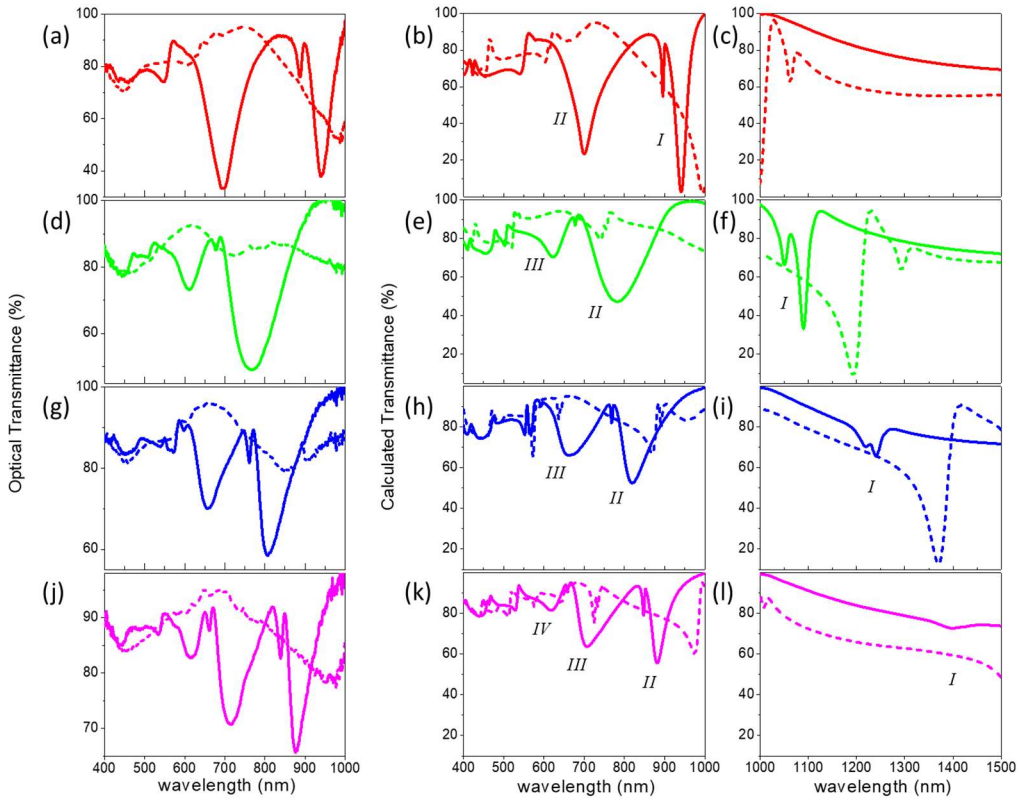

Figure 6.8: Spectral shift of the modes obtained by variation of the grating periodicity, P = (a) 700, (d) 900, (g) 1100, (j) 1300 nm. (a,d,g,j) experimental spectra of the gratings; (b,e,h,k) calculated spectra of the nanostripes in the experimentally observed spectral range; (c,f,l,l) calculated extended-range spectra in the Near IR. The order of the guided modes is labelled with letters in the simulated spectra.

6.2.3 Free-standing nanogratings sensors

To test the performance of this flat-optics system, we devised a proof-of-concept experiment based on the free-standing plasmonic/photonic templates operating as nanofluidic refractive index sensors. To get quantitative information, the chip has been mounted on a transparent glass support as sketched in Figure 6.9a. The fluidic microchannel enables controlled confinement of sub-picoliter volumes of liquid in the active area. This configuration enables direct in-situ optical detection of transmission micro-spectra under normal incidence illumination (as shown in Figure 6.6a). Different liquids with known refractive index (water, iso-propanol, PMMA/ethyl-lactate solution) have been dosed in contact with the nanopatterned side of the membrane, monitoring the spectral shift of the optical modes.

Figure 6.9b compares the VIS-NIR transmittance micro-spectra detected when the active area of P1100 nanograting samples different dielectric environments: air (black curve), water (red curve), iso-propanol (IPA) (green curve) and a PMMA-ethyl-lactate solution (blue curve). A gradual redshift of all the optical modes is detected as the refractive index increases from air- (n=1) to PMMA - environment (n=1.42). To evaluate the spectral sensitivity of this template we selected the narrowband second-order guided modes (see Figure 6.8h), resonant in air at 770 nm (mode B) and 810 nm (mode A) and characterized by optimal

bandwidth. A red-shift of more than 50 nm has been detected for both the targeted peaks as *n* increases from 1 to 1.42. In parallel, the resonant frequency of these modes linearly depends on the refractive index, as highlighted by the plot of Figure 6.9c, and further confirmed by data fit. The latter allows the evaluation of the refractive index sensitivity ($\frac{\Delta\lambda}{\Delta n}$), corresponding to the slope of the curve and reading 180 nm/RIU for mode B (red arrow in Figure 6.9b), and 110 nm /RIU for mode A (blue arrow in Figure 6.9b).

The corresponding simulated spectra of this nanosensor (Figure 6.9d), well matches with the experimental data (Figure 6.9b), further confirming the good optical sensitivity of this platform based on guided photonic modes. In particular, the mode B (as seen for P700 in Figure 6.7g), is characterized by minimal bandwidth and by strong near-field confinement extending about 100-150 nm at the external interface of the metasurface. This latter figure is particularly promising in view of more complex nanofluidic sensing platforms enabling detection of weak molecular signals (e.g. SERS). In perspective, nanogratings with different aspect ratio and/or periodicity can be fabricated to evaluate different coupling conditions between the guided modes and the plasmonic response. In this respect the simulated spectra of Figure 6.9d suggest that the spectral width of the waveguided mode could be reduced to 5 nm in an optimized sample, with possible improvement of the refractive index sensing performances[192].

Another interesting pathway to increase the sensing capability of the device involves reduction of the minimum sampled volume[185]. By simply designing a fluidic channel with drastically reduced gap in the ten-micrometre range, the sensed volume can be downscaled to the picolitre scale. As a lower limit at the molecular scale one can consider examples of nanofluidic applications in which the nanograting itself behaves as a nanochannels grating, supporting a 2D material flake that acting as a ceiling of the nanofluidic system.

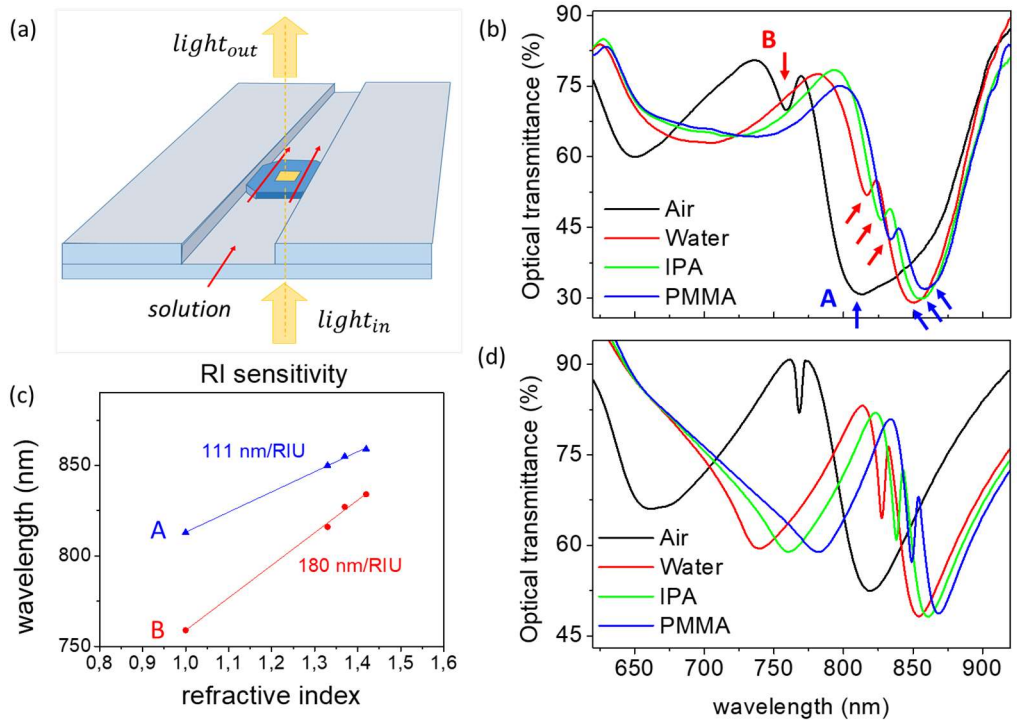

Figure 6.9: Testing of the device sensing capability. (a) sketch of the measure configuration: the active area is highlighted in yellow, the red arrows indicate the flow of tested solution inside the canal; (b) in-situ spectra of the sample, liquids from top to bottom with increasing refractive index; (c) plotted spectral position of the peaks A and B in air (n=1), water (n=1.33), IPA (n=1.37) and PMMA solution (n=1.42), with estimated Refractive Index sensitivity obtained fitting the spectral shifts (nm/RIU); (d) simulation of the spectral shift with the attributed refractive indices.

In conclusion, flat optics nanosensor templates based on plasmonic gratings have been fabricated via high resolution electron beam lithography at the surface of free-standing silicon nitride (Si_3N_4) membranes. These engineered templates are able to host both a broadband plasmonic lattice resonance and different narrowband optical modes launched by the nanograting into the waveguide. A qualitative and semi-quantitative agreement has been achieved between measured optical micro spectra and simulations, demonstrating the capability to tune narrowband waveguided modes over a wide VIS-NIR spectrum by simply tailoring the periodicity of the lattice. The optimal bandwidth of these photonic modes, as low as 12 nm, combined with their strong near-field confinement at the external interface, enable the development of a hybrid photonic/plasmonic free-standing nanofluidic device. A proof-of-concept refractive index sensing experiment, at the sub-picoliter scale, showed a good refractive index sensitivity of 180 nm/RIU, for this free-standing platform, enabled by the narrowband waveguided mode (mode B), in optimal agreement with simulations. The latter, suggest a further improvement of the refractive index sensitivity in nanoarrays where bandwidth as low as 5 nm can be achieved. The high sensitivity provided by waveguided modes thus suggests these free-standing flat-optics platforms as optimal candidates for label-free biosensing into nanofluidic systems, diagnostics and environmental detection.

Appendix: Photon-harvesting with flat-optics nanogratings

Additional photonics applications of LIL nanogratings can be investigated by transfer of the polymeric nanopattern to a dielectric substrate. Under this condition photon harvesting functionalities can be obtained with a strong potential in photonics and photovoltaics. In this activity, we optimized the nanofabrication, and we studied the optical response of functionalized transparent windows for photon harvesting in thin organic photovoltaic cells. This activity led to a publication within an international research collaboration[193].

In recent years, organic photovoltaics (OPVs) have emerged as a promising candidate owing to their potential merit of low-cost energy conversion[194] and optional mechanical flexibility[195,196]. It opens up a range of novel and unconventional applications, e.g., integrating smart building components[197,198], products, and electronic devices. Despite the substantial progress in the last years[199], the power conversion efficiency of thin-film OPVs is still lower than their inorganic counterparts, and device performance always toggles between sufficient light absorption and good charge carrier extraction. Good light absorption would require a micrometer-scale thick active layer, restricting the collection of minority carriers[200]. On the other hand, a thin layer of the organic absorber is preferable to efficiently collect the photo-generated carriers, and beneficial against photon-induced degradation of the organic absorber. However, this limits the photon-absorption efficiency, which in turn reduces the overall efficiency of solar cells. A considerable portion of the incoming light is lost due to the reflection from the electrodes as well as due to incomplete absorption by the semi-transparent nature of the organic solar cells.

To suppress light reflection losses, various light management strategies have been proposed so far, like e.g. the addition of anti-reflective thin-film coating. Anti-reflective layers however act over a limited wavelength range and suffer from delamination issues which hinder mechanical stability on the long term[201,202]. The use of metallic nanostructures supporting localized plasmon resonances has been extensively studied in order to exploit the resonant light scattering amplification and/or the near-field enhancement[203,204], although the efficiency of these strategies is limited by ohmic losses.

In a complementary approach, anti-reflection and light trapping functionalities can be achieved by introducing subwavelength dielectric nanostructures on the transparent window which supports the active OPV layer[205,206]. A substantial increase of the photon absorption in thin-film photovoltaics has been recently demonstrated by functionalizing transparent or semiconductor substrates with large-scale self-organized nanopatterns based on anisotropic high-aspect ratio nanostructures[207–209]. The periodically textured surfaces endowed with subwavelength structures (SWSs) can reduce the reflection and/or increase light scattering and significantly increase the light coupled to the thin film device. High-aspect ratio SWSs fetch gradual changes in refractive index from the value of air to that of the substrate, mimicking the moth-eye effect leading anti-reflective functionality in the broadband spectral range[210,211]. In a complementary way, dielectric nanostructures with a lateral size comparable to or larger than the incident wavelength behave as Mie resonators,

strongly promote photon absorption, and thus enhance the short-circuit current (J_{SC}) in the thin film PV device.

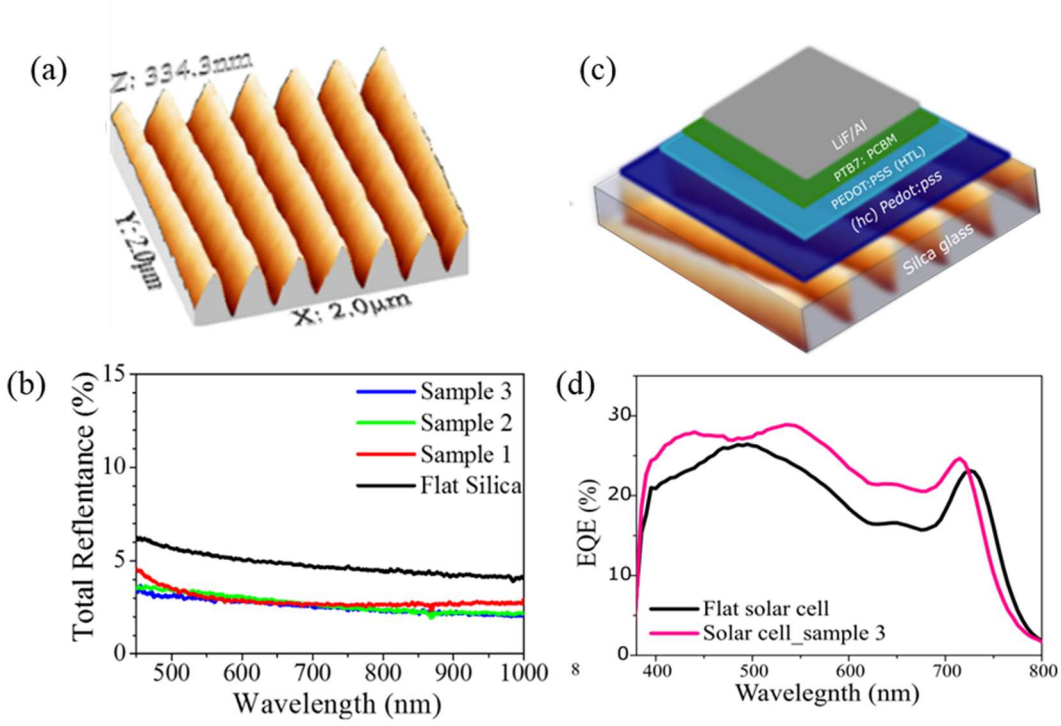

Figure A.1: (a) Topography 3D model, based on AFM images, showing the high homogeneity of the obtained anti-reflection nanostructures (model area = 2x2 µm²); (b) Total reflectance of the pristine substrate (black curve) compared with the one of the structured samples, measured inside an integrating sphere; (c) sketch of the OPV multi-stack cell, with LiF/Al layer on top of the active PTB7:PCBM film, PEDOT:PSS conductive contact and the anti-reflection silica window; (d) External Quantum Efficiency (EQE) of the OPV cell, compared with the EQE of an equivalent, non-functionalized cell. Adapted from[193].

Here, we demonstrated the capability to improve the photoconversion efficiency in thin-film OPV devices via large scale surface nanopatterning of the transparent window, promoting broadband light trapping into the active thin layer. We investigate periodically surface-textured substrates such as one dimensional (1-D) periodic gratings of different pitch (P) and groove height (H), to explore anti-reflection and Mie scattering effects for photon harvesting in organic thin film devices. A cost-effective approach based on laser interference lithography (LIL), combined with reactive ion etching, provides homogeneous nanofabrication of 1D nanogratings over macroscopic areas (cm^2) at the surface of transparent silica substrates (Figure A.1a), and enables controlled tailoring of the nanostructures shape and periodicity. These templates are conformally coated with a thin organic absorber layer (PTB7: PCBM), investigating their characteristic optical response via transmission and reflection optical spectroscopy, to identify the optimum light trapping condition. A suppression of the optical reflection, as high as 4%, has been detected over a broadband Visible and Near-Infrared spectral range (see Figure A.1b), thanks to an optimized

nanograting morphology (height 280 nm, period 300 nm). The nanopatterned thin film device hosted on this engineered template finally showed an amplified photoconversion figure with a 14% increase of the short-circuit current with respect to the reference flat device (Figure A.1d). These results demonstrate the potential of the large-scale nanogratings for broadband photon harvesting and conversion in thin film organic devices.

Conclusion and outlook

The search for new methods enabling efficient collection of particulate matter and multifactorial analysis in terms of size distribution, elemental composition, and structural identification represents a key-aspect of current efforts in environmental science.

In this thesis a significant part of the effort has been devoted to the problem of collection and concentration of airborne particulate matter on a miniaturised custom chip. For this purpose, I applied original nanofabrication approaches derived from nanotechnology to build a special Si_3N_4 sieve, capable of trapping the airborne micro- and nano-particles on the active region of custom modified free standing TEM membranes. In addition to this, by fabrication of nanophotonic structures on the active surface of chip concentrators, I studied the possibility to achieve co-localised and spatially resolved detection of submicrometric airborne particles, with high resolution and sensitivity. The results demonstrate that with the new prototype it is possible to investigate not only the concentration, size, and shape of collected particles, but also their chemical composition (via EDX spectroscopy) and molecular structure (via Raman spectroscopy).

In the first part of the thesis, I discussed the significant effort in developing original nanofabrication methods for the functionalization of substrates, introducing the large-area fabrication of periodic gratings (by Laser Interference Lithography) and the development of an Electron Beam Lithography (EBL) module installed in the hosting laboratory right before the beginning of my PhD. The EBL know-how acquired during the doctorate turned out to be crucial for the fabrication of functionalized Si_3N_4 membranes and the collection of submicrometric particles.

In Chapter 4 I have demonstrated the possibility of applying the nanofabricated collection chips in realistic environmental conditions. For this purpose, I designed and built a portable collection prototype featuring a custom chip holder, where the free-standing membranes can be mounted to enable their safe application in standard collection setups and subsequent mounting in vacuum chambers or spectroscopy instruments. Then I set up a sampling experiment in order to check the performance of the chip with respect to standard techniques for PM sampling. Aerosols composed of micro- and nanoparticles (roughly PM2.5) have been generated and their size-distribution has been controlled and studied thanks to the analysis of samples collected, in parallel, on the fabricated membranes and on standard collection references. Thus, I could define a transfer-function between the collection efficiency of standard techniques and the one obtained with the chip.

In Chapter 5 I have demonstrated that the microfabricated silicon nitride chip allows the identification of individual nanoparticles immobilised on the membrane. Thanks to the definition of a common coordinate system on the surface of the free-standing membranes, it is possible to address specific particles of interest in co-localized spectroscopic experiments performed in different instruments such as electron microscopy, x-ray energy dispersive spectroscopy and micro-Raman spectroscopy. Thanks to the reduced nanometer thickness of the free-standing membrane, the background signal of the X-ray fluorescence

spectrometer is minimised making possible identification and analysis of size, shape, composition down to the nanometer level. Remarkably the functionalization of the perforated free-standing substrates with self-organised plasmonic nanoantennas boosts dramatically the sensitivity of the Raman spectroscopy. By tailoring the plasmonic resonance in the range of the Raman laser pump the signal of a single molecular layer of Methylene Blue molecules adsorbed on the surface of the functionalized membrane is boosted by more than 4 orders of magnitude with respect to a reference flat gold film. Further optimization efforts are placed to enhance the spectroscopic signal from particles collected on the miniaturised devices, opening the possibility of high-sensitivity detection to the limit of single molecule sensing.

In Chapter 6, I presented a different approach for the plasmonic functionalization of the active surface of the sensors, aiming at monitoring variations of the refractive index in the environment surrounding the active surface. The concept here is to adopt a simple optical extinction measurement configuration employing a cheap solid-state spectrometer coupled to a transparent substrate. Nanofabrication of ordered plasmonic gratings with tailored periodic geometry gives rise to narrowband modes resulting from the coupling of localised plasmonic resonances and lattice modes (also described in the context of Rayleigh anomalies) which exhibit a marked sensitivity to the refractive index of the external environment. In my thesis I explored two different configurations, one based on large area nanofabrication on bulk glass substrates (via Laser Interference Lithography), the other based on EBL nanofabrication on the miniaturised free-standing membranes. In both cases I demonstrated the possibility to employ them in a liquid environment, achieving a strong sensitivity to the variation of the external refractive index. In the case of the free-standing membranes, additionally, I demonstrated the coupling of light into the thin substrate and the generation of guided modes featuring strong EM field localization.

There remain several questions to be answered, such as the possibility of modifying the geometry of pores in the fabricated membranes or developing a versatile connection system between membrane and environment to select in a simple way the upper cut-off size of the particles collected on the miniaturised filters. A possible development of the sampling platform which requires further work is the detection of nanometer scale particulate and biologically relevant target molecules dispersed in airborne liquid droplets and aerosols. The latter problem has become particularly relevant in recent times due to the COVID pandemic. To conclude, we can state that the designed substrates and miniaturised sampling platform represent a promising solution for the co-localized study of collected particles, capable of multifactorial and high-resolution analysis in a compact and versatile approach, where the combination of nanophotonics and nanotechnology paves the road toward the development of compact devices for portable and personal PM monitoring.

List of oral and poster communications presented by the PhD candidate at workshops and conferences

Personal oral communications:

- Manzato, G., Giordano, M. C., Centini, M., Buatier de Mongeot, F., *"Nanofluidic sensing with nanostripe gratings on a free-standing SiN waveguide"*, **EOSAM 2021** European Optical Society Annual Meeting, Rome (IT), September 13-17, 2021, TOM9 S05, Optics at Nanoscale (ONS): Sensing.

- Manzato, G., Giordano, M. C., Centini, M., Buatier de Mongeot, F., *"Microfabricated SiN membrane applied as a free-standing waveguide for refractive index sensing"*, **MNE 2021** 47th International Conference on Micro and Nano Engineering, flagship event of the international Micro and Nano Engineering society (iMNEs), Turin (IT), September 20-23, 2021, Session C5: Technologies for micro and nano Photonics II.

Personal poster communications:

- Manzato, G., et al., *"Large area fabrication of metal-dielectric metasurfaces via laser interference lithography"*, **VISPEC 2019**, International conference on emerging trends in vibrational spectroscopy, Brescia (IT), September 9-13, 2019.

- Manzato, G., Giordano, M. C., Centini, M., Buatier de Mongeot, F. *"Flat-optics nanostripe gratings for nanofluidic sensing"*, **POM21** (Photonics Online Meetup 2021), International online meeting on photonics, January 13-14, 2021.

Other papers

- B. Siri, E. Celasco, L. Ferrari Barusso, F. Buatier de Mongeot, P. Manfrinetti, G. Manzato, A. Provino, F. Gatti, *Impact of Annealing on TC and Structure of Titanium Thin Films, in IEEE Transactions on Applied Superconductivity*, vol. 31, no. 5, pp. 1-4, Aug. 2021, Art no. 7500304, doi: 10.1109/TASC.2021.3071997.

Aknowledgements / Ringraziamenti

At the end of this adventure, I wish to thank all the people met on the route toward the doctorate completion, inside and outside the University:

My dear colleagues from the “LabNano” Group, both the elders Marina, Carlo, Matteo, Roberto and Debasree, and the young Matteo, Giulio and Giorgio (and his laptop), because surviving a PhD would be much harder without them (and always remember… riprarno).

Above all I want to thank my supervisor, Francesco Buatier, who was able to lead me in the ways of science and research, sharing hours of zoom calls with dogs barking below my desk and patiently pulling me out from the “bozzolo” each and every time.

I want to thank the group PM_TEN for the fruitful collaboration, my co-supervisor Paolo Brotto for all the shared knowledge in the field, Dario Massabò for the supervision of my prototype (often tragical) experiments, and of course Lorenzo and Silvia for the support.

For the RIE etching facility, I have to thank Flavio Gatti and the most-friendly-and-collaborative Beatrice Siri, who gave birth with remarkable precision to the nanosieves.

For the micro-Raman facility, I wish to thank Marco Scambelluri, other example of notable patience in respect to my prototype experiments.

Special thanks to Ennio Vigo, the work-shop operator who never said “no” to one of my tiny, thin, fragile, asymmetric, and definitely-too-many chip holders, enabling the realization of all the core components of the collection prototype.

Francesco Bisio, for sharing his tales during pre-pandemic lunches.

Marco Smerieri, Letizia Savio and Giovanni Carraro, for sharing my first research experiences in the bachelor thesis and always finding time for a word.

Silvano Tosi, for all the discussions and counsels (and, of course, the sushi).

The great PhD lunch-group “*Pame na Fame*”, for the magically good vibes in the middle of workdays, and especially Marzia who was there since it all started.

The Plasmokémon(s): bad batch, all materials scientists, better not knowing them.

Fopp.a.Tu.Bi. friends, best combination of role-play games, wine, food and laughs.

My parents for the constant certainty of a support.

My brothers, because you don’t choose your siblings, but if had the chance it would be them.

Zia Paola, for sharing the wisdom of a fully spent life.

And Alessandra, for being lovely at my side in the good and the bad times.

List of References

(1) Hinds, W. C. *Aerosol Technology: Properties, Behavior, and Measurement of Airborne Particles*, 2nd ed.; Wiley: New York, 1999.

(2) UNION, P. Directive 2008/50/EC of the European Parliament and of the Council of 21 May 2008 on Ambient Air Quality and Cleaner Air for Europe. *Off. J. Eur. Union* **2008**.

(3) European Environmental Agency Report - Air Quality in Europe 2021 - ISBN 978-92-9480-403-7 - ISSN 1977-8449 - Doi: 10.2800/549289.

(4) Seinfeld, J. H.; Pandis, S. N. *Atmospheric Chemistry and Physics: From Air Pollution to Climate Change*, Third edition.; John Wiley & Sons: Hoboken, New Jersey, 2016.

(5) IPCC. Climate Change 2013:The Physical Science Basis. Working Group I Contribution to the Fifth Assessment Report of the Intergovernmental Panel on Climate Change. Technical Report, Intergovernmental Panel on Climate Change, 2013.

(6) Mannshardt, E.; Sucic, K.; Jiao, W.; Dominici, F.; Frey, H. C.; Reich, B.; Fuentes, M. Comparing Exposure Metrics for the Effects of Fine Particulate Matter on Emergency Hospital Admissions. *J. Expo. Sci. Environ. Epidemiol.* **2013**, *23* (6), 627–636. https://doi.org/10.1038/jes.2013.39.

(7) Wang, Y.; Kloog, I.; Coull, B. A.; Kosheleva, A.; Zanobetti, A.; Schwartz, J. D. Estimating Causal Effects of Long-Term PM $_{2.5}$ Exposure on Mortality in New Jersey. *Environ. Health Perspect.* **2016**, *124* (8), 1182–1188. https://doi.org/10.1289/ehp.1409671.

(8) Burnett, R.; Chen, H.; Szyszkowicz, M.; Fann, N.; Hubbell, B.; Pope, C. A.; Apte, J. S.; Brauer, M.; Cohen, A.; Weichenthal, S.; Coggins, J.; Di, Q.; Brunekreef, B.; Frostad, J.; Lim, S. S.; Kan, H.; Walker, K. D.; Thurston, G. D.; Hayes, R. B.; Lim, C. C.; Turner, M. C.; Jerrett, M.; Krewski, D.; Gapstur, S. M.; Diver, W. R.; Ostro, B.; Goldberg, D.; Crouse, D. L.; Martin, R. V.; Peters, P.; Pinault, L.; Tjepkema, M.; van Donkelaar, A.; Villeneuve, P. J.; Miller, A. B.; Yin, P.; Zhou, M.; Wang, L.; Janssen, N. A. H.; Marra, M.; Atkinson, R. W.; Tsang, H.; Quoc Thach, T.; Cannon, J. B.; Allen, R. T.; Hart, J. E.; Laden, F.; Cesaroni, G.; Forastiere, F.; Weinmayr, G.; Jaensch, A.; Nagel, G.; Concin, H.; Spadaro, J. V. Global Estimates of Mortality Associated with Long-Term Exposure to Outdoor Fine Particulate Matter. *Proc. Natl. Acad. Sci.* **2018**, *115* (38), 9592–9597. https://doi.org/10.1073/pnas.1803222115.

(9) Dockery, D. W.; Pope, C. A.; Xu, X.; Spengler, J. D.; Ware, J. H.; Fay, M. E.; Ferris, B. G.; Speizer, F. E. An Association between Air Pollution and Mortality in Six U.S. Cities. *N. Engl. J. Med.* **1993**, *329* (24), 1753–1759. https://doi.org/10.1056/NEJM199312093292401.

(10) Amaral, S.; de Carvalho, J.; Costa, M.; Pinheiro, C. An Overview of Particulate Matter Measurement Instruments. *Atmosphere* **2015**, *6* (9), 1327–1345. https://doi.org/10.3390/atmos6091327.

(11) CEN. EN 12341:2014 - Ambient Air. Standard Gravimetric Measurement Method for the Determination of the PM10 or PM2,5 Mass Concentration of Suspended Particulate Matter. Technical Report, Centre European de Normalisation, 2014.

(12) Giechaskiel, B.; Maricq, M.; Ntziachristos, L.; Dardiotis, C.; Wang, X.; Axmann, H.; Bergmann, A.; Schindler, W. Review of Motor Vehicle Particulate Emissions Sampling and Measurement: From Smoke and Filter Mass to Particle Number. *J. Aerosol Sci.* **2014**, *67*, 48–86. https://doi.org/10.1016/j.jaerosci.2013.09.003.

(13) Bohren, C. F.; Huffman, D. R. *Absorption and Scattering of Light by Small Particles*; 2008.

(14) Nüesch, M. F.; Ivanović, M. T.; Claude, J.-B.; Nettels, D.; Best, R. B.; Wenger, J.; Schuler, B. Single-Molecule Detection of Ultrafast Biomolecular Dynamics with

Nanophotonics. *J. Am. Chem. Soc.* **2022**, *144* (1), 52–56. https://doi.org/10.1021/jacs.1c09387.

(15) Acuna, G.; Grohmann, D.; Tinnefeld, P. Enhancing Single-Molecule Fluorescence with Nanophotonics. *FEBS Lett.* **2014**, *588* (19), 3547–3552. https://doi.org/10.1016/j.febslet.2014.06.016.

(16) Mivelle, M.; Van Zanten, Thomas. S.; Manzo, C.; Garcia-Parajo, M. F. Nanophotonic Approaches for Nanoscale Imaging and Single-Molecule Detection at Ultrahigh Concentrations: Nanophotonic Approaches for Biology. *Microsc. Res. Tech.* **2014**, *77* (7), 537–545. https://doi.org/10.1002/jemt.22369.

(17) Crouch, G. M.; Han, D.; Bohn, P. W. Zero-Mode Waveguide Nanophotonic Structures for Single Molecule Characterization. *J. Phys. Appl. Phys.* **2018**, *51* (19), 193001. https://doi.org/10.1088/1361-6463/aab8be.

(18) Mock, J. J.; Barbic, M.; Smith, D. R.; Schultz, D. A.; Schultz, S. Shape Effects in Plasmon Resonance of Individual Colloidal Silver Nanoparticles. *J. Chem. Phys.* **2002**, *116* (15), 6755–6759. https://doi.org/10.1063/1.1462610.

(19) Sharma, B.; Frontiera, R. R.; Henry, A.-I.; Ringe, E.; Van Duyne, R. P. SERS: Materials, Applications, and the Future. *Mater. Today* **2012**, *15* (1–2), 16–25. https://doi.org/10.1016/S1369-7021(12)70017-2.

(20) Portela, A.; Calvo-Lozano, O.; Estevez, M.-C.; Medina Escuela, A.; Lechuga, L. M. Optical Nanogap Antennas as Plasmonic Biosensors for the Detection of MiRNA Biomarkers. *J. Mater. Chem. B* **2020**, *8* (19), 4310–4317. https://doi.org/10.1039/D0TB00307G.

(21) Lim, D.-K.; Jeon, K.-S.; Kim, H. M.; Nam, J.-M.; Suh, Y. D. Nanogap-Engineerable Raman-Active Nanodumbbells for Single-Molecule Detection. *Nat. Mater.* **2010**, *9* (1), 60–67. https://doi.org/10.1038/nmat2596.

(22) Nam, J.-M.; Oh, J.-W.; Lee, H.; Suh, Y. D. Plasmonic Nanogap-Enhanced Raman Scattering with Nanoparticles. *Acc. Chem. Res.* **2016**, *49* (12), 2746–2755. https://doi.org/10.1021/acs.accounts.6b00409.

(23) Kim, J.; Sim, K.; Cha, S.; Oh, J.; Nam, J. Single-Particle Analysis on Plasmonic Nanogap Systems for Quantitative SERS. *J. Raman Spectrosc.* **2021**, *52* (2), 375–385. https://doi.org/10.1002/jrs.6030.

(24) Cilwa, K. E.; McCormack, M.; Lew, M.; Robitaille, C.; Corwin, L.; Malone, M. A.; Coe, J. V. Scatter-Free IR Absorption Spectra of Individual, 3–5 Mm, Airborne Dust Particles Using Plasmonic Metal Microarrays: A Library of 63 Spectra. *J. Phys. Chem. C* **2011**, *115* (34), 16910–16919. https://doi.org/10.1021/jp205383h.

(25) Malone, M. A.; McCormack, M.; Coe, J. V. Single Airborne Dust Particles Using Plasmonic Metal Films with Hole Arrays. *J. Phys. Chem. Lett.* **2012**, *3* (6), 720–724. https://doi.org/10.1021/jz300057z.

(26) Qiu, G.; Yue, Y.; Tang, J.; Zhao, Y.-B.; Wang, J. Total Bioaerosol Detection by a Succinimidyl-Ester-Functionalized Plasmonic Biosensor To Reveal Different Characteristics at Three Locations in Switzerland. *Environ. Sci. Technol.* **2020**, *54* (3), 1353–1362. https://doi.org/10.1021/acs.est.9b05184.

(27) Zeng, Y.; Hu, R.; Wang, L.; Gu, D.; He, J.; Wu, S.-Y.; Ho, H.-P.; Li, X.; Qu, J.; Gao, B. Z.; Shao, Y. Recent Advances in Surface Plasmon Resonance Imaging: Detection Speed, Sensitivity, and Portability. *Nanophotonics* **2017**, *6* (5), 1017–1030. https://doi.org/10.1515/nanoph-2017-0022.

(28) Xing, J.; Shao, L.; Zhang, W.; Peng, J.; Wang, W.; Shuai, S.; Hu, M.; Zhang, D. Morphology and Size of the Particles Emitted from a Gasoline-Direct-Injection-Engine Vehicle and Their Ageing in an Environmental Chamber. *Atmospheric Chem. Phys.* **2020**, *20* (5), 2781–2794. https://doi.org/10.5194/acp-20-2781-2020.

(29) Acher, O.; Nguyên, T.-L.; Podzorov, A.; Leroy, M.; Carles, P.-A.; Legendre, S. An Efficient Solution for Correlative Microscopy and Co-Localized Observations Based on Multiscale Multimodal Machine-Readable NanoGPS Tags. *Meas. Sci. Technol.* **2021**, *32* (4), 045402. https://doi.org/10.1088/1361-6501/abce39.

(30) George Sarau, Lasse Kling, Barbara E. Oßmann, Ann-Katrin Unger, Frank Vogler, and Silke H. Christiansen, "Correlative Microscopy and Spectroscopy Workflow for Microplastics," Appl. Spectrosc. 74, 1155-1160 (2020).

(31) Xu, Q.; Zhang, W.; Dong, C.; Sreeprasad, T. S.; Xia, Z. Biomimetic Self-Cleaning Surfaces: Synthesis, Mechanism and Applications. *J. R. Soc. Interface* **2016**, *13* (122), 20160300. https://doi.org/10.1098/rsif.2016.0300.

(32) Wilson, S. J.; Hutley, M. C. The Optical Properties of "Moth Eye" Antireflection Surfaces. *Opt. Acta Int. J. Opt.* **1982**, *29* (7), 993–1009. https://doi.org/10.1080/713820946.

(33) Sun, C.-H.; Jiang, P.; Jiang, B. Broadband Moth-Eye Antireflection Coatings on Silicon. *Appl. Phys. Lett.* **2008**, *92* (6), 061112. https://doi.org/10.1063/1.2870080.

(34) Maier, S. A. *Plasmonics: Fundamentals and Applications*; Springer: New York, 2007.

(35) Yu, N.; Capasso, F. Flat Optics with Designer Metasurfaces. *Nat. Mater.* **2014**, *13* (2), 139–150. https://doi.org/10.1038/nmat3839.

(36) Yu, H.; Peng, Y.; Yang, Y.; Li, Z.-Y. Plasmon-Enhanced Light–Matter Interactions and Applications. *Npj Comput. Mater.* **2019**, *5* (1), 45. https://doi.org/10.1038/s41524-019-0184-1.

(37) Yu, T.; Wei, Q. Plasmonic Molecular Assays: Recent Advances and Applications for Mobile Health. *Nano Res.* **2018**, *11* (10), 5439–5473. https://doi.org/10.1007/s12274-018-2094-9.

(38) Kristensen, A.; Yang, J. K. W.; Bozhevolnyi, S. I.; Link, S.; Nordlander, P.; Halas, N. J.; Mortensen, N. A. Plasmonic Colour Generation. *Nat. Rev. Mater.* **2017**, *2* (1), 16088. https://doi.org/10.1038/natrevmats.2016.88.

(39) Wang, J.; Lin, W.; Cao, E.; Xu, X.; Liang, W.; Zhang, X. Surface Plasmon Resonance Sensors on Raman and Fluorescence Spectroscopy. *Sensors* **2017**, *17* (12), 2719. https://doi.org/10.3390/s17122719.

(40) Kalachyova, Y.; Mares, D.; Lyutakov, O.; Kostejn, M.; Lapcak, L.; Švorčík, V. Surface Plasmon Polaritons on Silver Gratings for Optimal SERS Response. *J. Phys. Chem. C* **2015**, *119* (17), 9506–9512. https://doi.org/10.1021/acs.jpcc.5b01793.

(41) Neff, H.; Oliveira, L. C.; Rodrigures, E. P.; Thirstrup, C.; Lima, A. M. N. Enhanced Directed Radiative Surface Plasmon Emission from Periodically Corrugated Noble Metal Films. *Plasmonics* **2018**, *13* (6), 2021–2027. https://doi.org/10.1007/s11468-018-0718-2.

(42) Gillibert, R.; Sarkar, M.; Bryche, J.-F.; Yasukuni, R.; Moreau, J.; Besbes, M.; Barbillon, G.; Bartenlian, B.; Canva, M.; Chapelle, M. L. de la. Directional Surface Enhanced Raman Scattering on Gold Nano-Gratings. *Nanotechnology* **2016**, *27* (11), 115202. https://doi.org/10.1088/0957-4484/27/11/115202.

(43) *Handbook of Enhanced Spectroscopy*; Gucciardi, P. G., Lamy de la Chapelle, M., Lidgi-Guigui, N., Eds.; Pan Stanford Publishing: Singapore, 2016.

(44) Lee, J.; Crampton, K. T.; Tallarida, N.; Apkarian, V. A. Visualizing Vibrational Normal Modes of a Single Molecule with Atomically Confined Light. *Nature* **2019**, *568* (7750), 78–82. https://doi.org/10.1038/s41586-019-1059-9.

(45) Zhang, R.; Zhang, Y.; Dong, Z. C.; Jiang, S.; Zhang, C.; Chen, L. G.; Zhang, L.; Liao, Y.; Aizpurua, J.; Luo, Y.; Yang, J. L.; Hou, J. G. Chemical Mapping of a Single Molecule by Plasmon-Enhanced Raman Scattering. *Nature* **2013**, *498* (7452), 82–86. https://doi.org/10.1038/nature12151.

(46) Tallarida, N.; Rios, L.; Apkarian, V. A.; Lee, J. Isomerization of One Molecule Observed through Tip-Enhanced Raman Spectroscopy. *Nano Lett.* **2015**, *15* (10), 6386–6394. https://doi.org/10.1021/acs.nanolett.5b01543.

(47) Domke, K. F.; Zhang, D.; Pettinger, B. Tip-Enhanced Raman Spectra of Picomole Quantities of DNA Nucleobases at Au(111). *J. Am. Chem. Soc.* **2007**, *129* (21), 6708–6709. https://doi.org/10.1021/ja071107q.

(48) Treffer, R.; Böhme, R.; Deckert-Gaudig, T.; Lau, K.; Tiede, S.; Lin, X.; Deckert, V. Advances in TERS (Tip-Enhanced Raman Scattering) for Biochemical Applications. *Biochem. Soc. Trans.* **2012**, *40* (4), 609–614. https://doi.org/10.1042/BST20120033.

(49) Sheng, S.; Wu, J.; Cong, X.; Li, W.; Gou, J.; Zhong, Q.; Cheng, P.; Tan, P.; Chen, L.; Wu, K. Vibrational Properties of a Monolayer Silicene Sheet Studied by Tip-Enhanced Raman Spectroscopy. *Phys. Rev. Lett.* **2017**, *119* (19), 196803. https://doi.org/10.1103/PhysRevLett.119.196803.

(50) Smolsky, J. M.; Krasnoslobodtsev, A. V. Nanoscopic Imaging of Oxidized Graphene Monolayer Using Tip-Enhanced Raman Scattering. *Nano Res.* **2018**, *11* (12), 6346–6359. https://doi.org/10.1007/s12274-018-2158-x.

(51) Bohren, C. F.; Huffman, D. R. *Absorption and Scattering of Light by Small Particles*, 1st ed.; Wiley, 1998. https://doi.org/10.1002/9783527618156.

(52) Muskens, O.; Christofilos, D.; Fatti, N. D.; Vallée, F. Optical Response of a Single Noble Metal Nanoparticle. *J. Opt. Pure Appl. Opt.* **2006**, *8* (4), S264–S272. https://doi.org/10.1088/1464-4258/8/4/S28.

(53) Maier, S. A.; Kik, P. G.; Atwater, H. A. Observation of Coupled Plasmon-Polariton Modes in Au Nanoparticle Chain Waveguides of Different Lengths: Estimation of Waveguide Loss. *Appl. Phys. Lett.* **2002**, *81* (9), 1714–1716. https://doi.org/10.1063/1.1503870.

(54) Maystre, D. I Rigorous Vector Theories of Diffraction Gratings. In *Progress in Optics*; Elsevier, 1984; Vol. 21, pp 1–67. https://doi.org/10.1016/S0079-6638(08)70121-5.

(55) Antonakakis, Tryfon & Baida, Fadi & Belkhir, Abderrahmane & Cherednichenko, Kirill & Cooper, Shane & Craster, Richard & Demésy, Guillaume & Desanto, John & Granet, G. & Gralak, Boris & Guenneau, Sébastien & Maystre, Daniel & Nicolet, André & Stout, Brian & Zolla, Frédéric & Vial, Benjamin & Popov, Evgeni. (2012). Gratings: Theory and Numeric Applications.

(56) Giannini, V.; Vecchi, G.; Gómez Rivas, J. Lighting Up Multipolar Surface Plasmon Polaritons by Collective Resonances in Arrays of Nanoantennas. *Phys. Rev. Lett.* **2010**, *105* (26), 266801. https://doi.org/10.1103/PhysRevLett.105.266801.

(57) Bhatnagar, M.; Giordano, M. C.; Mennucci, C.; Chowdhury, D.; Mazzanti, A.; Della Valle, G.; Martella, C.; Tummala, P.; Lamperti, A.; Molle, A.; Buatier de Mongeot, F. Ultra-Broadband Photon Harvesting in Large-Area Few-Layer MoS_2 Nanostripe Gratings. *Nanoscale* **2020**, *12* (48), 24385–24393. https://doi.org/10.1039/D0NR06744J.

(58) Bhatnagar, M.; Gardella, M.; Giordano, M. C.; Chowdhury, D.; Mennucci, C.; Mazzanti, A.; Valle, G. D.; Martella, C.; Tummala, P.; Lamperti, A.; Molle, A.; Buatier de Mongeot, F. Broadband and Tunable Light Harvesting in Nanorippled MoS_2 Ultrathin Films. *ACS Appl. Mater. Interfaces* **2021**, *13* (11), 13508–13516. https://doi.org/10.1021/acsami.0c20387.

(59) Martella, C.; Mennucci, C.; Giordano, M. C.; Buatier de Mongeot, F.; Delli Veneri, P.; Mercaldo, L. V.; Usatii, I. Broadband Light Trapping in Nanopatterned Thin Film Amorphous Silicon Solar Cells. In *2014 Third Mediterranean Photonics Conference*; IEEE: Trani, Italy, 2014; pp 1–2. https://doi.org/10.1109/MePhoCo.2014.6866455.

(60) D'Andrea, C.; Fazio, B.; Gucciardi, P. G.; Giordano, M. C.; Martella, C.; Chiappe, D.; Toma, A.; Buatier de Mongeot, F.; Tantussi, F.; Vasanthakumar, P.; Fuso, F.; Allegrini,

M. SERS Enhancement and Field Confinement in Nanosensors Based on Self-Organized Gold Nanowires Produced by Ion-Beam Sputtering. *J. Phys. Chem. C* **2014**, *118* (16), 8571–8580. https://doi.org/10.1021/jp5007236.

(61) Giordano, M. C.; Tzschoppe, M.; Barelli, M.; Vogt, J.; Huck, C.; Canepa, F.; Pucci, A.; Buatier de Mongeot, F. Self-Organized Nanorod Arrays for Large-Area Surface-Enhanced Infrared Absorption. *ACS Appl. Mater. Interfaces* **2020**, *12* (9), 11155–11162. https://doi.org/10.1021/acsami.9b19719.

(62) Giordano, M. C.; Foti, A.; Messina, E.; Gucciardi, P. G.; Comoretto, D.; Buatier de Mongeot, F. SERS Amplification from Self-Organized Arrays of Plasmonic Nanocrescents. *ACS Appl. Mater. Interfaces* **2016**, *8* (10), 6629–6638. https://doi.org/10.1021/acsami.5b11843.

(63) Wang, D.-S.; Chew, H.; Kerker, M. Enhanced Raman Scattering at the Surface (SERS) of a Spherical Particle. *Appl. Opt.* **1980**, *19* (14), 2256. https://doi.org/10.1364/AO.19.002256.

(64) Salameh, D.; Detournay, A.; Pey, J.; Pérez, N.; Liguori, F.; Saraga, D.; Bove, M. C.; Brotto, P.; Cassola, F.; Massabò, D.; Latella, A.; Pillon, S.; Formenton, G.; Patti, S.; Armengaud, A.; Piga, D.; Jaffrezo, J. L.; Bartzis, J.; Tolis, E.; Prati, P.; Querol, X.; Wortham, H.; Marchand, N. PM2.5 Chemical Composition in Five European Mediterranean Cities: A 1-Year Study. *Atmospheric Res.* **2015**, *155*, 102–117. https://doi.org/10.1016/j.atmosres.2014.12.001.

(65) Sandrini, S.; Fuzzi, S.; Piazzalunga, A.; Prati, P.; Bonasoni, P.; Cavalli, F.; Bove, M. C.; Calvello, M.; Cappelletti, D.; Colombi, C.; Contini, D.; de Gennaro, G.; Di Gilio, A.; Fermo, P.; Ferrero, L.; Gianelle, V.; Giugliano, M.; Ielpo, P.; Lonati, G.; Marinoni, A.; Massabò, D.; Molteni, U.; Moroni, B.; Pavese, G.; Perrino, C.; Perrone, M. G.; Perrone, M. R.; Putaud, J.-P.; Sargolini, T.; Vecchi, R.; Gilardoni, S. Spatial and Seasonal Variability of Carbonaceous Aerosol across Italy. *Atmos. Environ.* **2014**, *99*, 587–598. https://doi.org/10.1016/j.atmosenv.2014.10.032.

(66) Scerri, M. M.; Kandler, K.; Weinbruch, S.; Yubero, E.; Galindo, N.; Prati, P.; Caponi, L.; Massabò, D. Estimation of the Contributions of the Sources Driving PM2.5 Levels in a Central Mediterranean Coastal Town. *Chemosphere* **2018**, *211*, 465–481. https://doi.org/10.1016/j.chemosphere.2018.07.104.

(67) Ogura, I.; Kotake, M.; Sakurai, H.; Honda, K. Surface-Collection Efficiency of Nuclepore Filters for Nanoparticles. *Aerosol Sci. Technol.* **2016**, *50* (8), 846–856. https://doi.org/10.1080/02786826.2016.1200007.

(68) Xiang, M.; Morgeneyer, M.; Philippe, F.; Manokaran, M.; Bressot, C. Comparative Review of Efficiency Analysis for Airborne Solid Submicrometer Particle Sampling by Nuclepore Filters. *Chem. Eng. Res. Des.* **2020**, *164*, 338–351. https://doi.org/10.1016/j.cherd.2020.10.009.

(69) Sheehan, P. E.; Whitman, L. J. Detection Limits for Nanoscale Biosensors. *Nano Lett.* **2005**, *5* (4), 803–807. https://doi.org/10.1021/nl050298x.

(70) Nair, P. R.; Alam, M. A. Performance Limits of Nanobiosensors. *Appl. Phys. Lett.* **2006**, *88* (23), 233120. https://doi.org/10.1063/1.2211310.

(71) Lassiter, J. B.; Aizpurua, J.; Hernandez, L. I.; Brandl, D. W.; Romero, I.; Lal, S.; Hafner, J. H.; Nordlander, P.; Halas, N. J. Close Encounters between Two Nanoshells. *Nano Lett.* **2008**, *8* (4), 1212–1218. https://doi.org/10.1021/nl080271o.

(72) Eftekhari, F.; Escobedo, C.; Ferreira, J.; Duan, X.; Girotto, E. M.; Brolo, A. G.; Gordon, R.; Sinton, D. Nanoholes As Nanochannels: Flow-through Plasmonic Sensing. *Anal. Chem.* **2009**, *81* (11), 4308–4311. https://doi.org/10.1021/ac900221y.

(73) Jason-Moller, L.; Murphy, M.; Bruno, J. Overview of Biacore Systems and Their Applications. *Curr. Protoc. Protein Sci.* **2006**, *45* (1). https://doi.org/10.1002/0471140864.ps1913s45.

(74) De Angelis, F.; Gentile, F.; Mecarini, F.; Das, G.; Moretti, M.; Candeloro, P.; Coluccio, M. L.; Cojoc, G.; Accardo, A.; Liberale, C.; Zaccaria, R. P.; Perozziello, G.; Tirinato, L.; Toma, A.; Cuda, G.; Cingolani, R.; Di Fabrizio, E. Breaking the Diffusion Limit with Super-Hydrophobic Delivery of Molecules to Plasmonic Nanofocusing SERS Structures. *Nat. Photonics* **2011**, *5* (11), 682–687. https://doi.org/10.1038/nphoton.2011.222.

(75) Sun, M.; Luo, C.; Xu, L.; Ji, H.; Ouyang, Q.; Yu, D.; Chen, Y. Artificial Lotus Leaf by Nanocasting. *Langmuir* **2005**, *21* (19), 8978–8981. https://doi.org/10.1021/la050316q.

(76) Janel, S.; Werkmeister, E.; Bongiovanni, A.; Lafont, F.; Barois, N. CLAFEM. In *Methods in Cell Biology*; Elsevier, 2017; Vol. 140, pp 165–185. https://doi.org/10.1016/bs.mcb.2017.03.010.

(77) Odermatt, P. D.; Shivanandan, A.; Deschout, H.; Jankele, R.; Nievergelt, A. P.; Feletti, L.; Davidson, M. W.; Radenovic, A.; Fantner, G. E. High-Resolution Correlative Microscopy: Bridging the Gap between Single Molecule Localization Microscopy and Atomic Force Microscopy. *Nano Lett.* **2015**, *15* (8), 4896–4904. https://doi.org/10.1021/acs.nanolett.5b00572.

(78) Fantner, G.; Lafont, F. Correlative Microscopy Using Scanning Probe Microscopes. In *Correlative Imaging*; Verkade, P., Collinson, L., Eds.; Wiley, 2019; pp 99–118. https://doi.org/10.1002/9781119086420.ch6.

(79) Peddie, C. J.; Domart, M.-C.; Snetkov, X.; O'Toole, P.; Larijani, B.; Way, M.; Cox, S.; Collinson, L. M. Correlative Super-Resolution Fluorescence and Electron Microscopy Using Conventional Fluorescent Proteins in Vacuo. *J. Struct. Biol.* **2017**, *199* (2), 120–131. https://doi.org/10.1016/j.jsb.2017.05.013.

(80) Sarau G, Yarbakht M, Ossmann B, Kling L, Aste J, Vollnhals F, Mueller-Deile J, Schiffer M and Christiansen S H 2020 Context Microscopy and Fingerprinting Spectroscopy of Micro- and Nanoplastics and Their Effects on Human Kidney Cells Using NanoGPS and Particle Finder Readout E54 23 (Https://Static.Horiba. Com/Fileadmin/Horiba/Company/About_HORIBA/ Readout/R54E/R54E_05_023.Pdf).

(81) Paul-Gilloteaux, P.; Heiligenstein, X.; Belle, M.; Domart, M.-C.; Larijani, B.; Collinson, L.; Raposo, G.; Salamero, J. EC-CLEM: Flexible Multidimensional Registration Software for Correlative Microscopies. *Nat. Methods* **2017**, *14* (2), 102–103. https://doi.org/10.1038/nmeth.4170.

(82) Jiruše, J.; Haničinec, M.; Havelka, M.; Hollricher, O.; Ibach, W.; Spizig, P. Integrating Focused Ion Beam–Scanning Electron Microscope with Confocal Raman Microscope into a Single Instrument. *J. Vac. Sci. Technol. B Nanotechnol. Microelectron. Mater. Process. Meas. Phenom.* **2014**, *32* (6), 06FC03. https://doi.org/10.1116/1.4897502.

(83) Bruker BioMaterials Workstation BioMAT Https://Www.Bruker.Com/En/Products-and-Solutions/Microscopes/Bioafm/Bioafm-Accessories/Biomaterials-Workstation-Biomat.Html.

(84) Norcada Micro-Porous Membranes on TEM Grids Https://Www.Norcada.Com/Products/Porous-Membranes/.

(85) PELCO® Holey Silicon Nitride Support Film for TEM Https://Www.Tedpella.Com/Grids_html/Silicon-Nitride-Holey.Aspx.

(86) Dong, Z.; Bosman, M.; Zhu, D.; Goh, X. M.; Yang, J. K. W. Fabrication of Suspended Metal–Dielectric–Metal Plasmonic Nanostructures. *Nanotechnology* **2014**, *25* (13), 135303. https://doi.org/10.1088/0957-4484/25/13/135303.

(87) Hatab, N. A.; Hsueh, C.-H.; Gaddis, A. L.; Retterer, S. T.; Li, J.-H.; Eres, G.; Zhang, Z.; Gu, B. Free-Standing Optical Gold Bowtie Nanoantenna with Variable Gap Size for

Enhanced Raman Spectroscopy. *Nano Lett.* **2010**, *10* (12), 4952–4955. https://doi.org/10.1021/nl102963g.

(88) Brostrøm, A.; Kling, K. I.; Koponen, I. K.; Hougaard, K. S.; Kandler, K.; Mølhave, K. Improving the Foundation for Particulate Matter Risk Assessment by Individual Nanoparticle Statistics from Electron Microscopy Analysis. *Sci. Rep.* **2019**, *9* (1), 8093. https://doi.org/10.1038/s41598-019-44495-7.

(89) R'mili, B.; Dutouquet, C.; Sirven, J. B.; Aguerre-Chariol, O.; Frejafon, E. Analysis of Particle Release Using LIBS (Laser-Induced Breakdown Spectroscopy) and TEM (Transmission Electron Microscopy) Samplers When Handling CNT (Carbon Nanotube) Powders. *J. Nanoparticle Res.* **2011**, *13* (2), 563–577. https://doi.org/10.1007/s11051-010-0050-z.

(90) R'mili, B.; Le Bihan, O. L. C.; Dutouquet, C.; Aguerre-Charriol, O.; Frejafon, E. Particle Sampling by TEM Grid Filtration. *Aerosol Sci. Technol.* **2013**, *47* (7), 767–775. https://doi.org/10.1080/02786826.2013.789478.

(91) Lyyränen, J.; Backman, U.; Tapper, U.; Auvinen, A.; Jokiniemi, J. A Size Selective Nanoparticle Collection Device Based on Diffusion and Thermophoresis. *J. Phys. Conf. Ser.* **2009**, *170*, 012011. https://doi.org/10.1088/1742-6596/170/1/012011.

(92) Ogura, I.; Hashimoto, N.; Kotake, M.; Sakurai, H.; Kishimoto, A.; Honda, K. Aerosol Particle Collection Efficiency of Holey Carbon Film-Coated TEM Grids. *Aerosol Sci. Technol.* **2014**, *48* (7), 758–767. https://doi.org/10.1080/02786826.2014.924614.

(93) Fierz, M.; Kaegi, R.; Burtscher, H. Theoretical and Experimental Evaluation of a Portable Electrostatic TEM Sampler. *Aerosol Sci. Technol.* **2007**, *41* (5), 520–528. https://doi.org/10.1080/02786820701253327.

(94) Ileri, N. Fabrication of Functional Silicon-Based Nanoporous Membranes. *J. MicroNanolithography MEMS MOEMS* **2012**, *11* (1), 013012. https://doi.org/10.1117/1.JMM.11.1.013012.

(95) Achar, B. H. V.; Sengupta, S.; Bhattacharya, E. Fabrication of Ultrathin Silicon Nanoporous Membranes and Their Application in Filtering Industrially Important Biomolecules. *IEEE Trans. Nanotechnol.* **2013**, *12* (4), 583–588. https://doi.org/10.1109/TNANO.2013.2262100.

(96) Gel, M.; Kandasamy, S.; Cartledge, K.; Haylock, D. Fabrication of Micro Pore Arrays in Free Standing COC Membranes and Their Application for in Vitro Barrier Tissue Models. In *2013 IEEE 26th International Conference on Micro Electro Mechanical Systems (MEMS)*; IEEE: Taipei, Taiwan, 2013; pp 895–898. https://doi.org/10.1109/MEMSYS.2013.6474388.

(97) Montagne, F.; Blondiaux, N.; Bojko, A.; Pugin, R. Molecular Transport through Nanoporous Silicon Nitride Membranes Produced from Self-Assembling Block Copolymers. *Nanoscale* **2012**, *4* (19), 5880. https://doi.org/10.1039/c2nr31498c.

(98) Ileri, N.; Faller, R.; Palazoglu, A.; Létant, S. E.; Tringe, J. W.; Stroeve, P. Molecular Transport of Proteins through Nanoporous Membranes Fabricated by Interferometric Lithography. *Phys Chem Chem Phys* **2013**, *15* (3), 965–971. https://doi.org/10.1039/C2CP43400H.

(99) EMS Grids Square Mesh Https://Www.Emsdiasum.Com/Microscopy/Products/Grids/Gilder.Aspx.

(100) Adiga, S. P.; Jin, C.; Curtiss, L. A.; Monteiro-Riviere, N. A.; Narayan, R. J. Nanoporous Membranes for Medical and Biological Applications. *Wiley Interdiscip. Rev. Nanomed. Nanobiotechnol.* **2009**, *1* (5), 568–581.

(101) Han, J.; Fu, J.; Schoch, R. B. Molecular Sieving Using Nanofilters: Past, Present and Future. *Lab. Chip* **2008**, *8* (1), 23–33.

(102) Dekker, C. Solid-State Nanopores. *Nat. Nanotechnol.* **2007**, *2* (4), 209–215. https://doi.org/10.1038/nnano.2007.27.

(103) Heyderman, L. J.; Ketterer, B.; Bächle, D.; Glaus, F.; Haas, B.; Schift, H.; Vogelsang, K.; Gobrecht, J.; Tiefenauer, L.; Dubochet, O. High Volume Fabrication of Customised Nanopore Membrane Chips. *Microelectron. Eng.* **2003**, *67*, 208–213.

(104) Zhang, X.; Zhu, Z.; Sun, C.; Zhu, F.; Luo, Z.; Yan, J.; Mao, B. Colloidal Lithography-Based Fabrication of Suspended Nanoporous Silicon Nitride Membranes. *Microchim. Acta* **2009**, *167* (1), 135–140.

(105) *Comprehensive Nanoscience and Nanotechnology*, 2. Auflage-.; Andrews, D. L., Lipson, R. H., Nann, T., Eds.; Academic Press: Amsterdam Boston Heidelberg, 2019.

(106) Vogel, N.; Retsch, M.; Fustin, C.-A.; del Campo, A.; Jonas, U. Advances in Colloidal Assembly: The Design of Structure and Hierarchy in Two and Three Dimensions. *Chem. Rev.* **2015**, *115* (13), 6265–6311. https://doi.org/10.1021/cr400081d.

(107) Chuo, Y.; Landrock, C.; Omrane, B.; Hohertz, D.; Grayli, S. V.; Kavanagh, K.; Kaminska, B. Rapid Fabrication of Nano-Structured Quartz Stamps. *Nanotechnology* **2013**, *24* (5), 055304. https://doi.org/10.1088/0957-4484/24/5/055304.

(108) *Nanofabrication*; Stepanova, M., Dew, S., Eds.; Springer Vienna: Vienna, 2012. https://doi.org/10.1007/978-3-7091-0424-8.

(109) Raith GmbH, Dortmund, Www.Raith.Com.

(110) Vistec Electron Beam GmbH, Jena, Www.Vistec-Semi.Com.

(111) Jeol Electron Beam Lithography, Tokyo, Www.Jeol.Com/PRODUCTS/SemiconductorEQuipment/ElectronBeamLithography/Tabid/99/Default.Aspx.

(112) Chang, T. H. P. Proximity Effect in Electron-beam Lithography. *J. Vac. Sci. Technol.* **1975**, *12* (6), 1271–1275. https://doi.org/10.1116/1.568515.

(113) Owen, G. Methods for Proximity Effect Correction in Electron Lithography. *J. Vac. Sci. Technol. B Microelectron. Nanometer Struct.* **1990**, *8* (6), 1889. https://doi.org/10.1116/1.585179.

(114) Zhang, J.; Fouad, M.; Yavuz, M.; Cui, B. Charging Effect Reduction in Electron Beam Lithography with NA Beam Current. *Microelectron. Eng.* **2011**, *88* (8), 2196–2199. https://doi.org/10.1016/j.mee.2010.12.103.

(115) Tanaka, T.; Morigami, M.; Oizumi, H.; Soga, T.; Ogawa, T.; Murai, F. Prevention of Resist Pattern Collapse by Resist Heating during Rinsing. *J. Electrochem. Soc.* **1994**, *141* (12), L169–L171. https://doi.org/10.1149/1.2059382.

(116) Mohammad, M. A.; Fito, T.; Chen, J.; Buswell, S.; Aktary, M.; Stepanova, M.; Dew, S. K. Systematic Study of the Interdependence of Exposure and Development Conditions and Kinetic Modelling for Optimizing Low-Energy Electron Beam Nanolithography. *Microelectron. Eng.* **2010**, *87* (5–8), 1104–1107.

(117) Muhammad, M.; Buswell, S. C.; Dew, S. K.; Stepanova, M. Nanopatterning of PMMA on Insulating Surfaces with Various Anticharging Schemes Using 30 KeV Electron Beam Lithography. *J. Vac. Sci. Technol. B Nanotechnol. Microelectron. Mater. Process. Meas. Phenom.* **2011**, *29* (6), 06F304.

(118) Bagheri, S.; Giessen, H.; Neubrech, F. Large-Area Antenna-Assisted SEIRA Substrates by Laser Interference Lithography. *Adv. Opt. Mater.* **2014**, *2* (11), 1050–1056.

(119) Zetie, K. P.; Adams, S. F.; Tocknell, R. M. How Does a Mach-Zehnder Interferometer Work? *Phys. Educ.* **2000**, *35* (1), 46.

(120) Mennucci, C.; Chowdhury, D.; Manzato, G.; Barelli, M.; Chittofrati, R.; Martella, C.; Buatier de Mongeot, F. Large-Area Flexible Nanostripe Electrodes Featuring Plasmon Hybridization Engineering. *Nano Res.* **2021**, *14* (3), 858–867.

(121) Darvishzadeh-Varcheie, M.; Thrift, W. J.; Kamandi, M.; Ragan, R.; Capolino, F. Two-Scale Structure for Giant Field Enhancement: Combination of Rayleigh Anomaly and Colloidal Plasmonic Resonance. *Phys. Rev. Appl.* **2019**, *11* (5), 054057.

(122) Valbusa, U.; Boragno, C.; De Mongeot, F. B. Nanostructuring Surfaces by Ion Sputtering. *J. Phys. Condens. Matter* **2002**, *14* (35), 8153.

(123) Toma, A.; Chiappe, D.; Massabo, D.; Boragno, C.; Buatier de Mongeot, F. Self-Organized Metal Nanowire Arrays with Tunable Optical Anisotropy. *Appl. Phys. Lett.* **2008**, *93* (16), 163104.

(124) van Popta, A. C.; Sit, J. C.; Brett, M. J. Optical Properties of Porous Helical Thin Films and the Effects of Post-Deposition Annealing; Heremans, P. L., Muccini, M., Hofstraat, H., Eds.; Strasbourg, France, 2004; p 198. https://doi.org/10.1117/12.545923.

(125) Vick, D.; Friedrich, L. J.; Dew, S. K.; Brett, M. J.; Robbie, K.; Seto, M.; Smy, T. Self-Shadowing and Surface Diffusion Effects in Obliquely Deposited Thin Films. *Thin Solid Films* **1999**, *339* (1–2), 88–94. https://doi.org/10.1016/S0040-6090(98)01154-7.

(126) Vick, D.; Smy, T.; Brett, M. J. Growth Behavior of Evaporated Porous Thin Films. *J. Mater. Res.* **2002**, *17* (11), 2904–2911.

(127) Jensen, M. O.; Brett, M. J. Periodically Structured Glancing Angle Deposition Thin Films. *IEEE Trans. Nanotechnol.* **2005**, *4* (2), 269–277.

(128) Demers, H.; Poirier-Demers, N.; Couture, A. R.; Joly, D.; Guilmain, M.; de Jonge, N.; Drouin, D. Three-Dimensional Electron Microscopy Simulation with the CASINO Monte Carlo Software. *Scanning* **2011**, *33* (3), 135–146. https://doi.org/10.1002/sca.20262.

(129) Romo-Kröger, C. M. A Qualitative Study of Atmospheric Aerosols and Particles Deposited on Flat Membrane Surfaces by Microscopy and Other Techniques. *Powder Technol.* **2006**, *161* (3), 235–241. https://doi.org/10.1016/j.powtec.2005.10.014.

(130) Cyrs, W. D.; Boysen, D. A.; Casuccio, G.; Lersch, T.; Peters, T. M. Nanoparticle Collection Efficiency of Capillary Pore Membrane Filters. *J. Aerosol Sci.* **2010**, *41* (7), 655–664.

(131) Chen, S.-C.; Wang, J.; Fissan, H.; Pui, D. Y. H. Use of Nuclepore Filters for Ambient and Workplace Nanoparticle Exposure Assessment—Spherical Particles. *Atmos. Environ.* **2013**, *77*, 385–393. https://doi.org/10.1016/j.atmosenv.2013.05.007.

(132) Müller, T.; Gerardino, A.; Schnelle, T.; Shirley, S. G.; Bordoni, F.; De Gasperis, G.; Leoni, R.; Fuhr, G. Trapping of Micrometre and Sub-Micrometre Particles by High-Frequency Electric Fields and Hydrodynamic Forces. *J. Phys. Appl. Phys.* **1996**, *29* (2), 340.

(133) Yamada, M.; Seki, M. Hydrodynamic Filtration for On-Chip Particle Concentration and Classification Utilizing Microfluidics. *Lab. Chip* **2005**, *5* (11), 1233–1239.

(134) Massabò, D.; Danelli, S. G.; Brotto, P.; Comite, A.; Costa, C.; Di Cesare, A.; Doussin, J. F.; Ferraro, F.; Formenti, P.; Gatta, E.; Negretti, L.; Oliva, M.; Parodi, F.; Vezzulli, L.; Prati, P. ChAMBRe: A New Atmospheric Simulation Chamber for Aerosol Modelling and Bio-Aerosol Research. *Atmospheric Meas. Tech.* **2018**, *11* (10), 5885–5900. https://doi.org/10.5194/amt-11-5885-2018.

(135) Danelli, S. G.; Brunoldi, M.; Massabò, D.; Parodi, F.; Vernocchi, V.; Prati, P. Comparative Characterization of the Performance of Bio-Aerosol Nebulizers in Connection with Atmospheric Simulation Chambers. *Atmospheric Meas. Tech.* **2021**, *14* (6), 4461–4470. https://doi.org/10.5194/amt-14-4461-2021.

(136) Willeke, K.; Whitby, K. T. Atmospheric Aerosols: Size Distribution Interpretation. *J. Air Pollut. Control Assoc.* **1975**, *25* (5), 529–534. https://doi.org/10.1080/00022470.1975.10470110.

(137) Testa-Anta, M.; Ramos-Docampo, M. A.; Comesaña-Hermo, M.; Rivas-Murias, B.; Salgueiriño, V. Raman Spectroscopy to Unravel the Magnetic Properties of Iron

Oxide Nanocrystals for Bio-Related Applications. *Nanoscale Adv.* **2019**, *1* (6), 2086–2103. https://doi.org/10.1039/C9NA00064J.

(138) Zhang, J.; Con, C.; Cui, B. Electron Beam Lithography on Irregular Surfaces Using an Evaporated Resist. *ACS Nano* **2014**, *8* (4), 3483–3489.

(139) Kim, J.-H.; Zhou, Q.; Chang, J. A Facile Dry-PMMA Transfer Process for Electron-Beam Lithography on Non-Flat Substrates. In *2017 IEEE 30th International Conference on Micro Electro Mechanical Systems (MEMS)*; IEEE, 2017; pp 274–277.

(140) Dey, R. K.; Aydinoglu, F.; Cui, B. Electron Beam Lithography on Irregular Surface Using Grafted PMMA Monolayer as Resist. *Adv. Mater. Interfaces* **2017**, *4* (3), 1600780.

(141) Caldwell, J. D.; Glembocki, O. J.; Bezares, F. J.; Kariniemi, M. I.; Niinistö, J. T.; Hatanpää, T. T.; Rendell, R. W.; Ukaegbu, M.; Ritala, M. K.; Prokes, S. M.; Hosten, C. M.; Leskelä, M. A.; Kasica, R. Large-Area Plasmonic Hot-Spot Arrays: Sub-2 Nm Interparticle Separations with Plasma-Enhanced Atomic Layer Deposition of Ag on Periodic Arrays of Si Nanopillars. *Opt. Express* **2011**, *19* (27), 26056. https://doi.org/10.1364/OE.19.026056.

(142) Oh, Y.-J.; Kang, M.; Park, M.; Jeong, K.-H. Engineering Hot Spots on Plasmonic Nanopillar Arrays for SERS: A Review. *BioChip J.* **2016**, *10* (4), 297–309. https://doi.org/10.1007/s13206-016-0406-2.

(143) Andreani, L. C.; Agio, M. Photonic Bands and Gap Maps in a Photonic Crystal Slab. *IEEE J. Quantum Electron.* **2002**, *38* (7), 891–898. https://doi.org/10.1109/JQE.2002.1017603.

(144) Fazio, B.; D'Andrea, C.; Bonaccorso, F.; Irrera, A.; Calogero, G.; Vasi, C.; Gucciardi, P. G.; Allegrini, M.; Toma, A.; Chiappe, D.; Martella, C.; Buatier de Mongeot, F. Re-Radiation Enhancement in Polarized Surface-Enhanced Resonant Raman Scattering of Randomly Oriented Molecules on Self-Organized Gold Nanowires. *ACS Nano* **2011**, *5* (7), 5945–5956. https://doi.org/10.1021/nn201730k.

(145) Laurent, G.; Félidj, N.; Aubard, J.; Lévi, G.; Krenn, J. R.; Hohenau, A.; Schider, G.; Leitner, A.; Aussenegg, F. R. Evidence of Multipolar Excitations in Surface Enhanced Raman Scattering. *Phys. Rev. B* **2005**, *71* (4), 045430. https://doi.org/10.1103/PhysRevB.71.045430.

(146) Repetto, D.; Giordano, M. C.; Foti, A.; Gucciardi, P. G.; Mennucci, C.; Buatier de Mongeot, F. SERS Amplification by Ultra-Dense Plasmonic Arrays on Self-Organized PDMS Templates. *Appl. Surf. Sci.* **2018**, *446*, 83–91. https://doi.org/10.1016/j.apsusc.2018.02.163.

(147) D'Andrea, C.; Irrera, A.; Fazio, B.; Foti, A.; Messina, E.; Maragò, O. M.; Kessentini, S.; Artoni, P.; David, C.; Gucciardi, P. G. Red Shifted Spectral Dependence of the SERS Enhancement in a Random Array of Gold Nanoparticles Covered with a Silica Shell: Extinction versus Scattering. *J. Opt.* **2015**, *17* (11), 114016. https://doi.org/10.1088/2040-8978/17/11/114016.

(148) D'Andrea, C.; Bochterle, J.; Toma, A.; Huck, C.; Neubrech, F.; Messina, E.; Fazio, B.; Maragò, O. M.; Di Fabrizio, E.; Lamy de La Chapelle, M.; Gucciardi, P. G.; Pucci, A. Optical Nanoantennas for Multiband Surface-Enhanced Infrared and Raman Spectroscopy. *ACS Nano* **2013**, *7* (4), 3522–3531. https://doi.org/10.1021/nn4004764.

(149) Siegfried, T.; Ekinci, Y.; Martin, O. J. F.; Sigg, H. Gap Plasmons and Near-Field Enhancement in Closely Packed Sub-10 Nm Gap Resonators. *Nano Lett.* **2013**, *13* (11), 5449–5453. https://doi.org/10.1021/nl403030g.

(150) Aćimović, S. S.; Kreuzer, M. P.; González, M. U.; Quidant, R. Plasmon Near-Field Coupling in Metal Dimers as a Step toward Single-Molecule Sensing. *ACS Nano* **2009**, *3* (5), 1231–1237. https://doi.org/10.1021/nn900102j.

(151) König, M.; Rahmani, M.; Zhang, L.; Lei, D. Y.; Roschuk, T. R.; Giannini, V.; Qiu, C.-W.; Hong, M.; Schlücker, S.; Maier, S. A. Unveiling the Correlation between Nanometer-Thick Molecular Monolayer Sensitivity and Near-Field Enhancement and Localization in Coupled Plasmonic Oligomers. *ACS Nano* **2014**, *8* (9), 9188–9198. https://doi.org/10.1021/nn5028714.

(152) Jonsson, M. P.; Dahlin, A. B.; Feuz, L.; Petronis, S.; Höök, F. Locally Functionalized Short-Range Ordered Nanoplasmonic Pores for Bioanalytical Sensing. *Anal. Chem.* **2010**, *82* (5), 2087–2094. https://doi.org/10.1021/ac902925e.

(153) Novara, C.; Lamberti, A.; Chiadò, A.; Virga, A.; Rivolo, P.; Geobaldo, F.; Giorgis, F. Surface-Enhanced Raman Spectroscopy on Porous Silicon Membranes Decorated with Ag Nanoparticles Integrated in Elastomeric Microfluidic Chips. *RSC Adv.* **2016**, *6* (26), 21865–21870. https://doi.org/10.1039/C5RA26746C.

(154) Prikhozhdenko, E. S.; Bratashov, D. N.; Gorin, D. A.; Yashchenok, A. M. Flexible Surface-Enhanced Raman Scattering-Active Substrates Based on Nanofibrous Membranes. *Nano Res.* **2018**, *11* (9), 4468–4488. https://doi.org/10.1007/s12274-018-2064-2.

(155) Rossi, S.; Gazzola, E.; Capaldo, P.; Borile, G.; Romanato, F. Grating-Coupled Surface Plasmon Resonance (GC-SPR) Optimization for Phase-Interrogation Biosensing in a Microfluidic Chamber. *Sensors* **2018**, *18* (5), 1621. https://doi.org/10.3390/s18051621.

(156) Barelli, M.; Giordano, M. C.; Gucciardi, P. G.; Buatier de Mongeot, F. Self-Organized Nanogratings for Large-Area Surface Plasmon Polariton Excitation and Surface-Enhanced Raman Spectroscopy Sensing. *ACS Appl. Nano Mater.* **2020**, *3* (9), 8784–8793. https://doi.org/10.1021/acsanm.0c01569.

(157) Sarcina, L.; Macchia, E.; Loconsole, G.; D'Attoma, G.; Saldarelli, P.; Elicio, V.; Palazzo, G.; Torsi, L. Surface Plasmon Resonance Assay for Label-Free and Selective Detection of *Xylella Fastidiosa*. *Adv. NanoBiomed Res.* **2021**, *1* (10), 2100043. https://doi.org/10.1002/anbr.202100043.

(158) Nugroho, F. A. A.; Albinsson, D.; Antosiewicz, T. J.; Langhammer, C. Plasmonic Metasurface for Spatially Resolved Optical Sensing in Three Dimensions. *ACS Nano* **2020**, *14* (2), 2345–2353. https://doi.org/10.1021/acsnano.9b09508.

(159) Wang, Y.; Zhao, C.; Wang, J.; Luo, X.; Xie, L.; Zhan, S.; Kim, J.; Wang, X.; Liu, X.; Ying, Y. Wearable Plasmonic-Metasurface Sensor for Noninvasive and Universal Molecular Fingerprint Detection on Biointerfaces. *Sci. Adv.* **2021**, *7* (4), eabe4553. https://doi.org/10.1126/sciadv.abe4553.

(160) Alipour, A.; Farmani, A.; Mir, A. High Sensitivity and Tunable Nanoscale Sensor Based on Plasmon-Induced Transparency in Plasmonic Metasurface. *IEEE Sens. J.* **2018**, *18* (17), 7047–7054. https://doi.org/10.1109/JSEN.2018.2854882.

(161) Xiao-Ping Jin; Xu-Guang Huang; Jin Tao; Xian-Shi Lin; Qin Zhang. A Novel Nanometeric Plasmonic Refractive Index Sensor. *IEEE Trans. Nanotechnol.* **2010**, *9* (2), 134–137. https://doi.org/10.1109/TNANO.2009.2038909.

(162) Fano, U. Effects of Configuration Interaction on Intensities and Phase Shifts. *Phys. Rev.* **1961**, *124* (6), 1866–1878. https://doi.org/10.1103/PhysRev.124.1866.

(163) Francescato, Y.; Giannini, V.; Maier, S. A. Plasmonic Systems Unveiled by Fano Resonances. *ACS Nano* **2012**, *6* (2), 1830–1838. https://doi.org/10.1021/nn2050533.

(164) Liu, J.; Liu, Z.; Hu, H. Tunable Multiple Fano Resonance Employing Polarization-Selective Excitation of Coupled Surface-Mode and Nanoslit Antenna Resonance in Plasmonic Nanostructures. *Sci. Rep.* **2019**, *9* (1), 2414. https://doi.org/10.1038/s41598-019-38708-2.

(165) Wu, S.; Shen, Y.; Jin, C. Surface-Enhanced Raman Scattering Induced by the Coupling of the Guided Mode with Localized Surface Plasmon Resonances. *Nanoscale* **2019**, *11* (30), 14164–14173. https://doi.org/10.1039/C9NR02831E.

(166) Chowdhury, D.; Giordano, M. C.; Manzato, G.; Chittofrati, R.; Mennucci, C.; Buatier de Mongeot, F. Large-Area Microfluidic Sensors Based on Flat-Optics Au Nanostripe Metasurfaces. *J. Phys. Chem. C* **2020**, *124* (31), 17183–17190. https://doi.org/10.1021/acs.jpcc.0c03023.

(167) Zeng, B.; Gao, Y.; Bartoli, F. J. Rapid and Highly Sensitive Detection Using Fano Resonances in Ultrathin Plasmonic Nanogratings. *Appl. Phys. Lett.* **2014**, *105* (16), 161106. https://doi.org/10.1063/1.4899132.

(168) Noguez, C. Surface Plasmons on Metal Nanoparticles: The Influence of Shape and Physical Environment. *J. Phys. Chem. C* **2007**, *111* (10), 3806–3819. https://doi.org/10.1021/jp066539m.

(169) López-Muñoz, G. A.; Estevez, M.-C.; Peláez-Gutierrez, E. C.; Homs-Corbera, A.; García-Hernandez, M. C.; Imbaud, J. I.; Lechuga, L. M. A Label-Free Nanostructured Plasmonic Biosensor Based on Blu-Ray Discs with Integrated Microfluidics for Sensitive Biodetection. *Biosens. Bioelectron.* **2017**, *96*, 260–267. https://doi.org/10.1016/j.bios.2017.05.020.

(170) Shen, Y.; Zhou, J.; Liu, T.; Tao, Y.; Jiang, R.; Liu, M.; Xiao, G.; Zhu, J.; Zhou, Z.-K.; Wang, X.; Jin, C.; Wang, J. Plasmonic Gold Mushroom Arrays with Refractive Index Sensing Figures of Merit Approaching the Theoretical Limit. *Nat. Commun.* **2013**, *4* (1), 2381. https://doi.org/10.1038/ncomms3381.

(171) Kravets, V. G.; Kabashin, A. V.; Barnes, W. L.; Grigorenko, A. N. Plasmonic Surface Lattice Resonances: A Review of Properties and Applications. *Chem. Rev.* **2018**, *118* (12), 5912–5951. https://doi.org/10.1021/acs.chemrev.8b00243.

(172) Liu, F.; Zhang, X. Fano Coupling between Rayleigh Anomaly and Localized Surface Plasmon Resonance for Sensor Applications. *Biosens. Bioelectron.* **2015**, *68*, 719–725. https://doi.org/10.1016/j.bios.2015.01.071.

(173) Offermans, P.; Schaafsma, M. C.; Rodriguez, S. R. K.; Zhang, Y.; Crego-Calama, M.; Brongersma, S. H.; Gómez Rivas, J. Universal Scaling of the Figure of Merit of Plasmonic Sensors. *ACS Nano* **2011**, *5* (6), 5151–5157. https://doi.org/10.1021/nn201227b.

(174) Lee, K.-L.; Chen, P.-W.; Wu, S.-H.; Huang, J.-B.; Yang, S.-Y.; Wei, P.-K. Enhancing Surface Plasmon Detection Using Template-Stripped Gold Nanoslit Arrays on Plastic Films. *ACS Nano* **2012**, *6* (4), 2931–2939. https://doi.org/10.1021/nn3001142.

(175) Baquedano, E.; González, M. U.; Paniagua-Domínguez, R.; Sánchez-Gil, J. A.; Postigo, P. A. Low-Cost and Large-Size Nanoplasmonic Sensor Based on Fano Resonances with Fast Response and High Sensitivity. *Opt. Express* **2017**, *25* (14), 15967. https://doi.org/10.1364/OE.25.015967.

(176) Sosnova, M. V.; Dmitruk, N. L.; Korovin, A. V.; Mamykin, S. V.; Mynko, V. I.; Lytvyn, O. S. Local Plasmon Excitations in One-Dimensional Array of Metal Nanowires for Sensor Applications. *Appl. Phys. B* **2010**, *99* (3), 493–497. https://doi.org/10.1007/s00340-009-3799-y.

(177) Lee, S.; Mayer, K. M.; Hafner, J. H. Improved Localized Surface Plasmon Resonance Immunoassay with Gold Bipyramid Substrates. *Anal. Chem.* **2009**, *81* (11), 4450–4455. https://doi.org/10.1021/ac900276n.

(178) Lassiter, J. B.; McGuire, F.; Mock, J. J.; Ciracì, C.; Hill, R. T.; Wiley, B. J.; Chilkoti, A.; Smith, D. R. Plasmonic Waveguide Modes of Film-Coupled Metallic Nanocubes. *Nano Lett.* **2013**, *13* (12), 5866–5872. https://doi.org/10.1021/nl402660s.

(179) Khorasaninejad, M.; Capasso, F. Broadband Multifunctional Efficient Meta-Gratings Based on Dielectric Waveguide Phase Shifters. *Nano Lett.* **2015**, *15* (10), 6709–6715. https://doi.org/10.1021/acs.nanolett.5b02524.

(180) Quaranta, G.; Basset, G.; Martin, O. J. F.; Gallinet, B. Recent Advances in Resonant Waveguide Gratings. *Laser Photonics Rev.* **2018**, *12* (9), 1800017. https://doi.org/10.1002/lpor.201800017.

(181) Joseph, S.; Sarkar, S.; Joseph, J. Grating-Coupled Surface Plasmon-Polariton Sensing at a Flat Metal–Analyte Interface in a Hybrid-Configuration. *ACS Appl. Mater. Interfaces* **2020**, *12* (41), 46519–46529. https://doi.org/10.1021/acsami.0c12525.

(182) Butun, S.; Aydin, K. Asymmetric Light Absorption and Reflection in Freestanding Nanostructured Metallic Membranes. *ACS Photonics* **2015**, *2* (12), 1652–1657. https://doi.org/10.1021/acsphotonics.5b00377.

(183) Sakat, E.; Vincent, G.; Ghenuche, P.; Bardou, N.; Collin, S.; Pardo, F.; Pelouard, J.-L.; Haïdar, R. Guided Mode Resonance in Subwavelength Metallodielectric Free-Standing Grating for Bandpass Filtering. *Opt. Lett.* **2011**, *36* (16), 3054. https://doi.org/10.1364/OL.36.003054.

(184) Siria, A.; Bocquet, M.-L.; Bocquet, L. New Avenues for the Large-Scale Harvesting of Blue Energy. *Nat. Rev. Chem.* **2017**, *1* (11), 0091. https://doi.org/10.1038/s41570-017-0091.

(185) Mouterde, T.; Keerthi, A.; Poggioli, A. R.; Dar, S. A.; Siria, A.; Geim, A. K.; Bocquet, L.; Radha, B. Molecular Streaming and Its Voltage Control in Ångström-Scale Channels. *Nature* **2019**, *567* (7746), 87–90. https://doi.org/10.1038/s41586-019-0961-5.

(186) Yanik, A. A.; Huang, M.; Artar, A.; Chang, T.-Y.; Altug, H. Integrated Nanoplasmonic-Nanofluidic Biosensors with Targeted Delivery of Analytes. *Appl. Phys. Lett.* **2010**, *96* (2), 021101. https://doi.org/10.1063/1.3290633.

(187) Kumar, S.; Cherukulappurath, S.; Johnson, T. W.; Oh, S.-H. Millimeter-Sized Suspended Plasmonic Nanohole Arrays for Surface-Tension-Driven Flow-Through SERS. *Chem. Mater.* **2014**, *26* (22), 6523–6530. https://doi.org/10.1021/cm5031848.

(188) Tuccio, S.; Centini, M.; Benedetti, A.; Sibilia, C. Subwavelength Coherent Control and Coupling of Light in Plasmonic Nanoresonators on Dielectric Waveguides. *J. Opt. Soc. Am. B* **2013**, *30* (2), 450. https://doi.org/10.1364/JOSAB.30.000450.

(189) Tan, C.; Simonen, J.; Niemi, T. Hybrid Waveguide-Surface Plasmon Polariton Modes in a Guided-Mode Resonance Grating. *Opt. Commun.* **2012**, *285* (21–22), 4381–4386. https://doi.org/10.1016/j.optcom.2012.07.027.

(190) Zhang, J.; Cai, L.; Bai, W.; Song, G. Hybrid Waveguide-Plasmon Resonances in Gold Pillar Arrays on Top of a Dielectric Waveguide. *Opt. Lett.* **2010**, *35* (20), 3408. https://doi.org/10.1364/OL.35.003408.

(191) Zentgraf, T.; Zhang, S.; Oulton, R. F.; Zhang, X. Ultranarrow Coupling-Induced Transparency Bands in Hybrid Plasmonic Systems. *Phys. Rev. B* **2009**, *80* (19), 195415. https://doi.org/10.1103/PhysRevB.80.195415.

(192) Lu, X.; Zheng, G. G.; Zhou, P. High Performance Refractive Index Sensor with Stacked Two-Layer Resonant Waveguide Gratings. *Results Phys.* **2019**, *12*, 759–765. https://doi.org/10.1016/j.rinp.2018.12.048.

(193) Debasree Chowdhury et al., Broadband Photon Harvesting in Organic Photovoltaic Devices Induced by Large-Area Nanogrooved Templates, under Submission to Solar RRL.

(194) Forrest, S. R. The Path to Ubiquitous and Low-Cost Organic Electronic Appliances on Plastic. *Nature* **2004**, *428* (6986), 911–918. https://doi.org/10.1038/nature02498.

(195) de Oliveira Hansen, R. M.; Liu, Y.; Madsen, M.; Rubahn, H.-G. Flexible Organic Solar Cells Including Efficiency Enhancing Grating Structures. *Nanotechnology* **2013**, *24* (14), 145301. https://doi.org/10.1088/0957-4484/24/14/145301.

(196) Han, Y. W.; Jeon, S. J.; Lee, H. S.; Park, H.; Kim, K. S.; Lee, H.; Moon, D. K. Evaporation-Free Nonfullerene Flexible Organic Solar Cell Modules Manufactured by An All-Solution Process. *Adv. Energy Mater.* **2019**, *9* (42), 1902065. https://doi.org/10.1002/aenm.201902065.

(197) Guo, F.; Chen, S.; Chen, Z.; Luo, H.; Gao, Y.; Przybilla, T.; Spiecker, E.; Osvet, A.; Forberich, K.; Brabec, C. J. Printed Smart Photovoltaic Window Integrated with an Energy-Saving Thermochromic Layer. *Adv. Opt. Mater.* **2015**, *3* (11), 1524–1529. https://doi.org/10.1002/adom.201500314.

(198) Davy, N. C.; Sezen-Edmonds, M.; Gao, J.; Lin, X.; Liu, A.; Yao, N.; Kahn, A.; Loo, Y.-L. Pairing of Near-Ultraviolet Solar Cells with Electrochromic Windows for Smart Management of the Solar Spectrum. *Nat. Energy* **2017**, *2* (8), 17104. https://doi.org/10.1038/nenergy.2017.104.

(199) Xue, R.; Zhang, J.; Li, Y.; Li, Y. Organic Solar Cell Materials toward Commercialization. *Small* **2018**, *14* (41), 1801793. https://doi.org/10.1002/smll.201801793.

(200) Müller, J.; Rech, B.; Springer, J.; Vanecek, M. TCO and Light Trapping in Silicon Thin Film Solar Cells. *Sol. Energy* **2004**, *77* (6), 917–930. https://doi.org/10.1016/j.solener.2004.03.015.

(201) Sarkın, A. S.; Ekren, N.; Sağlam, Ş. A Review of Anti-Reflection and Self-Cleaning Coatings on Photovoltaic Panels. *Sol. Energy* **2020**, *199*, 63–73. https://doi.org/10.1016/j.solener.2020.01.084.

(202) Raut, H. K.; Ganesh, V. A.; Nair, A. S.; Ramakrishna, S. Anti-Reflective Coatings: A Critical, in-Depth Review. *Energy Environ. Sci.* **2011**, *4* (10), 3779. https://doi.org/10.1039/c1ee01297e.

(203) Atwater, H. A.; Polman, A. Plasmonics for Improved Photovoltaic Devices. In *Materials for Sustainable Energy*; Co-Published with Macmillan Publishers Ltd, UK, 2010; pp 1–11. https://doi.org/10.1142/9789814317665_0001.

(204) Mandal, P.; Sharma, S. Progress in Plasmonic Solar Cell Efficiency Improvement: A Status Review. *Renew. Sustain. Energy Rev.* **2016**, *65*, 537–552. https://doi.org/10.1016/j.rser.2016.07.031.

(205) Fadakar Masouleh, F.; Das, N.; Rozati, S. Nano-Structured Gratings for Improved Light Absorption Efficiency in Solar Cells. *Energies* **2016**, *9* (9), 756. https://doi.org/10.3390/en9090756.

(206) Lee, S.; In, S.; Mason, D. R.; Park, N. Incorporation of Nanovoids into Metallic Gratings for Broadband Plasmonic Organic Solar Cells. *Opt. Express* **2013**, *21* (4), 4055. https://doi.org/10.1364/OE.21.004055.

(207) Mennucci, C.; Muhammad, M. H.; Hameed, M. F. O.; Mohamed, S. A.; Abdelkhalik, M. S.; Obayya, S. S. A.; Buatier de Mongeot, F. Broadband Light Trapping in Nanotextured Thin Film Photovoltaic Devices. *Appl. Surf. Sci.* **2018**, *446*, 74–82. https://doi.org/10.1016/j.apsusc.2018.02.186.

(208) Mennucci, C.; Del Sorbo, S.; Pirotta, S.; Galli, M.; Andreani, L. C.; Martella, C.; Giordano, M. C.; Buatier de Mongeot, F. Light Scattering Properties of Self-Organized Nanostructured Substrates for Thin-Film Solar Cells. *Nanotechnology* **2018**, *29* (35), 355301. https://doi.org/10.1088/1361-6528/aac9ac.

(209) Martella, C.; Chiappe, D.; Delli Veneri, P.; Mercaldo, L. V.; Usatii, I.; Buatier de Mongeot, F. Self-Organized Broadband Light Trapping in Thin Film Amorphous Silicon Solar Cells. *Nanotechnology* **2013**, *24* (22), 225201. https://doi.org/10.1088/0957-4484/24/22/225201.

(210) Galeotti, F.; Trespidi, F.; Timò, G.; Pasini, M. Broadband and Crack-Free Antireflection Coatings by Self-Assembled Moth Eye Patterns. *ACS Appl. Mater. Interfaces* **2014**, *6* (8), 5827–5834. https://doi.org/10.1021/am500687f.

(211) Ghymn, Y. H.; Jung, K.; Shin, M.; Ko, H. A Luminescent Down-Shifting and Moth-Eyed Anti-Reflective Film for Highly Efficient Photovoltaic Devices. *Nanoscale* **2015**, *7* (44), 18642–18650. https://doi.org/10.1039/C5NR04440E.